The Dissertation Committee for Chun-Yaung Lu
certifies that this is the approved version of the following dissertation:

Dynamical simulation of molecular scale systems: methods and applications

Committee:

Graeme Henkelman, Supervisor

Peter J. Rossky

Dmitrii E. Makarov

David A. Vanden Bout

Thomas M. Truskett

Dynamical simulation of molecular scale systems: methods and applications

by

Chun-Yaung Lu, B.S.

DISSERTATION

Presented to the Faculty of the Graduate School of
The University of Texas at Austin
in Partial Fulfillment
of the Requirements
for the Degree of

DOCTOR OF PHILOSOPHY

THE UNIVERSITY OF TEXAS AT AUSTIN
December 2010

Dedicated to my family.

Acknowledgments

Most of all, I want to thank Graeme Henkelman for all his time and his insightful guidance in research. Graeme has been an excellent advisor and good friend. Professor David Vanden Bout and Dmitrii Makarov have also been excellent people to work with. I am grateful to my parents and grandparents for their understanding and support to my pursuit of science. Special thank to Hsuan and Elise for their emotional support. Finally, I want to thank all the group members for their help and support during my Ph.D. study.

Dynamical simulation of molecular scale systems: methods and applications

Chun-Yaung Lu, Ph.D.
The University of Texas at Austin, 2010

Supervisor: Graeme Henkelman

Rare-event phenomena are ubiquitous in nature. We propose a new strategy, κ-dynamics, to model rare event dynamics. In this methodology we only assume that the important rare-event dynamics obey first-order kinetics. Exact rates are not required in the calculation and the reaction path is determined on the fly. κ-dynamics is highly parallelizable and can be implemented on computer clusters and distributed machines. Theoretical derivations and several examples of atomic scale dynamics are presented.

With single-molecule (SM) techniques, the individual molecular process can be resolved without being averaged over the ensemble. However, factors such as apparatus stability, background level, and data quality will limit the amount of information being collected. We found that the correlation function calculated from the finite-size SM rotational diffusion trajectory will deviate

from its true value. Therefore, care must be taken not to interpret the difference as the evidence of new dynamics occurred in the system. We also proposed an algorithm of single fluorophore orientation reconstruction which converts three measured intensities $\{I_0, I_{45}, I_{90}\}$ to the dipole orientation. Fluctuations in the detected signals caused by the shot noise result in a different prediction from the true orientation. This difference should not be interpreted as the evidence of the nonisotropic rotational motion.

Catalytic reactions are also governed by the rare-events. Studying the dynamics of catalytic processes is an important subject since the more we learn, the more we can improve current catalysts. Fuel cells have become a promising energy source in the past decade. The key to make a high performance cell while keeping the price low is the choice of a suitable catalyst at the electrodes. Density functional theory calculations are carried out to study the role of geometric relaxation in the oxygen-reduction reaction for nanoparticle of various transition metals. Our calculations of Pt nanoparticles show that the structural deformation induced by atomic oxygen binding can energetically stabilize the oxidized states and thus reduces the catalytic activity. The catalytic performance can be improved by making alloys with less deformable metals.

Table of Contents

List of Tables

List of Figures

Chapter 1

Introduction

This thesis contains the work I did with my adviser Graeme Henkelman, Professor David Vanden Bout and Professor Dmitrii Makarov during my Ph.D. study in the physical chemistry division at the University of Texas at Austin. The main theme of the thesis is about utilizing computer simulation techniques to solve interesting problems which were either encountered in experiments or recognized in other theoretical studies. The content includes three major topics: κ-dynamics, single molecule correlation analysis and the geometric deformation in metallic nanoparticles induced by oxygen binding. Each part of the work is considered as an independent and self-containd story. This introduction gives a brief review of some general concepts relate to the following chapters.

1.1 Reaction rate simulation and accelerated dynamics

Almost everything in the real world changes with time. The concepts of “fast” and “slow” were originated from our sense experience and the term “rate” can be intuitively defined as how fast or how slow an event takes place. For chemists, chemical reaction is microscopically defined as a continuous atom rearrangements from reactant to product state. The time scales for reactions in nature can differ by several orders of magnitude. Oxidation reaction for example, can be either fast as in combustion or slow like rusting. Nowadays, atomistic dynamical simulations become available on modern computers by utilizing techniques such as molecular dynamics (MD). In classical MD the appropriate time step for atomic systems is on the order of femtoseconds (10^{-15} s) which is the typical time scale of vibrational motions in solid-state systems. Based on the current computing power, the time scale accessed by classical MD is limited to an order of nano- (10^{-9} s) to microsecond (10^{-6} s) while many important phenomena can occur on the scale of millisecond and beyond. A millisecond scale reaction for example will vibrate on average 10^{12} times before making a successful transition. For systems with very slow dynamics, direct simulations become prohibitively expensive. Several accelerated-MD techniques have been developed to improve efficiency, and have shown great promise for achieving long-time simulations. In the following, we briefly review several accelerated-dynamics techniques and related theories.

1.1.1 Transition state theory (TST)

Rare-events are usually described by a system escaping from a basin in the potential energy surface (PES). If the barrier for a system to leave the basin is high when compared with the thermal energy (k_BT), the system will spend a long time in the bottom region of the basin before crossing over the barrier. Since reactions seldom occur, the computational efficiency is low. One way to improve the simulation efficiency is to treat the basin part of the system in a statistical manner. In transition state theory, reaction rate is determined by the equilibrium flux through a dividing surface (denoted as $S^{\ddagger}$) located in the bottle-neck region along the reaction coordinate. In order for a reaction to take place, the system must overcome an energy barrier and cross $S^{\ddagger}$ to reach the product state.

There are an infinite number of possible $S^{\ddagger}$ and the values of the corresponding TST rates ($\mathrm{k}^{\mathrm{TST}}$) depend on the definition of $S^{\ddagger}$. An ideal $S^{\ddagger}$ will give a $\mathrm{k}^{\mathrm{TST}}$ equal to the true rate. However, in reality, not all trajectories leaving $S^{\ddagger}$ arrive at product state. Some of the trajectories can recross $S^{\ddagger}$ and return to the initial state. This leads to a variational version of TST, which states that TST provides an upper-bound of the true rate

$$\mathrm{k}^{\mathrm{true}} \leq \mathrm{k}^{\mathrm{TST}}. \tag{1.1}$$

The ratio $\mathrm{k}^{\mathrm{true}}/\mathrm{k}^{\mathrm{TST}}$ is called the dynamical correction factor (denoted as κ, also known as the transmission coefficient) which is a measurement of the quality of TST approximation. When TST rate is exact, κ is unity. Obviously, the choice of $S^{\ddagger}$ will decide whether $\mathrm{k}^{\mathrm{TST}}$ provides a good approximation.

If the motions around minima and saddle points can be well described by harmonic oscillators, $\mathrm{k}^{\mathrm{TST}}$ can be further expressed in the harmonic TST form

$$\mathrm{k}^{\mathrm{hTST}} = \frac{\prod_{i=1}^{3N} \nu_i^{min}}{\prod_{i=1}^{3N-1} \nu_i^{saddle}} e^{-\Delta E_a/k_B T}, \tag{1.2}$$

where N is the number of atoms, ν_i^{min} and ν_i^{saddle} are the frequencies of $3N$ and $3N-1$ nonimaginary normal modes at the minimum and saddle point respectively, ΔE_a is the potential energy difference between the minimum and the saddle point. This expression is referred to as the Vineyard equation.[1] At high temperature, the value of $\mathrm{k}^{\mathrm{hTST}}$ will deviate further from the true rate due to the increase of anharmonicity in the PES around the minima and saddle point.

1.1.2 Kinetic Monte Carlo (KMC)

Kinetic Monte Carlo provides a numerical solution to the Master equation

$$\frac{dp_i}{dt} = \sum_j -\mathrm{k}_{i\to j}\, p_i + \mathrm{k}_{j\to i}\, p_j. \tag{1.3}$$

The basic idea of KMC is to produce a statistically correct sequence of events and the transition times, using the knowledge of all possible transitions and the corresponding rates available to the system. In other words, the first thing we need to do in KMC is to make a rate table for the current state including all possible reactions and their rates. Then select the next state according to the probability

$$p_{i\to j} = \frac{\mathrm{k}_{i\to j}}{\mathrm{k}_{i\to}}, \tag{1.4}$$

where $p_{i\to j}$ is the probability for transition $i \to j$ to take place, $\mathrm{k}_{i\to j}$ is the transition rate from state i to j and $\mathrm{k}_{i\to} = \sum_j \mathrm{k}_{i\to j}$. Using Eq. (1.4), detailed balance, as well as the dynamical hierarchy, are satisfied for the system at equilibrium.

If all the processes escaping state i satisfy first-order kinetics, the duration time t_d in state i is exponentially distributed with probability density function

$$P_{i\rightarrow}(t_d) = \mathrm{k}_{i\rightarrow} \exp(-\mathrm{k}_{i\rightarrow} t_d). \tag{1.5}$$

A t_d which satisfies the above distribution can be obtained from

$$t_d = \frac{\ln(1/\mu)}{\mathrm{k}_{i\rightarrow}}, \tag{1.6}$$

where μ is an uniform random number on $(0, 1]$. By iterating Eq. (1.4) and Eq. (1.6), a state-to-state trajectory can be calculated.

The most severe limitation of KMC is that all the reaction mechanisms and their rates need to be identified *a priori*. Calculating all the rates can be prohibitively expensive. It is also difficult to know whether all possible processes have been identified. Several strategies, such as adaptive [2] and database approaches, have been incorporated into the original KMC scheme to improve the efficiency.

1.1.3 Accelerated dynamics methods based on trajectories

In MD simulations, the dynamical trajectory actually know nothing about the possible final states and the rates. The final states and the time scale are automatically determined when transitions occur. In KMC, more than the necessary information is required for the simulation. Several accelerated-dynamics schemes have been proposed based on the idea of using trajectories to probe the reactions. Three methods which belong to this catagory, parallel replica dynamics (PRD), hyperdynamics, and temperature-accelerated dynamics (TAD), are described below.

1.1.3.1 Parallel replica dynamics (PRD)

Parallel replica method is the simplest and the most accurate way to do accelerated-MD simulation. [3, 4] The only assumption made in this method is that the reactions satisfy first-order kinetics [Eq. (1.5)]. To implement PRD, we first make N replicas of the system and then randomize the momentum in each replica until their motions become totally uncorrelated. The simulation clock starts after this dephasing stage and stops when the first transition is detected in any of the replica. Because those N trajectories are independent, they can explore the phase space N times faster than using a single trajectory. Once a transition has been found, the overall simulation clock is advanced by the sum of all the simulation times in replicas. PRD boosts the simulation linearly with the number of replicas and can be easily implement on clusters of computers of or distributed architectures.

1.1.3.2 Hyperdynamics

The basic idea of hyperdynamics is using a non-negative bias potential to destablize the potential energy wells. [5, 6, 3] Assuming that the thermal energy is much lower than the energy barrier required for escaping the basin, and the TST formalism is valid, the TST rate of leaving state i for given dividing surface $S^\ddagger$ is

$$\mathrm{k}_{i\to}^{\mathrm{TST}} = \frac{\int\int |\upsilon_i|\delta_i(\mathbf{x})\Theta_i(\mathbf{x})e^{-\beta[K(\mathbf{p})+V(\mathbf{x})]}d\mathbf{x}d\mathbf{p}}{\int\int e^{-\beta[K(\mathbf{p})+V(\mathbf{x})]}d\mathbf{x}d\mathbf{p}}. \tag{1.7}$$

In the above equation, state i is defined as the region enclosed by the boundary $S^\ddagger$, $\upsilon_i = -(\nabla S^\ddagger \cdot \dot{\mathbf{x}}/|\nabla S^\ddagger|)$ is the velocity normal to $S^\ddagger$, $\delta_i(\mathbf{x})$ is a delta-function which returns unity when $\mathbf{x} \in S^\ddagger$ and zero otherwise, $\Theta_i(\mathbf{x})$ is an indicator function which returns unity when $\mathbf{x} \in i$ and zero otherwise.

Eq. (1.7) is rewritten by inserting a bias potential V_b which satisfies $V_b(\mathbf{x}) = 0$ when $\mathbf{x} \in S^\ddagger$

$$\begin{aligned} \mathrm{k}_{i\to}^{\mathrm{TST}} &= \frac{\int\int |\upsilon_i|\delta_i(\mathbf{x})\Theta_i(\mathbf{x})e^{-\beta[K(\mathbf{p})+V(\mathbf{x})+V_b(\mathbf{x})]}e^{+\beta V_b(\mathbf{x})}d\mathbf{x}d\mathbf{p}}{\int\int e^{-\beta[K(\mathbf{p})+V(\mathbf{x})]}d\mathbf{x}d\mathbf{p}} \\ &= \frac{\langle|\upsilon_i|\delta_i(\mathbf{x})\rangle_{i_b}}{\langle e^{\beta V_b(\mathbf{x})}\rangle_{i_b}} \\ &= \frac{\mathrm{k}_{i\to}^{b}}{\langle e^{\beta V_b(\mathbf{x})}\rangle_{i_b}}, \end{aligned} \tag{1.8}$$

where $\langle\cdots\rangle_{i_b}$ is a short notation for the ensemble average taken on the biased potential surface $V + V_b$, and $\mathrm{k}_{i\to}^{b}$ is the corresponding TST escape rate estimated from the biased potential surface. When running MD simulation on the biased potential, the time advanced in MD (Δt_{MD}) and hyperdynamics (Δt_b) are related by

$$\Delta t_b = \Delta t_{MD} \exp[\beta V_b(\mathbf{x})]. \tag{1.9}$$

Since $\Delta V > 0$, Δt_b is always larger or equal to Δt_{MD}, so that the dynamics are always accelerated. The average boost factor is defined as

$$\mathit{boost} = \langle\exp[\beta V_b(\mathbf{x})]\rangle_{i_b}. \tag{1.10}$$

The key point in hyperdynamics is to find a bias potential which satisfies the requirement $V_b = 0$ at the dividing surface and also be able to achieve the maximal boost. However, finding a suitable bias potential is a nontrivial task which requires some knowledge about the system. Finding bias potentials for complex systems such as proteins or other macromolecules remains an open challenge. Several techniques used to build bias potentials have been discussed in the literatures. [3, 7, 8]

1.1.3.3 Temperature-accelerated dynamics (TAD)

At high temperature, reactions become faster and can explore a larger volume in phase space. Reactions can be probed more efficiently when simulated at a higher temperature. The basic idea of TAD is to extrapolate high temperature dynamics to predict the dynamics at low temperature. In order to do this, we need a method that can connect the dynamics between two different temperatures. The key point of TAD is to extrapolate the duration times at high temperature to their low temperature values by using the relation, $\mathrm{k}_i^{(\mathrm{low})} t_i^{(\mathrm{low})} = \mathrm{k}_i^{(\mathrm{high})} t_i^{(\mathrm{high})}$, and rewriting the harmonic TST equation [Eq. (1.2)]

$$t_{i,\mathrm{low}} = t_{i,\mathrm{high}} e^{\Delta E_{a,i}(\beta_{\mathrm{low}} - \beta_{\mathrm{high}})}, \tag{1.11}$$

where $t_{i,\mathrm{low}}$ and $t_{i,\mathrm{high}}$ are the duration times of event i at low and high temperature respectively, $\beta \equiv k_B T$ for high or low temperature as specified, and $\Delta E_{a,i}$ is the energy barrier of the process which can be obtained from the nudged elastic band (NEB) method. [9, 10]

In TAD, a basin-constrained MD simulation is carried out at a high temperature. When the trajectory attempts to leave the state, the duration time and the energy barrier for this process at the high temperature are calculated. Then use Eq. (1.11) to extrapolate $t_{i,\mathrm{low}}$. The MD simulation is terminated when enough $t_{i,\mathrm{low}}$ values are collected. Finally, the shortest $t_{i,\mathrm{low}}$ is accepted and the state is updated accordingly. TAD is more approximate than PRD and hyperdynamics since it assumes harmonic TST is valid. But unlike hyperdynamics, we do not require a bias potential in TAD.

We have developed a new methodology called "κ-dynamics" which shares the idea of drawing times from a distribution with the KMC method, but it does not need a rate table. In κ-dynamics, possible product states are probed using MD trajectories launched from a dividing surface. Therefore, many advantages of the trajectory methods can also be found in κ-dynamics. More details are discussed in chapter 2.

1.2 Data analysis in single molecule experiments

1.2.1 Problems in single molecule measurements

Unlike bulk measurements, single molecule (SM) experiments deal with the signal from a individual molecule source. [11, 12, 13] Since the concentration of probed molecules is quite low, the detection is operated close to the thermal background. In addition, without ensemble averaging, the measured quantities fluctuate due to environmental variations and the stochastic entity of the observed process. Thus, there are two major challenges in the single molecule experiment design.

First of all is the detection limit. Because the signal from single molecule is relative small compared with bulk measurement, in order to separate useful signal from the background, techniques with high sensitivity are required. Compared with traditional methods, (e.g. ensemble photometry, spectroscopy, electrochemical experiments, etc.) SM detection requires extra design to eliminate the background intensity, or in other words, to increase the signal-to-noise ratio (S/N). Many techniques developed to overcome this problem, such as NSOM [14], confocal [15], and TIR microscopy [16], are now widely used in experiments. Most of those techniques are commercially available, and some of them have even become routine procedures in characterizing samples.

The second issue which scientists confront is related to the SM data analysis. As we mentioned above, the SM signal exhibits fluctuations which might not necessarily converge to a specific value with a finite number of observations. Before discussing further, we need to clarify the concept of sampling. Suppose we want to characterize the system by measuring a quantity M. According to ergodic theorem, the spatial average in a bulk measurement is assumed to be the same as the time average. However, in a SM experiment, if we track only a few molecular trajectories in a finite period of time, they might not be able to represent the entire sampling space. Unless we can prove that the data belong to a specific distribution, they can only be considered as single events. Experiments based on single-event observations usually can only provide some phenomenological information.

1.2.2 Measuring schemes of single molecule experiments

Obviously, an experimental design which can provide good statistics will always be a better choice. Based on the law of large numbers, better statistics can be obtained by repeating the measurements. But practically, it requires that the experiment itself can be easily implemented, and the system is stable enough during the measurements. Sometimes, a molecule itself is vulnerable under the probing field. Photobleaching, for example, is commonly observed during laser excitation. Once the molecule has been destroyed, a new molecule is used to continue the measurement. But different molecules might have different environments. Care must be taken when dealing with data including broken trajectories.

This kind of problem can be circumvented by designing an experiment in which the fluorophore acts only as a reporter. Data are analyzed by counting events rather than directly characterizing the trajectory. One of the examples is the SM study of enzyme kinetics. In the past decade, much works has been done in this area. [17, 18, 19, 20] The primary goal for these studies is to elucidate the mechanism of bio-systems on SM-level resolution.

Following the above scheme, in principle, one can collect data as much as possible until satisfactory statistics are achieved. Once the distributions of interest have been obtained, simple statistical tools, such as deconvolution, least square fit, or moment analysis can be used to characterize the distribution.

A different scheme which requires analyzing the whole trajectory is limited by the size of sample [21]. For example, to obtain a translational diffusion constant in a nano-scale environment, one can measure the displacements of probed molecule and calculate the diffusion coefficient from the distribution of displacements. However, due to photobleaching, trajectories terminate at some point. If we choose a new molecule, it may not be in the same environment. The two distributions will be different, and we cannot simply combine the two data sets together. For this reason, one needs to know how to extract information from data of finite size. This so-called "finite-sample problem" can be found in various fields.

1.2.3 Single molecule rotational diffusion

In SM rotation experiments, we measure the fluorescence signal from a single molecular probe embedded in the matrix. The signal carries information about the local environment as a function of time. Suppose the environment is isotropic and time invariant, the properties characterized from the observed trajectory will approach the ensemble value if the observation is long enough. However, in an anisotropic system, the probe might not be able to sample enough configurations. And things become even more complicated if the properties of the system are non-stationary due to time-dependent environment changes. Each trajectory should be considered independent.

Commonly, an auto-correlation function is used to characterize the rotational motions [21]. Since correlation functions are an average of the joint probability of two points on the trajectory separated by time lag k, the total number of pairs will affect the average value. It can be shown that for a stationary process, the variance of correlation function is inversely proportional to the trajectory length. Thus, even if the system is stationary, the correlation function calculated from a trajectory of finite length exhibits fluctuations. As a consequence, if one characterizes the sample correlation function by fitting it to a parameterized function, stretched exponential $Ae^{(-t/\tau)^\beta}$ for example, the variance in the correlation function will propagate to the fitting parameters. For a traditional dichroism measurement using high numerical aperture (N.A.) objective, the correlation function calculated from the dichroism trajectory mainly corresponds to its second rank spherical component. However, for the purpose of model identification, higher order terms provide more detail comparisons. If one can measure the real orientation of the probe molecule by using 3D imaging techniques, trajectories of higher order spherical harmonic components can be readily obtained. The finite-length sampling issue in single molecule correlation analysis are discussed in chapter 3. More details about the correlation analysis of 3D imaging data are presented in chapter 4.

1.3 Oxygen reduction reaction and metallic catalysts

The fuel cell has become a popular energy source which is, potentially a low-cost, low-carbon emission but high-efficiency electrochemical device. Although promising, there are still several issues limiting the performance of fuel cells under standard operating conditions. Among them is the sluggish kinetics of the oxygen reduction reaction (ORR) at the cathode

$$\frac{1}{2}O_2 + 2H^+ + 2e^- \to H_2O, \tag{1.12}$$

which is much slower than the oxidation reaction of hydrogen at the anode

$$H_2 \to 2H^+ + 2e^-. \tag{1.13}$$

The oxygen reduction reaction has been studied over the years because of its fundamental and technological importances. To date, the most widely used ORR catalyst is Pt supported on carbon. However, platinum is an extremely rare metal. The concentration of Pt in the Earth's crest is only 0.005 ppm. [22] The applications of Pt based catalysts are hindered by the high price and the unstable supply of the metal.

There is also a considerable overpotential associated with ORR on Pt, which diminishes the efficiency of the fuel cell performance. A more active material is needed to reduce the overpotential. Several efforts have been made to improve the performance of ORR catalysts. It is well-known that nanoparticles can have very different properties from the bulk materials. [23, 24] By reducing the size of the catalysts, one can expect some changes in the reactivity. Another way to tune the activity is by changing the composition of catalysts, such as making alloys, layer or core-shell structures. [25] Interactions between different types of metals can sometimes produce new properties. Strain [26], ligands [27] and geometric effects, as well as charge transfer [25], for example, have been observed in various multi-metallic systems.

According to the Brønsted-Evans-Polanyi (BEP) relation [28, 29], there exists a linear relation between the activation energy (barrier) and the reaction energy (binding of products) of an elementary reaction. By using this property, Bligaard *et al.* shown that the overall rate of a surface-catalyzed chemical process is determined by the dissociative chemisorption energy of the key reactant. [30] In the case of the ORR, the key parameter which determines the catalytic activity is the atomic oxygen binding energy. When the rates plot as a function of dissociative chemisorption energy, a peak will appear in the curve. The shape of the curve is similar to the famous "volcano plot" [31, 32] which is commonly seen when activity of catalyst is plotted as a function of catalyst surface parameter. In ORR, the volcano-like trend indicates that the ideal catalyst will have an intermediate oxygen binding energy. This result is not difficult to rationalize. Too-weak binding makes it hard for oxygen molecule to dissociate, while too-strong binding prevents the product desorbed from the surface. In both situations, the ORR activity are reduced. Nørskov *et al.* [33] have shown that the optimal atomic oxygen binding energy is slightly weaker than the binding on Pt(111). This prediction provides a guideline for designing a better ORR catalyst. By utilizing the above theories, in chapter 5, we use the atomic oxygen binding energy obtained from DFT calculation as an measurement to relate the geometric deformation with the ORR activity in metallic random alloy nanoparticles.

Chapter 2

κ-dynamics: An exact method for accelerating rare event classical molecular dynamics

2.1 Abstract

We propose a new strategy (κ-dynamics) to model rare event dynamics. It is well-understood that the exact rate can be obtained by applying the dynamical correction factor κ to the transition state theory rate $\mathrm{k}^{\mathrm{TST}}$. However, the computational cost of calculating the κ for many complex systems is so high that makes the dynamical simulation impractical. In κ-dynamics we launch trajectories (forward and backward) from the forward-flux ensemble of a dividing surface encloses the initial state until the first reactive trajectory is found. We prove that if first order kinetics is assumed, a duration time with the correct probability distribution can be generated using only the total number of trial shootings and $\mathrm{k}^{\mathrm{TST}}$ for the given dividing surface. Neither the exact rate nor the transmission coefficient is required in the calculation. Although mathematically similar to Kinetic Monte Carlo (KMC), κ-dynamics does not need the rate table. The reaction path is determined on the fly, and no information about the final states is needed *a priori*. κ-dynamics is highly parallelizable due to the thermodynamic nature of TST. This method is shown to be accurate in the study of surface diffusion on the Al (100) surface. Several

other examples of atomic scale dynamics are also presented in this work.

2.2 Introduction

One of the great challenges of modeling atomic motion is bridging the gap between atomic vibration on the femtosecond timescale and the interesting rare events, such as thermally activated bond breaking or bio-molecular dynamics, which can occur on the millisecond to second timescale. Several computational methods have been developed for accelerating molecular dynamics [34] using approaches such as increasing the temperature [35], applying a bias potential to destabilize minima [5], and integrating parallel replicas [4], to increase the rate of observing rare events. The primary assumption for these methods is that the interesting dynamics of the system can be described by rare events of short duration which take the system from one stable state to another. Then the fast dynamics within each stable state can be modeled statistically in an average or approximate way and the slow dynamics between states modeled correctly.

If an activated process satisfies first-order kinetics as expected for a rare-event system, the time interval between independent transitions are given by Poisson statistics and the duration times t_d are distributed exponentially:

$$P_{i\rightarrow}(t_d) = \mathrm{k}_{i\rightarrow} \exp(-\mathrm{k}_{i\rightarrow} t_d), \tag{2.1}$$

where $P_{i\rightarrow}(t_d)$ is the probability distribution of escaping state i in time t_d, and $\mathrm{k}_{i\rightarrow}$ is the rate of that escape. In the case of multiple product states j

the probability of being in state i is given by the master equation

$$\frac{dp_i}{dt} = \sum_j -\mathrm{k}_{i\to j}\, p_i + \mathrm{k}_{j\to i}\, p_j. \tag{2.2}$$

If all the rates $\mathrm{k}_{i\to j}$ are known, the dynamics of the system can be modeled exactly. However, for those complex systems, when solving the master equation becomes infeasible, an alternative method such as kinetic Monte Carlo (KMC) [36, 37] can be used to model the dynamics. In the KMC algorithm, a product state j is chosen stochastically with the probability

$$p_{i\to j} = \frac{\mathrm{k}_{i\to j}}{\mathrm{k}_{i\to}} \tag{2.3}$$

where $\mathrm{k}_{i\to} = \sum_j \mathrm{k}_{i\to j}$, and the time for the transition is drawn from $P_{i\to}(t_d)$ as

$$t_d = \frac{\ln(1/\mu)}{\mathrm{k}_{i\to}} \tag{2.4}$$

where μ is a uniform random number on $(0, 1]$.

There are two significant problems with using this expression in molecular dynamics simulations. First, from each state i, all product states j need to be found. In a high dimensional system with hundreds of atoms, there can be a very large number of such states and finding them all is not easy to do. Second, calculating the rates $\mathrm{k}_{i\to j}$ between these states is very expensive.

Transition state theory (TST) is a common approximation used to calculate reaction rates [38, 39]. The TST approach requires the identification of a transition state (TS), which is a dividing surface that separates reactants and products. If this TS surface contains the reaction bottleneck, the true rate can be approximated as the equilibrium flux through the surface in one direction. In most cases, however, it is difficult to identify a good TS *a priori*. Trajectories which cross the TS at short time can recross and reveal themselves as unreactive at longer times. Since TST is a variational theory that gives an upper bound on the true rate [40], the TS can be optimized to minimize the recrossings and the flux through the surface. The overestimation of the TST approximation can also be calculated from the recrossings of trajectories initiated at the TS [41, 42]. This so-called dynamical correction factor, or transmission coefficient, $\kappa \in [0, 1]$, is the ratio of the true rate to the TST rate,

$$\mathrm{k}_{i\to} = \kappa_{i\to}\mathrm{k}_{i\to}^{\mathrm{TST}}. \tag{2.5}$$

Voter and Doll [43] have shown how the transmission coefficient can be extended to multiple product states

$$\mathrm{k}_{i\to j} = \kappa_{i\to j}\mathrm{k}_{i\to}^{\mathrm{TST}}, \tag{2.6}$$

so that the true rate to each product state j can be calculated from short trajectories from the same TS surface. The branching ratio can also then be expressed in terms of the transmission factors

$$p_{i\to j} = \frac{\kappa_{i\to j}}{\kappa_{i\to}} \tag{2.7}$$

where $\kappa_{i\to} = \sum_j \kappa_{i\to j}$ and $\sum_j p_{i\to j} = 1$.

The importance of κ is strongly dependent upon the dynamics of the system and the ability to choose a good TS. In solid systems, the harmonic approximation to TST, in which the TS is taken to be a plane perpendicular to the negative mode at the saddle point for a reaction, can be very accurate [44]. Then, if the saddle points for all accessible reaction pathways can be found, the KMC algorithm can be used to model the long time dynamics of the system [45]. However, in the general case where $\kappa < 1$, either because a good TS can not be identified or dynamically correlated events are important, a better approach is needed to model the dynamics.

Also, if different reactions are uncorrelated, when a specific reaction occurs, the system actually need not to know anything about the other pathways. But in KMC a complete rate table which contains all possible reaction rates is required *a priori* for producing correct probabilities [Eq. (2.3) and (2.4)]. So an excessive amount of information is required by KMC and the accuracy of simulation depends greatly on the quality of rate table. Other methods such as hyperdynamics [5] and parallel replica dynamics [4] alternatively use a single trajectory to explore the phase space dynamically and the state evolution is determined by the progress of the trajectory as in a regular MD simulation. Since there is no need for the rate table, the performance of those methods relies on whether the trajectory can explore states efficiently. Clearly, both simulation schemes have their own advantages and disadvantages. In the present work, we proposed a new scheme for simulating rare-event dynamics which keeps the spirit of KMC drawing time from a probability distribution, without requiring a rate table. In the following we will first review the theoretical basis of κ-dynamics and then introduce the computational techniques utilized in our work. Some examples are shown in the last part of the chapter.

2.3 Theory

2.3.1 Reaction rate and the transition state approximation

Let $\mathbf{x} \in \mathbb{R}^n$ represents the set of 3N atomic Cartesian coordinates of a system in the canonical (constant-NVT) ensemble. The sets of conjugate velocities and momenta are denoted by $\mathbf{v}$ and $\mathbf{p}$ respectively ($\mathbf{v}, \mathbf{p} \in \mathbb{R}^n$). Assume the Born-Oppenheimer approximation is valid and the potential energy $V = V(\mathbf{x})$ is a function of nuclei positions only. The Hamiltonian of the system H is given by:

$$H = \frac{1}{2}\mathbf{p}^T\mathbf{M}^{-1}\mathbf{p} + V(\mathbf{x}), \tag{2.8}$$

where $\mathbf{M}$ is a diagonal mass matrix and $\mathbf{p}^T$ is the transpose matrix of $\mathbf{p}$. The probability density ρ in the phase space is governed by the Boltzmann distribution function:

$$\rho(\mathbf{x}, \mathbf{p}) = \mathcal{Z}^{-1} e^{-\beta H(\mathbf{x},\mathbf{p})}, \tag{2.9}$$

where $\beta \equiv (k_B\mathrm{T})^{-1}$ (k_B is the Boltzmann constant, T is the temperature) and $\mathcal{Z}$ represents the canonical partition function with $\mathcal{Q}$ and $\mathcal{K}$ the corresponding $\mathbf{x}$ and $\mathbf{p}$ integrals:

$$\mathcal{Z} \;=\; \int_{\mathbb{R}^n \times \mathbb{R}^n} e^{-\beta H(\mathbf{x},\mathbf{p})}\, d\mathbf{x}\, d\mathbf{p} = \mathcal{Q} \cdot \mathcal{K}. \tag{2.10}$$

The equilibrium population density of any set A in the configuration space is written as:

$$\phi_A = \mathcal{Q}^{-1} \int_A e^{-\beta V(\mathbf{x})} d\mathbf{x} \equiv \mathcal{Q}_A/\mathcal{Q} \tag{2.11}$$

where the subscript of $\mathcal{Q}$ specifies the integration range. Let $\mathbf{x}_i$ be one of the local minima of $V(\mathbf{x})$. State i (denoted as Ω_i) is defined as an open subset of the configuration space in which all the points can be related to the same local minimum $\mathbf{x}_i$ through a force-based energy minimization. Accordingly, the configuration space can be seen as a collection of states separated by a (3N − 1)-dimensional boundary S [i.e. $\bigcup_i \Omega_i \cup S = \mathbb{R}^n$, see Fig. 2.1(a)]. The boundary S is a natural choice for separating one state from the others. But practically finding S in a high dimensional system is difficult. An alternative surface of simpler form is usually chosen for convenience since the dynamics itself is independent of the type of the dividing surface. Here we only consider the system whose states are simple connected subsets, thus one connected surface is enough to isolate a state in the configuration space. Suppose in each state Ω there exists a subset ω ($\omega \subset \Omega$) which concentrates most of the probability in Ω, i.e. $\phi_\omega \approx \phi_\Omega$ and thus $\sum_i \phi_{\omega_i} \approx 1$. This assumption implies a dynamical trajectory will spend most of time in ωs rather than stay in the intermediate region which is usually referred to as the barrier region. In the following, a transition between two different ωs is defined as a reaction.

Given the initial state Ω_i, we now want to calculate the rate of escape. Assume the progress of the reactions occur in the system can be described by a particular reaction coordinate $s(\mathbf{x})$. The scalar-valued function $s(\mathbf{x})$ is

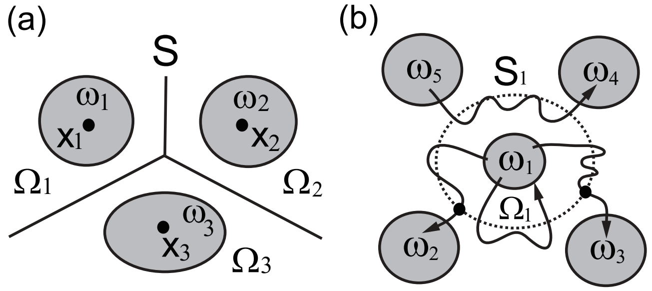

Figure 2.1: (a) The configuration space is partitioned into three states (Ω_i, $i =$ 1,2 and 3) by a (3N − 1)-dimensional hypersurface S. The corresponding local minimum is denoted by $\mathbf{x}_i$ and ω_i represents a subset in Ω_i which concentrates most of the population in Ω_i. (b) a dividing surface S_1 (dotted line) defines and separates state Ω_1 from the other states. The number of effective forward crossings (equals two in this case marked by solid circles) can be found by applying the counting rules $\Gamma_{\bar{i},S_i}(\mathbf{x},\mathbf{p})$ and $\Gamma_{i,\bar{i}}(\mathbf{x},-\mathbf{p})$ discussed in the text

continuous, differentiable and satisfies $s(\mathbf{x}) < s^{\ddagger}$ if $\mathbf{x} \in \Omega_i$. It is convenient to parameterize the boundary of Ω_i using $s(\mathbf{x})$:

$$S_i = \{\mathbf{x} \,|\, s(\mathbf{x}) = s^{\ddagger}\}, \tag{2.12}$$

where $s^{\ddagger} \in \mathbb{R}$ indicates the location of S_i. We define an indicator function $\theta_A(\mathbf{x})$ for any set A in the configuration space. $\theta_A(\mathbf{x}) = 1$ if $\mathbf{x} \in A$ and zero otherwise. The escape frequency ν is defined as the number of successful outward transitions (i.e. $\omega_i \rightarrow \omega_j$, $\omega_j \neq \omega_i$) per unit time. If the dynamics is ergodic, the counting can be done by tracking the state of a single trajectory. Let $\mathcal{X}(t)$ represents a dynamical trajectory which is generated from a constant-NVT MD simulation. The frequency of escape $\nu_{i\rightarrow}$ can be expressed in the effective forward-flux formalism:

$$\nu_{i\to} \;=\; \lim_{T\to\infty}\frac{1}{T}\int_0^T \theta_{\bar{i}}\{\mathcal{X}[t^+_{\bar{i}\,S_i}(t)]\}\theta_i\{\mathcal{X}[t^-_{i\,\bar{i}}(t)]\}\dot{\Theta}\{s[\mathcal{X}(t)]-s^\ddagger\}dt, \tag{2.13}$$

where $\bar{i}$ denotes any state other than ω_i, Θ is a Heaviside step-function, $\dot{\Theta} = d\Theta/dt$, the forward ($t^+$) and backward time ($t^-$) are defined as:

$$\begin{cases} t^+_{\bar{i}S_i}(t) & = \min\{\, t' \mid t' > t, \mathcal{X}(t') \in \omega_{\bar{i}} \cup S_i\} \\ t^-_{i\bar{i}}\;(t) & = \max\{\, t' \mid t' < t, \mathcal{X}(t') \in \omega_i \cup \omega_{\bar{i}}\}\ . \end{cases} \tag{2.14}$$

By ergodicity and using the definition of the escape rate coefficient $\mathrm{k}_{i\to} = \nu_{i\to}/\phi_i$, we rewrite Eq.(2.13) in the form of ensemble averaging:

$$\mathrm{k}_{i\to} \;=\; \phi_i^{-1}\langle[\mathbf{v}\cdot\nabla s(\mathbf{x})]_+\Gamma_{\bar{i},S_i}(\mathbf{x},\mathbf{p})\Gamma_{i,\bar{i}}(\mathbf{x},-\mathbf{p})\,]\rangle_{S_i} \tag{2.15}$$

where the equality $\dot{\Theta}[s(\mathbf{x})-s^\ddagger]=\delta[s(\mathbf{x})-s^\ddagger][\mathbf{v}\cdot\nabla s(\mathbf{x})]$ is used, $\delta[\cdots]$ denotes a δ-function, $[A]_+=\max(A,0)$, $\langle\cdots\rangle$ is a shorthand notation for a canonical ensemble averaging with the subscript S_i indicating the domain where the δ-function is active:

$$\begin{aligned}\langle A\rangle_{S_i} \;&=\; \langle A(\mathbf{x},\mathbf{p})\cdot\delta[s(\mathbf{x})-s^\ddagger]\,\rangle \\ &=\mathcal{Z}^{-1}\!\int_{\mathbb{R}^n\times\mathbb{R}^n} A(\mathbf{x},\mathbf{p})\delta[s(\mathbf{x})-s^\ddagger]\,e^{-\beta H(\mathbf{x},\mathbf{p})}d\mathbf{x}d\mathbf{p}.\end{aligned} \tag{2.16}$$

$\Gamma_{A,B}(\mathbf{x},\mathbf{p})$ is the indicator function which is 1 if the system reaches A before B given the starting point $(\mathbf{x},\mathbf{p})$ and 0 otherwise. Therefore if $\Gamma_{\bar{i},S_i}(\mathbf{x},\mathbf{p})\Gamma_{i,\bar{i}}(\mathbf{x},-\mathbf{p})$ is nonzero, it means the forward trajectory initiated from $(\mathbf{x},\mathbf{p})$ goes directly to the product state without recrossing the surface S_i, and the backward trajectory $(\mathbf{x},-\mathbf{p})$ originates in the initial state i. By applying both counting rules $\Gamma_{\bar{i},S_i}(\mathbf{x},\mathbf{p})$ and $\Gamma_{i,\bar{i}}(\mathbf{x},-\mathbf{p})$ one can unambiguously count the reactive trajectories as illustrated in Fig 1.1(b).

Taking the limit $\Gamma_{\bar{i},S_i}(\mathbf{x},\mathbf{p})\Gamma_{i,\bar{i}}(\mathbf{x},-\mathbf{p}) = 1$ in Eq.(2.15), we arrive at the TST approximation:

$$\mathrm{k}_{i\rightarrow}^{\mathrm{TST}} = \phi_i^{-1}\langle\, [\mathbf{v}\cdot\nabla q(\mathbf{x})]_+\,\rangle_{S_i}. \tag{2.17}$$

The above limit is equivalent to the assumption that all forward trajectories which cross the boundary S_i can be tracked back directly to ω_i and will end in ω_j ($\omega_j \neq \omega_i$) with no recrossing of S_i. Since Γ is either zero or one, the TST approximation [Eq.(2.17)] always overestimates the true escape rate. The transmission coefficient κ is defined as the ratio:

$$\begin{aligned}\kappa_{i\rightarrow} = \frac{\mathrm{k}_{i\rightarrow}}{\mathrm{k}_{i\rightarrow}^{\mathrm{TST}}} &= \frac{\langle[\mathbf{v}\cdot\nabla s(\mathbf{x})]_+\Gamma_{\bar{i},S_i}(\mathbf{x},\mathbf{p})\Gamma_{i,\bar{i}}(\mathbf{x},-\mathbf{p})\rangle_{S_i}}{\langle[\mathbf{v}\cdot\nabla s(\mathbf{x})]_+\rangle_{S_i}} && (2.18)\\ &= \langle\Gamma_{\bar{i},S_i}(\mathbf{x},\mathbf{p})\Gamma_{i,\bar{i}}(\mathbf{x},-\mathbf{p})\rangle_{FF} && (2.19)\end{aligned}$$

where in Eq.(2.19), $\langle A\rangle_{FF} = \langle A\cdot[\mathbf{v}\cdot\nabla s(\mathbf{x})]_+\rangle_{S_i}/\langle[\mathbf{v}\cdot\nabla s(\mathbf{x})]_+\rangle_{S_i}$ is a shorthand notation for the forward-flux-weighted ensemble averaging. If the final states in Eq.(2.15) are specified, $\kappa_{i\rightarrow}$ can be further decomposed by $\kappa_{i\rightarrow} = \sum_j \kappa_{i\rightarrow j}$. The branching ratio is defined as $p_{i\rightarrow j} = \kappa_{i\rightarrow j}/\kappa_{i\rightarrow}$ [Eq. (2.7)] with $\sum_j p_{i\rightarrow j} = 1$. The quantity $\kappa_{i\rightarrow}$ is not only a dynamical correction factor to the TST rate, but is also a measurement of the quality of the TST approximation. When $\kappa_{i\rightarrow} = 1$, the TST rate becomes exact. Since $k_{i\rightarrow}^{\mathrm{TST}}$ is intrinsic to the surface S_i, given the form of Eq.(2.12), $k_{i\rightarrow}^{\mathrm{TST}}$ can be optimized for this particular type of surface by adjusting $s^{\ddagger}$. A global optimization of TST rates, also known as the variational

TST scheme, is much more complicated since it also take the dividing surface functional into account during the optimization. For simplicity, we only focus on the specific type of surface which can be parameterized as Eq.(2.12).

The TST rate [Eq.(2.17)] can be written in the reversible work formalism by introducing an intermediate surface $S_o = \{\mathbf{x} \,|\, s(\mathbf{x}) - s^o = 0\}$ close to the minimum and utilizing the concept of free energy:

$$k_{i\rightarrow}^{\mathrm{TST}} \;=\; \sqrt{\frac{1}{2\pi\beta}} \cdot \xi^{\ddagger} \cdot \lambda_i^o \cdot e^{-\beta \Delta G_o^{\ddagger}}, \tag{2.20}$$

where symbols (i), (o) and $(\ddagger)$ represent Ω_i, S_o and S_i respectively, $\xi^{\ddagger}$ is the geometric factor associated with the term ∇s. It has a non-trivial contribution to the rate when dealing with particular types of curvilinear coordinates. The expression of $\xi^{\ddagger}$ for the dividing surface S_i is given by:

$$\xi^{\ddagger} \;=\; \mathcal{Q}_{S_i}^{-1} \int \sqrt{\mathbf{Z}_s} \cdot \delta[s(\mathbf{x}) - s^{\ddagger}]\, e^{-\beta V(\mathbf{x})} d\mathbf{x}, \tag{2.21}$$

where $\mathcal{Q}_{S_i}$ denotes:

$$\mathcal{Q}_{S_i} \;=\; \int_{\mathbb{R}^n} \delta[s(\mathbf{x}) - s^{\ddagger}]\, e^{-\beta V(\mathbf{x})} d\mathbf{x}, \tag{2.22}$$

$\mathbf{Z}_s$ is defined as:

$$\mathbf{Z}_s \;=\; \sum_{k}^{3N} \frac{1}{M_{kk}} \left(\frac{\partial s}{\partial \mathrm{x}_k} \right)^2 \tag{2.23}$$

with M_{kk} and x_k the matrix elements of $\mathbf{M}$ and $\mathbf{x}$ respectively. $\Delta G_o^{\ddagger}$ is the free energy difference between S_i and S_o:

$$\Delta G_o^{\ddagger} \;=\; -\beta^{-1} \ln \left(\frac{\mathcal{Q}_{S_i}}{\mathcal{Q}_{S_o}} \right), \tag{2.24}$$

and λ_i^o is defined as:

$$\lambda_i^o \;=\; \mathcal{Q}_{\Omega_i}^{-1}\int_{\mathbb{R}^n} \delta[s(\mathbf{x})- s^o]\, e^{-\beta V(\mathbf{x})} d\mathbf{x}. \tag{2.25}$$

The new formulation [Eq.(2.20)] turns the original flux averaging [Eq.(2.17)] into a combination of three different statistical samplings (i.e. $\xi^\ddagger$, $\Delta G_o^\ddagger$ and λ_i^o). The techniques used to estimate those terms are well-developed and can be found in various literatures.

2.3.2 κ-dynamics

In a regular kinetic Monte Carlo simulation the duration time and the final state are draw from the probability distributions Eq. (2.1) and (2.3) which contain the knowledge of all possible rates. Practically the calculation of the rates is difficult. In the previous section we showed that the true rate $\mathrm{k}_{i\to j}$ can be decomposed into two parts, $\mathrm{k}_{i\to}^{\mathrm{TST}}$ and $\kappa_{i\to j}$, where $\mathrm{k}_{i\to}^{\mathrm{TST}}$ is an equilibrium quantity and $\kappa_{i\to j}$ has the dynamical information. The transmission coefficient $\kappa_{i\to j}$ can be expressed using forward-flux-weighted averaging as shown previously in Eq. (2.19). Typically the averaging is done by shooting a large number of trajectories from the forward-flux ensemble of a given dividing surface and the estimation of κ is simply the portion of reactive trajectories. But it is not easy for a complex system especially when there are lots of possible final states or when κ is very small. In κ-dynamics, we show that the exact value of κ is not necessary when simulating dynamics. The theory is introduced below. Instead of counting the number of reactive trajectories, we switch to the scheme which counts the number of trial shootings until the first

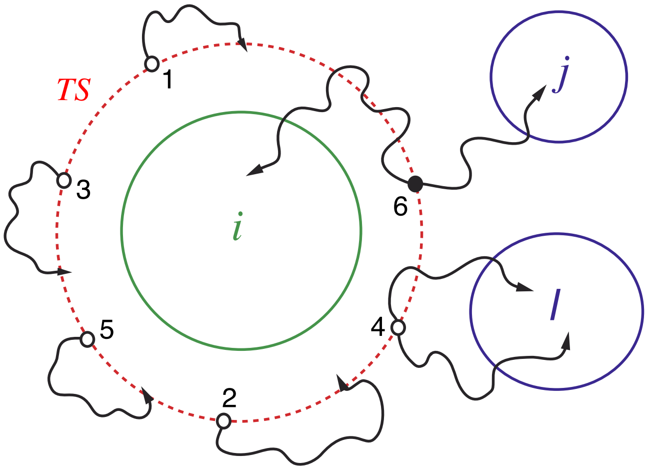

Figure 2.2: In the κ-dynamics method, trajectories are sampled from a TS surface that divides an initial state i from possible final state j and l. Trajectories are followed until one is found which starts in the initial state and goes directly to the product state without recrossing the TS. In this cartoon $N = 6$ trajectories were required to find the first reactive trajectory, giving an estimation of the transmission coefficient $\kappa_{i\rightarrow}$ of 1/6.

reactive one is found as illustrated in Fig. (2). If the initial point are randomly chosen from the forward-flux-weighed ensemble [Eq. (2.19)], the probability of having one successful trajectory is equal to $\kappa_{i\rightarrow}$. The probability of having the first reactive trajectory at the N_{th} trial shooting ($N > 0$) is described by the geometric distribution function:

$$P(N) = \kappa_{i\rightarrow}\left(1 - \kappa_{i\rightarrow}\right)^{N-1}. \tag{2.26}$$

which requires $N - 1$ unsuccessful trajectories before a successful one. The average of N is

$$\langle N \rangle = \sum_{N=1}^{\infty} N\, P(N) = \kappa_{i\rightarrow}^{-1}. \tag{2.27}$$

Therefore the inverse of $\langle N \rangle$ can be utilized as an estimator of $\kappa_{i\to}$. However, as mentioned above, in κ-dynamics we do not need to calculate $\langle N \rangle$ nor κ.

Given the TST Poisson distribution:

$$P_{i\to}^{\mathrm{TST}}(t_d) = \mathrm{k}_{i\to}^{\mathrm{TST}} \exp(-\mathrm{k}_{i\to}^{\mathrm{TST}} t_d), \tag{2.28}$$

the time assigned to the successful trajectory is actually the sum of N times drawn from the TST Poisson distribution [compare with Eq. (2.4)]

$$t_d = \sum_{n=1}^{N} \frac{\ln(1/\mu_n)}{\mathrm{k}_{i\to}^{\mathrm{TST}}}, \tag{2.29}$$

where μ_n are i.i.d. (independent and identically distributed) uniform random numbers on $(0, 1]$. The sum of N Poisson random numbers gives a distribution which was derived by the Danish engineer, A. K. Erlang, when studying the network traffic in a village telephone exchange [46]. For the TST Poisson times of Eq. (2.28), the Erlang distribution for N events is

$$\begin{aligned} P(t_d; N) &= \int_0^\infty \cdots \int_0^\infty \delta[t_d - \sum_{n=1}^{N} \tau_n] \prod_{n=1}^{N} P_{i\to}^{\mathrm{TST}}(\tau_n)\, d\tau_1 \cdots d\tau_N \\ &= \frac{(\mathrm{k}_{i\to}^{\mathrm{TST}})^N \cdot t_d^{N-1}}{(N-1)!} \exp(-\mathrm{k}_{i\to}^{\mathrm{TST}} t_d). \end{aligned} \tag{2.30}$$

These escape times are drawn from the geometric distribution

$$\begin{aligned}
P_{i\rightarrow}(t_d) &= \sum_{N=1}^{\infty} P(t_d;N)P(N) \\
&= \sum_{N=1}^{\infty} \frac{(\mathrm{k}_{i\rightarrow}^{\mathrm{TST}})^N t_d^{N-1} e^{-\mathrm{k}_{i\rightarrow}^{\mathrm{TST}} t_d}}{(N-1)!}(\kappa_{i\rightarrow})(1-\kappa_{i\rightarrow})^{N-1} \\
&= \kappa_{i\rightarrow}\mathrm{k}_{i\rightarrow}^{\mathrm{TST}} \exp(-\mathrm{k}_{i\rightarrow}^{\mathrm{TST}} t_d) \sum_{N=0}^{\infty} \frac{\left[\mathrm{k}_{i\rightarrow}^{\mathrm{TST}} t_d (1-\kappa_{i\rightarrow})\right]^N}{N!} \\
&= \kappa_{i\rightarrow}\mathrm{k}_{i\rightarrow}^{\mathrm{TST}} \exp(-\kappa_{i\rightarrow}\mathrm{k}_{i\rightarrow}^{\mathrm{TST}} t_d) \\
&= \mathrm{k}_{i\rightarrow} \exp(-\mathrm{k}_{i\rightarrow} t_d) \qquad (2.31)
\end{aligned}$$

using the definition of $\kappa_{i\rightarrow}$ from Eq. (2.18) and recognizing the sum as the expansion of an exponential function.

Since the distribution of successful κ-dynamics trajectories has the correct distribution of product states, from Eq. (2.7), and the transition time can be drawn from the correct Poisson distribution according to the true rate, from Eq. (2.31), we have shown that the method gives a correct state-to-state dynamical trajectory.

The algorithm of κ-dynamics is summarized in the following steps:

1. Sample a Boltzmann distribution in a TS defined by $s(\mathbf{x}) = s^{\ddagger}$ enclosing an initial state.
2. Select uncorrelated forward-flux weighted initial points on the TS.
3. Integrate N trajectories (forward and backward) until a successful one is found that goes directly to a product state without recrossing the TS and originates in the initial state.

4. If no such trajectory is found after $N_{\max}$ attempts, choose a new value of $s^{\ddagger}$ which increases the free energy of $s(\mathbf{x}) = s^{\ddagger}$ and return to step 1.

5. Increase the simulation time by an amount [Eq. (2.29)]

$$t_d = \sum_{n=1}^{N} \frac{\ln(1/\mu_n)}{\mathrm{k}_{i\to}^{\mathrm{TST}}}$$

   where the μ_n are uniform random numbers on $(0, 1]$.

6. Repeat from step 1 where the product state is the new initial state.

2.4 Methodology

In this section, we will briefly review the simulation tools needed for κ-dynamics which includes sampling a TS, shooting trajectories, and calculating the TST rate. Although there are various ways to estimate those quantities, the final result should not depend on any simulation scheme. The efficiency of a particular algorithm might differ from case to case and choosing an appropriate computational strategy is sometimes critical. The following methods were utilized in the examples illustrated in the later section.

2.4.1 Sampling issue

When a system has a rugged energy landscape, sampling becomes more challenging since the system is easily trapped in one of the local minimum. There are many well-developed methods which can be used to improve the sampling. In our work, sampling was done using replica exchange (also called parallel tempering) [47, 48, 49, 50] to overcome the multiple-minima problem by allowing replicas of the system run at different temperatures to exchange configurations. High temperature replicas are able to explore a larger volume of the phase space. A low temperature system can escape from the local minimum by exchanging the configuration with other high temperature replicas. The exchange is accepted or rejected according to a generalized Metropolis criterion [51]

$$P(\{\mathbf{x}_1, \mathbf{x}_2\} \to \{\mathbf{x}_2, \mathbf{x}_1\}) \;=\; \min[1, \exp(\Delta\beta\Delta E)], \tag{2.32}$$

where $\Delta\beta = \beta_2 - \beta_1$ and $\Delta E = E(\mathbf{x}_2) - E(\mathbf{x}_1)$. If replica exchange is implemented using MD (molecular dynamics) algorithm rather than MC (Monte Carlo), the momenta are also need to be rescaled using Eq. (2.33) in order to satisfy detailed balance [49, 50]

$$\{\mathbf{p}_1, \mathbf{p}_2\} \to \{\sqrt{T_1/T_2}\;\mathbf{p}_2, \sqrt{T_2/T_1}\;\mathbf{p}_1\} \tag{2.33}$$

In general, sampling becomes more efficient at the cost of extra computational expenses required for running replicas at multiple temperatures.

2.4.2 Calculations of $\xi^{\ddagger}$ and λ_i^o

For the sake of simplicity, in the following examples we only consider equal-mass distinguishable particles. Let m be the mass and $S(c) = \{\mathbf{x} \mid s(\mathbf{x}) - c\}$ denotes a hypersurface parameterized by c. We have $\sqrt{\mathbf{Z}_s} = m^{-1}|\nabla s|$ and the quantity

$$\psi_S \;=\; \mathcal{Q}^{-1}\int_{\mathbb{R}^n} \delta[s(\mathbf{x}) - c]\, e^{-\beta V(\mathbf{x})} d\mathbf{x} \tag{2.34}$$

represents the probability density of a thin slice with uniform thickness in the s-space around S. Suppose $S \subset A \subset \mathbb{R}^n$ where A is a subset in the configuration space, then the ratio ψ_S/ϕ_A can be obtained by taking the limit:

$$\frac{\psi_S}{\phi_A} = \lim_{\Delta s \to 0} \frac{1}{\Delta s} \frac{\phi_{S^*}}{\phi_A} . \tag{2.35}$$

where $S^* = \{\mathbf{x} | \, |s(\mathbf{x}) - c| \leq \Delta s/2\}$ is a slice of uniform thickness Δs in the s-space. The probability ratio ϕ_{S^*}/ϕ_A at equilibrium can be simply estimated through an NTV-constant MD simulation and the limit is done explicitly by making Δs small enough such that the value of ψ_S/ϕ_A becomes insensitive to Δs. By considering Eq.(2.25), we know λ_i^o already has the form of Eq.(2.34). Therefore the method can be applied directly to calculate λ_i^o.

As for $\xi^\ddagger$, we rewrite Eq.(2.21):

$$\xi^\ddagger = m^{-1} \frac{\int |\nabla s(\mathbf{x})| \delta[s(\mathbf{x}) - c^\ddagger] \, e^{-\beta V(\mathbf{x})} d\mathbf{x}}{\int \delta[s(\mathbf{x}) - c^\ddagger] \, e^{-\beta V(\mathbf{x})} d\mathbf{x}} . \tag{2.36}$$

The expression can be seen as performing ensemble averaging over $|\nabla s(\mathbf{x})|$ under the constraint $\delta[s(\mathbf{x}) - c^\ddagger]$. Following the strategy described above, the hypersurface is replaced by a slice of uniform thickness Δs ($\Delta s \to 0$) in the s-space, and the averaging is done through the MD simulation. However, since S_i is high above the minimum, sampling with regular MD will be inefficient. Therefore, a harmonic constraint $V_b(\mathbf{x}) \propto [s(\mathbf{x}) - c^\ddagger]^2$ centered at $c^\ddagger$ is added to the original potential $V(\mathbf{x})$ to concentrate the sampling. As long as $V_b \approx 0$ within the thin slice and the system is well thermalized, the estimation under the modified potential will still be accurate.

2.4.3 Calculation of $\Delta G_o^{\ddagger}$

The hypersurface $S(c)=\{\mathbf{x}\,|\,s(\mathbf{x})-c\}$ is parameterized by c. Umbrella sampling [52] and thermodynamic integration [53] are commonly used to calculate the free energy difference between two hypersurfaces (S_o and S_i for example) and the efficiency might vary from case to case. In the following examples we use umbrella sampling to estimate the free energy change along the reaction coordinate.

By definition, the free energy difference and the partition function ratio $\mathcal{Q}_{S_i}/\mathcal{Q}_{S_o}$ are related by Eq.(2.24). The value of $\mathcal{Q}_{S_i}/\mathcal{Q}_{S_o}$ can be estimated by either MD or MC. Direct sampling becomes inefficient when ΔG_o^i is big. Therefore multiple umbrella samplings are required to bridge the energy gap between two hypersurfaces. The basic idea of umbrella sampling is to reduce the influence of energy barrier by modifying the original potential V_0 with biasing potential V_b. The biasing potential is designed to confine sampling in a predetermined region in such a way that over all the simulations good coverage of the reaction coordinate is achieved. In this paper, harmonic type V_b is chosen for the sake of simplicity. Given the configuration $\mathbf{x}$ and the reference point c_s, the biasing potential and the corresponding force ($\mathbf{F}_b$) acting on atom k in the Cartesian direction $\hat{\zeta}$ ($\zeta = x, y, z$) are:

$$V_b(\mathbf{x}) = \frac{k_s}{2}\,[s(\mathbf{x}) - c_s]^2 \tag{2.37}$$

and

$$\mathbf{F}_b^{(k)}(\mathbf{x}) = -\sum_{\zeta} \frac{\partial V_b}{\partial s}\,\frac{\partial s}{\partial \zeta_k}\,\hat{\zeta}_k. \tag{2.38}$$

To carry out the overall free energy change, the weighted histogram analysis method (WHAM) [54] was used to analyze the data from umbrella sampling. The goal of WHAM is to combine data from multiple biased simulations and inverts thermodynamic properties, such as ΔG, back to their unbiased ensemble values.

2.4.4 Trial shooting and the calculation of $\kappa_{i\rightarrow}$

The first step in κ-dynamics is to sample the dividing surface to generate the foward-flux weighted initial points $(\mathbf{x}, \mathbf{p})$. The configurations $\mathbf{x}$ can be obtained by making MC walks confined to the dividing surface [43]. The initial velocity is decomposed into two parts. The velocity perpendicular to the dividing surface is chosen randomly from a Maxwellian-flux distribution $[P(v) \propto |v| \exp(-\beta m v^2/2)]$. The other components are drawn from a Boltzmann distribution $[P(v) \propto \exp(-\beta m v^2/2)]$. Another way to obtain the initial points is by adding a harmonic constraint V_b centered at the dividing surface to the original potential as described in the previous section. Then regular MD simulation is used to collect ($\mathbf{x}$,$\mathbf{p}$) of the crossing points under this combined field. If the thermostat functions well, both $\mathbf{x}$ and $\mathbf{p}$ will have the correct distribution. The advantage of the MD scheme is that the velocities are obtained simultaneously while the crossing points are found. Also, the same procedure is used in umbrella sampling, thus in practice two calculations can be done together.

A trial shooting is done by launching trajectories randomly from the forward-flux ensemble and applying the counting rules $\Gamma_{\bar{i},S_i}(\mathbf{x},\mathbf{p})$ and $\Gamma_{i,\bar{i}}(\mathbf{x},-\mathbf{p})$ to test whether those trajectories are reactive. The shooting scheme is asymmetric in that it counts only the last crossing of a reactive trajectory. The forward trajectory will terminate early if it recrosses the TS before thermalizing at the product state. When the dividing surface is below the free energy maximum in the reaction region, most of the forward trajectories will return to the minimum. Those trajectories will be assigned as unreactive after a few MD steps and thus reduce total number of force evaluations per trajectory. For the case that backward trajectories tend to recross than the forward trajectories, one can reverse the parity of the counting rules.

As shown previously, either Eq. (2.19) or (2.27) can be used to calculate $\kappa_{i\rightarrow}$. In the former case [Eq. (2.19)] a fixed number of trajectories are launched from the dividing surface and $\kappa_{i\rightarrow}$ is estimated as the portion of reactive trajectories. Eq. (2.27) is formulated based on the number of trial shootings N required until the first reactive one is found and $\kappa_{i\rightarrow}$ is estimated from the inverse of $\langle N\rangle$.

2.5 Examples

We have shown that κ-dynamics trajectories have the correct product state distribution [Eq. (2.7)] and transition times drawn from the correct exponential distribution according to the true rate [Eq. (2.31)], so the method gives a correct state-to-state dynamical trajectory. Several numerical examples are provided below to demonstrate the κ-dynamics method.

2.5.1 Dynamics of adatoms on Al(100) surface

The diffusion of adatoms on Al(100) surface was chosen as a model system to demonstrate how the escape processes of a given state [as shown in Fig. 2.1(b)] can be simulated and characterized by the methods described previously. This system has an interesting history in that the adatom was predicted to diffuse by exchange instead of by hoping. [55] An semiempirical potential based on the embedded atom method (EAM) was used to model the atomic interactions. The surfaces were approximated by a six layer slab (excluding the adatoms) with 50 atoms per layer. Periodic boundary condition was applied to this system with box size $20.1931 \times 20.1931 \times 110.0$ (Å^3). The two bottom layers were immobile and the top surface was left open to vacuum. Adatoms were deposited on the hollow sites of the top layer. Equation of motions were integrated using the velocity Verlet algorithm [56] with an Anderson thermostats [57] to generate a constant-TNV MD trajectory. Details of the techniques used in the examples are described in previously.

2.5.1.1 Adatom on frozen Al(100) surface

A simple three-dimensional system is used to illustrate how $\mathrm{k}_{i\rightarrow}^{\mathrm{TST}}$ varies as the shape of dividing surface and the true rate $\mathrm{k}_{i\rightarrow}$ is invariant upon the change. In Al(100) surface, if all the atoms except for the adatom are frozen, the total degrees of freedom will be six (x, y, z and the corresponding momenta). The only possible reaction occurred in this system is the adatom hopping [see Fig. 2.3(a)]. To calculate $\mathrm{k}_{i\rightarrow}^{\mathrm{TST}}$, we need to define a dividing

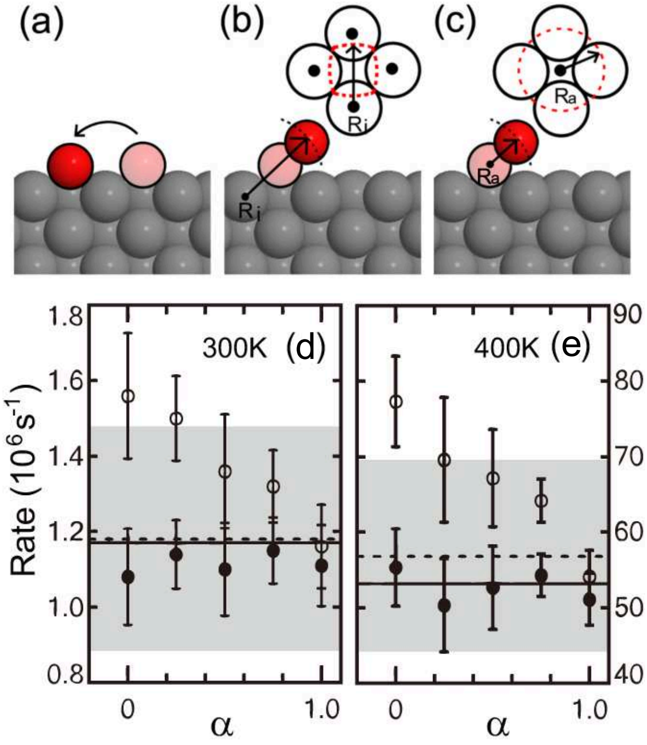

Figure 2.3: (a) Schematic illustration of an adatom hopping on the frozen Al(100) surface. The shape of the dividing surface when the reference points are assigned to (b) the four nearest atoms and (c) the center of the adatom in the minimum energy position (pink sphere). The adatom hopping rates calculated at 300K (d) and 400K (e) for various α (0, 0.25, 0.50, 0.75, and 1). The open and filled circles represent $\mathrm{k}_{i\rightarrow}^{\mathrm{TST}}$ and $\mathrm{k}_{i\rightarrow}$ respectively. The dashed lines are obtained from direct MD simulations with the shaded area the error range (one standard deviation). The harmonic TST rates (solid lines) are also compared in the figure.

surface. As shown in Fig. 2.3(b) and 2.3(c), the reference points are assigned to the center of the four nearest neighbors of the adatom [denoted as R_i ($i = 1, 2, 3, 4$)] and the center of adatom in the minimized structure (denoted as R_a). Let $\mathbf{r}$ represent the position of the adatom, $\mathbf{r}_{\mathrm{R}_i}$ and $\mathbf{r}_{\mathrm{R}_a}$ represent

Table 2.1: Transition state parameters for an Al adatom hopping on a frozen Al(100) surface.

$T = 300$K					$T = 400$K				
α	c^o	$c^\ddagger$	$\Delta G_o^\ddagger$	$\kappa_{i\to}$	α	c^o	$c^\ddagger$	$\Delta G_o^\ddagger$	$\kappa_{i\to}$
0.00	2.90	3.88	0.33	0.70	0.00	2.90	3.94	0.32	0.72
0.25	2.20	3.26	0.34	0.76	0.25	2.20	3.24	0.33	0.72
0.50	1.50	2.66	0.35	0.81	0.50	1.50	2.68	0.34	0.78
0.75	0.90	2.03	0.33	0.87	0.75	0.90	2.06	0.32	0.85
1.00	0.20	1.46	0.36	0.95	1.00	0.20	1.48	0.35	0.95

the position vector of the reference points, the dividing surface (S_i) is defined as:

$$S_i(c^\ddagger) = \{\mathbf{r} | \max(|\mathbf{r} - \mathbf{r}_{\mathrm{R}}|) = c^\ddagger\}, \tag{2.39}$$

where $\mathbf{r}_{\mathrm{R}}$ is the linear interpolating point of $\mathbf{r}_{\mathrm{R}_i}$ and $\mathbf{r}_{\mathrm{R}_a}$:

$$\mathbf{r}_{\mathrm{R}} = \mathbf{r}_{\mathrm{R}_i} + \alpha(\mathbf{r}_{\mathrm{R}_a} - \mathbf{r}_{\mathrm{R}_i}) \ \text{ with } \ \alpha \in [0, 1]. \tag{2.40}$$

By varying α from 0 to 1, the shape of the dividing surface will change from Fig. 2.3(b) to 2.3(c). $\mathrm{k}_{i\to}^{\mathrm{TST}}$ and $\mathrm{k}_{i\to}$ were calculated for dividing surfaces of various α and the corresponding $c^\ddagger$s are determined from the highest $\Delta G_o^\ddagger$. The calculated rates were summarized in Fig. 2.3(d) and 2.3(e). While $\mathrm{k}^{\mathrm{TST}}$ varies as the shape of S_i changes, the value of $\mathrm{k}_{i\to}$ is independent of the definition of S_i. In both cases, the harmonic TST rates show good agreement with the MD results. Some important factors in the calculation are summarized in Table 2.1.

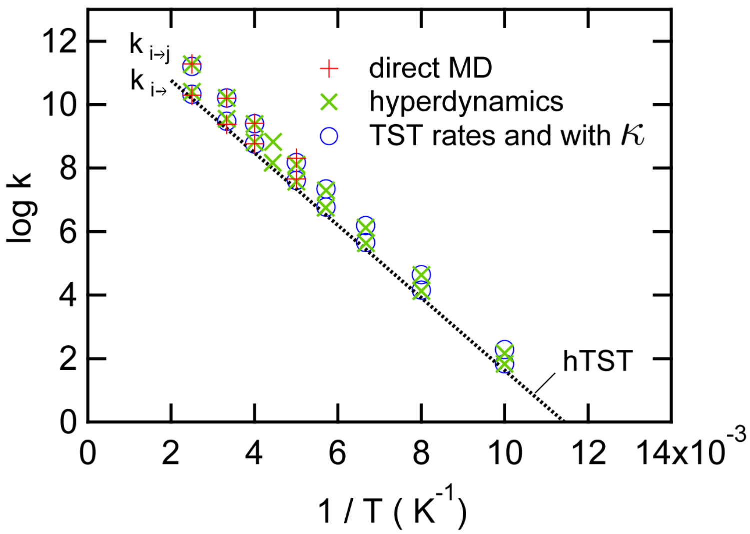

Figure 2.4: Arrhenius plot of the calculated rates ($k_{i\to}^{\mathrm{TST}}$ and $k_{i\to}$) of adatom single exchange mechanism at various temperatures using direct MD (red), bond-boost type hyperdynamics (green), and regular TST calculation with the estimation of $\kappa_{i\to j}$ (blue). The dashed line stands for the harmonic approximated TST rate. The standard errors of the data are small at the presented scale, therefore are not shown in the plot.

2.5.1.2 Al adatom on a relaxed Al(100) surface

When the surface atoms are allowed to move, the diffusion mechanisms become more complicated. In principle there are infinite number of reaction pathways, but only those with thermally accessible transition states can occur within a reasonable timescale.

To calculate $k_{i\to}^{\mathrm{TST}}$, we constructed the dividing surface based upon the relative stretch of bond lengths (the bond is defined for any two atoms within a cutoff distance). Let $\mathbf{r}_a$ denote the position of atom a and $\mathbf{r}_{ab} \equiv \mathbf{r}_a - \mathbf{r}_b$

Table 2.2: Transition state parameters for the Al adatom exchange mechanism on a relaxed Al(100) surface.

T(K)	c^o	$c^\ddagger$	$\Delta G_o^\ddagger$	$\mathrm{k}_{i\rightarrow}^{\mathrm{TST}}$	$\kappa_{i\rightarrow j}$	$\mathrm{k}_{i\rightarrow j}$	$\mathrm{k}_{i\rightarrow j}^{\mathrm{MD}}$	$\mathrm{k}_{i\rightarrow j}^{\mathrm{hyper}}$	$\mathrm{k}_{i\rightarrow j}^{\mathrm{hTST}}$
100	0.15	0.48	0.167	2.29	0.35	1.83	N.A.	1.83	1.64
200	0.23	0.47	0.102	8.17	0.27	7.61	7.66	7.57	7.34
300	0.30	0.44	0.044	10.2	0.18	9.48	9.38	9.36	9.25
400	0.30	0.41	0.041	11.2	0.13	10.3	10.3	10.3	10.2

All the rates are represented in $\log \mathrm{k}$ and $\Delta G_o^\ddagger$ has units of eV.

defines the relative position. $d_{ab} = |\mathbf{r}_{ab}|$ denotes the bond distance and $D_{ab} \equiv (d_{ab} - d_{ab}^0)/d_{ab}^0$ is the relative stretch (or compress if $D_{ab} < 0$) where d_{ab}^0 is the equilibrium length of d_{ab} at a given temperature. It is easy to show that the set $\mathbf{R} = \{\mathbf{r}_{ab} | \forall (a,b), a > b\}$ is more than sufficient to determine the relative configuration of a system. For a given structure, let $\mathbf{D} = \{D_{ab} | \forall (a,b), a > b\}$ be the corresponding set of relative stretches. The hypersurface S_i is defined as:

$$S_i(c) = \{\mathbf{D} | \max(\mathbf{D}) = c\}, \tag{2.41}$$

where $\max(\mathbf{D})$ returns the largest element in $\mathbf{D}$ and c is called the bond-stretching parameter. Each c uniquely defines a hypersurface in which the maximal relative bond stretch, max($\mathbf{D}$) is equal to c. The bond-stretching parameter has been shown in the literature [7] being an useful quantity to characterize the surface diffusion reactions. We first used Eq. (2.19) and (2.20) to calculate $\kappa_{i\rightarrow j}$, $\mathrm{k}_{i\rightarrow}^{\mathrm{TST}}$ and $\mathrm{k}_{i\rightarrow j}$ for the single exchange mechanism [see Fig. 2.5(c)] at various temperatures and compare them with the results obtained from direct MD, hyperdynamics and harmonic TST (Fig. 2.4). The data

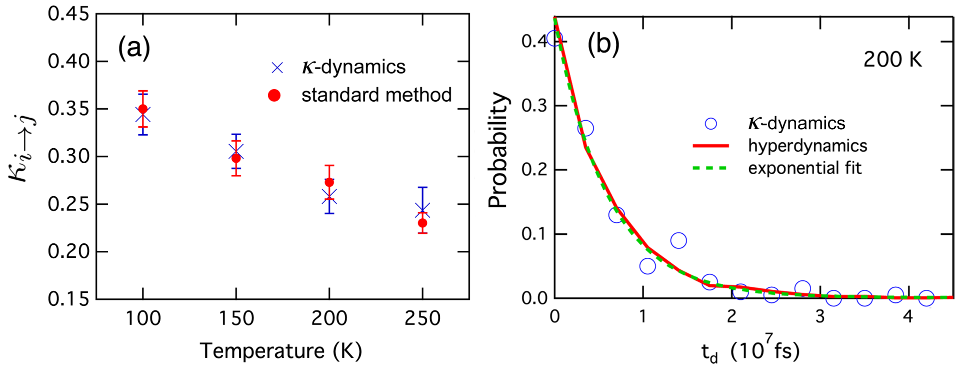

Figure 2.5: (a) The values of $\kappa_{i\to j}$ estimated at various temperatures by using the standard method [Eq. (2.19), red filled circle] and the κ-dynamics shooting scheme [Eq. (2.27), blue cross]. (b) The histogram of t_d at 200 K is calculated from κ-dynamics (open blue circle) and hyperdynamics (solid red line). The single exponential fit (dashed green line) of the hyperdynamics data is also shown in the plot.

points (direct MD, hyperdynamics and TST rate with $\kappa_{i\to j}$) nicely overlay, indicating that the rates are accurately estimated. At high temperature, the harmonic TST rate deviates from the exact rate (11%, 56%, and 85% higher at 30, 100 and 200 K respectively) due to the increase of anharmonicity in the potential energy surface around the saddle point. Some important factors of the calculation are summarized in Table 2.2.

To demonstrate κ-dynamics, we first show that $\langle N\rangle^{-1}$ [Eq. (2.27)] can be used to calculate $\kappa_{i\to j}$ instead of using Eq. (2.19), which is referred to as the standard method. As presented in Fig. 2.5(a), the $\kappa_{i\to j}$ value of single exchange estimated from $\langle N\rangle^{-1}$ agreed with the result obtained by directly calculating the portion of reactive trajectories. In the former scheme, each point and the corresponding error bar were calculated from five independent

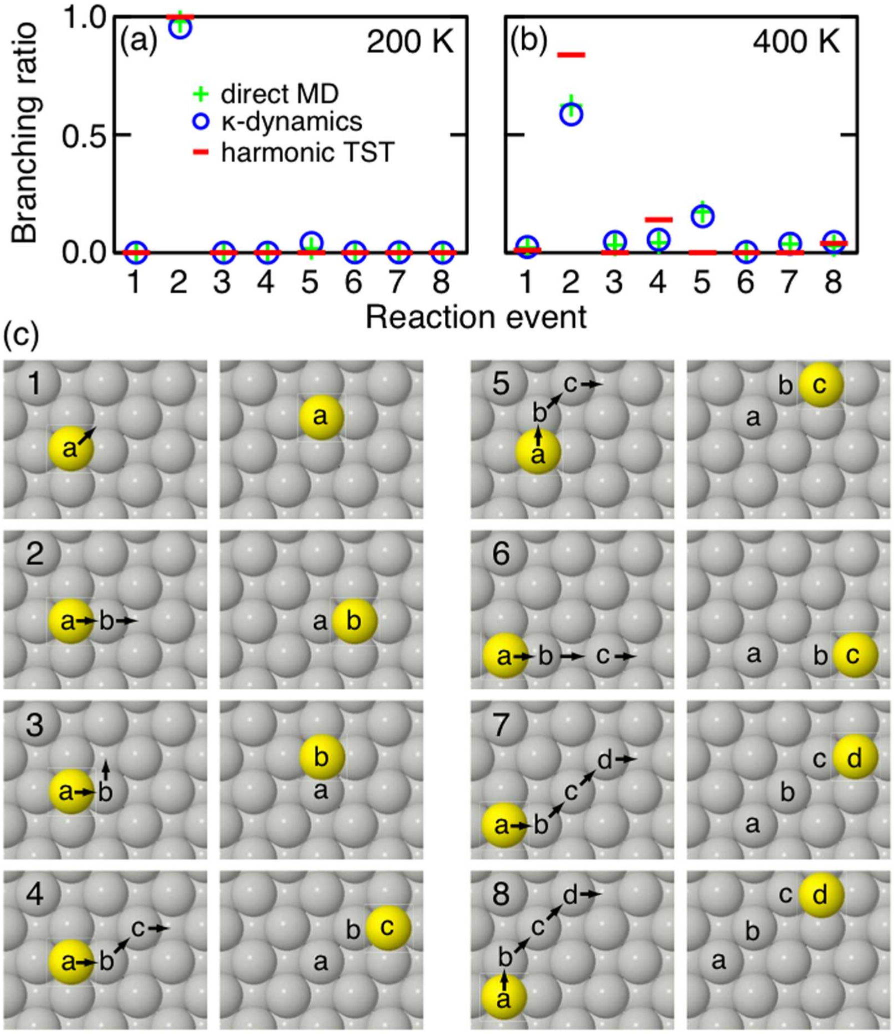

Figure 2.6: The branching ratio for an Al adatom diffusion on relaxed Al(100) surface at 200 (a) and 400 K (b) calculated by using direct MD, κ-dynamics and hTST. The eight most probable adatom diffusion mechanisms on relaxed Al(100) surface are shown in (c). The concerted exchange processes (3, 5, 6, and 7) have no corresponding saddle point; they are only possible because of anharmonicity in the potential energy surface.

values of $\langle N\rangle^{-1}$. Each $\langle N\rangle$ was averaged over 40 independent trials. In the standard method, each data point and the corresponding error bar were obtained from 10 correlation functions. Each correlation function was averaged over 1000 trajectories.

The histogram of t_d at 200 K calculated from κ-dynamics [Eq. (2.29)] and hyperdynamics were compared in Fig. 2.5(b). In the κ-dynamics calculation, 200 independent Ns were used to make the histogram. 5020 independent t_d values were obtained in the hyperdynamics simulation. The single exponential curve nicely fits the hyperdynamics data and thus indicates the system obeys first-order kinetics. The average transition rates obtained from these two histograms are 1.52×10^8 s^{-1} (κ-dynamics) and 1.58×10^8 s^{-1} (hyperdynamics) respectively.

The branching ratios calculated from direct MD, κ-dynamics and harmonic TST were compared in Fig. 2.5(a) and (b). The eight most probable processes for adatom diffusion are shown in Fig. 2.5(c). The exchange mechanism (2) dominates at 200 K. At 400 K, there are significant contributions from other processes, particularly (5) which is a concerted double-exchange. The branching ratio calculated from the κ-dynamics simulation is within statistical uncertainty of direct MD. The harmonic TST branching ratios are significantly different because the concerted exchange processes (3, 5, 6, and 7) have no corresponding saddle point; they are possible only because of anharmonicity in the potential energy surface.

As have shown above, both the t_d distribution and the branching ra-

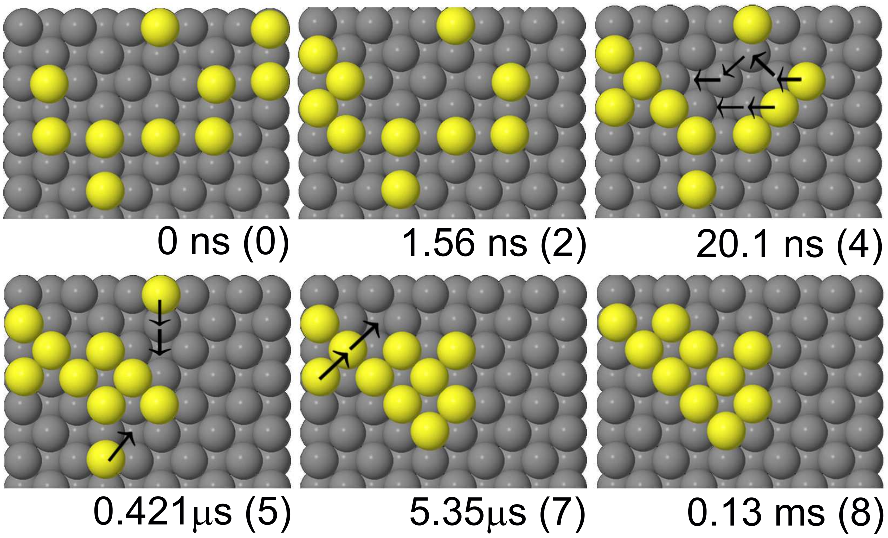

0 ns (0) 1.56 ns (2) 20.1 ns (4)

0.421μs (5) 5.35μs (7) 0.13 ms (8)

Figure 2.7: Selected snapshots of the island ripening dynamics on Al(100) surface simulated by the κ-dynamics algorithm. The yellow spheres are the adatoms. The arrows indicate the direction of displacement. Elapsed times are also shown in the figure and the number in the parenthesis is the number of transitions from the initial configuration.

tios can be accurately predicted. Thus exact dynamical simulations can be achieved by using κ-dynamics. In the following examples, κ-dynamics was utilized to study the dynamics of more complex systems.

2.5.1.3 Island ripening on Al(100) surface

A dynamical simulation of island ripening on the Al(100) surface at 100 K was performed utilizing the κ-dynamics algorithm. Ten adatoms were deposited randomly to make a 20% surface coverage. Adatoms and the atoms in the top four layers were allowed to move. An initial bond-boost TS surface [Eq.(2.41)] was chosen with a value of $c^{\ddagger} = 0.3$. The surface was sampled with replica-exchange using a harmonic constraint. Up to $N_{max} = 200$ independent trajectories were integrated to find a product state. If no successful process was found, the TS surface was pushed toward products by an amount $\Delta c^{\ddagger} = 0.01$ to 0.02. A maximum of $c^{\ddagger} = 0.37$ was required to find a successful trajectory in 200 attempts, corresponding to values of $\kappa_{i\rightarrow}$ greater than 0.005. The time advanced for a given N and $\mathrm{k}_{i\rightarrow}^{\mathrm{TST}}$ are calculated by Eq.(2.24). Snapshots of the dynamics presented in Fig. 2.7 show that the originally separated adatoms aggregate to form a compact island. Some transitions exhibit complex multi-atom rearrangement which is difficult to predict beforehand. It is clear that the concerted rearrangement plays a more important role in surface diffusion than for the single atom motion. The elapsed time shows that a millisecond-scale simulation was successfully achieved in eight transitions. The number of force evaluations in the κ-dynamics simulation corresponds to a MD time of 6.5 μs, giving a acceleration factor of 20.

2.5.1.4 Collapse of a pyramid on Al(100)

As shown in Fig. 2.8, metastable (3×3) square pyramidal cluster is placed upon the Al(100) surface AT 100 K. Using the same method described in the previous example, the TS surfaces with $c^{\ddagger} = 0.3 \sim 0.5$ were sampled. The value of $c^{\ddagger}$ incremented by $\Delta c^{\ddagger} = 0.05$ for every 100 unsuccessful attempts. TST rates were found using umbrella sampling of the $s(\mathbf{x}) = c^{\ddagger}$ surfaces, and the weighted histogram method to find the free energy of the TS with respect to the reactants. 26 transitions were observed before the cluster flattened onto

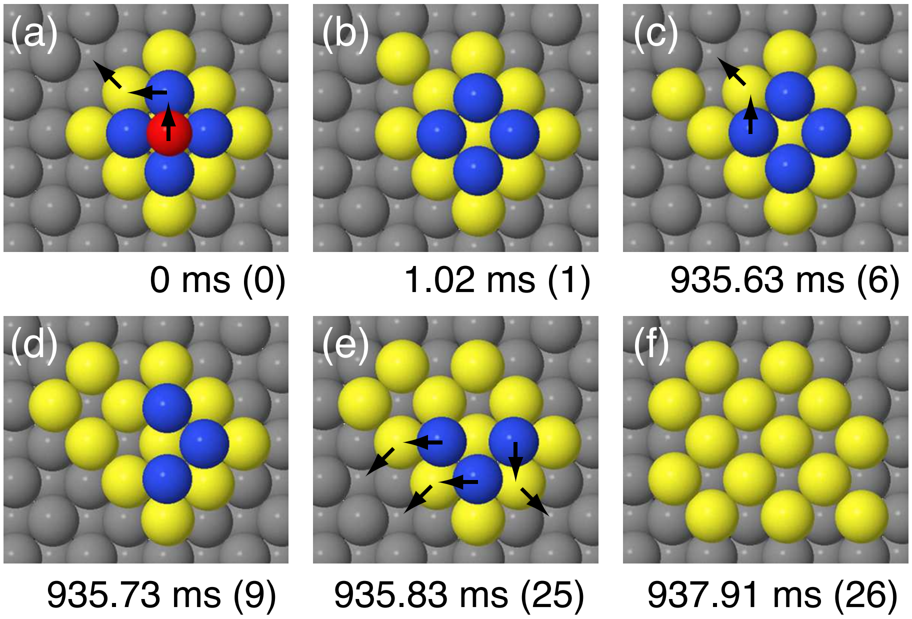

Figure 2.8: Selected snapshots of the collapse of pyramid structure on Al(100) surface simulated by the κ-dynamics algorithm. The yellow, blue and red spheres represent the first, second and third atomic layer above the surface respectively. The arrows indicate the direction of displacement. Elapsed times are also shown in the figure and the number in the parenthesis are the number of transitions from the initial configuration.

the terrace, in a timescale of 0.9 s at 100 K. The transitions in which the atoms descend onto the surface involve concerted exchange events. In the final event three atoms simultaneously descend onto the terrace. The number of force evaluations in the κ-dynamics simulation corresponds to a MD time of 100 μs, giving a acceleration factor of 10^4.

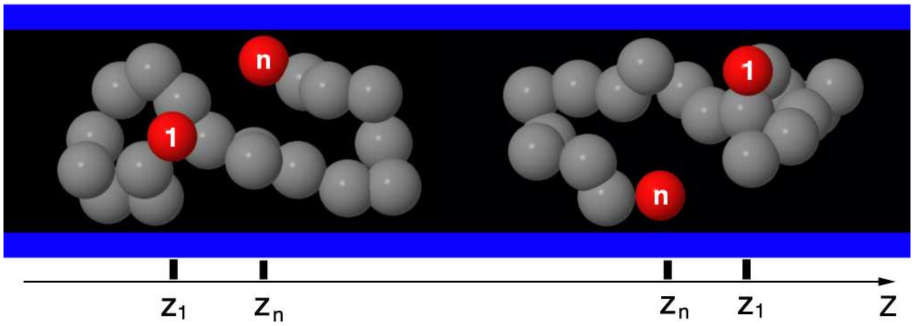

Figure 2.9: Schematic illustration of polymer chain reversal in a infinite pore. The reaction coordinate $z = z_n - z_1$ is defined as the relative distance of the two ends (red beads). The left and right configurations correspond to two different states $z > 0$ and $z < 0$ respectively.

2.5.2 Polymer reversal inside a pore

The theoretical study of polymer chain reversal inside a pore has been reported in the literature. [58] Let the polymer chain (see Fig. 2.9) be described by a series of vectors $\{\mathbf{r}_1, \mathbf{r}_2, \cdots, \mathbf{r}_n\}$ where $\mathbf{r}_i = \{x_i, y_i, z_i\}$ is the position of bead i. And the total number of beads in the chain is denoted by n. The reaction coordinate $z \equiv z_n - z_1$ is defined as the relative z distance between the two ends. The configuration space is partitioned into two ($z_n > z_1$ and $z_n < z_1$) by the dividing surface $z = 0$. Adjacent beads are linked harmonically

$$V_b = \frac{k_b}{2}(|\mathbf{r}_{i+1} - \mathbf{r}_i| - \sigma)^2, \tag{2.42}$$

where the spring constant $k_b = 100\epsilon/\sigma^2$, the parameter ϵ sets the energy scale and σ is the equilibrium bond length.

Interaction between beads other than the adjacent beads is described by a Lennard-Jonnes type potential with an excluded volume term

$$V_{nb} = 4\epsilon \left[\left(\frac{\sigma}{|\mathbf{r}_i - \mathbf{r}_j|} \right)^{12} - \left(\frac{\sigma}{|\mathbf{r}_i - \mathbf{r}_j|} \right)^{6} + \frac{1}{4} \right], \tag{2.43}$$

where $j \geq i + 2$, $|\mathbf{r}_j - \mathbf{r}_i| \geq 2^{1/6}\sigma$ and zero otherwise. The infinite cylindrical pore with radius r_p is described by

$$V_p(\mathbf{r}_i) = 1000\epsilon \left[\frac{(x_i^2 + y_i^2)^{1/2} - r_p}{\sigma} \right]^4, \tag{2.44}$$

for $(x_i^2 + y_i^2)^{1/2} > r_p$ and zero otherwise.

Since the wall is penetrable, the effective radius (denoted as r) will differ from r_p. It has been shown $r \approx r_p + 0.66\sigma$ in the range of parameters chosen.

The motion of polymer chain is governed by Langevin dynamics

$$m\frac{d\mathbf{r}_i}{dt^2} = -\xi \, \frac{\mathbf{r}_i(t)}{dt} - \frac{\partial V}{\partial \mathbf{r}_i} + \tilde{R}(t), \tag{2.45}$$

where $\xi = 2.0(\sigma^2/m\epsilon)^{1/2}$ is the friction coefficient for the beads and $\tilde{R}(t)$ is a Gaussian-distributed white noise.

By definition, there are only two states (namely $z > 0$ and $z < 0$) in this system. The transition rates $\mathrm{k}_{i\rightarrow}$ and the corresponding TST rates $\mathrm{k}_{i\rightarrow}^{\mathrm{TST}}$ as a function of pore size can be estimated from direct MD [Fig. 2.10(a)]. The reversal rate increases with the pore size. The $\kappa_{i\rightarrow}$ values can be estimated directly from $\mathrm{k}_{i\rightarrow}/\mathrm{k}_{i\rightarrow}^{\mathrm{TST}}$. As shown above, the transmission coefficient can also be calculated from the standard method [Eq. (2.19)] and κ-dynamics [Eq.

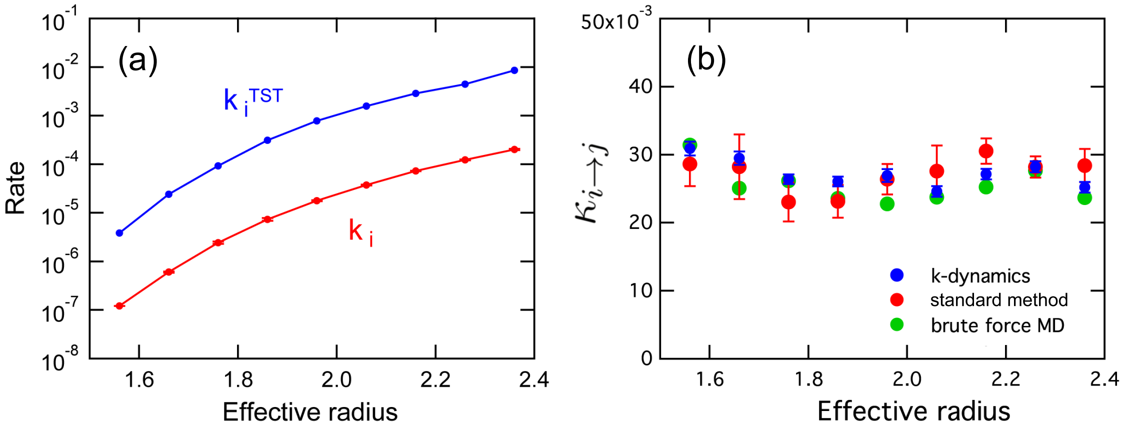

Figure 2.10: (a) $\mathrm{k}_{i\to}$ (red solid circles) and $\mathrm{k}_{i\to}^{\mathrm{TST}}$ (blue solid circles) for polymer chain reversal in pores of various radius calculated using brute force MD simulation. (b) The values of $\kappa_{i\to}$ as a function of effective radius calculated using the κ-dynamics shooting scheme [Eq. (2.27), blue filled circles], standard method [Eq. (2.19), red filled circles] and brute force MD (green filled circles).

(2.27)]. In the regular $\kappa_{i\to}$ calculation, each data point and the corresponding error bar was calculated from eight correlation functions. Each correlation function was averaged over 500 independent trajectories. In the calculation using κ-dynamics shooting scheme, the each data point and the corresponding error bar was calculated from about 90 independent $\langle N\rangle^{-1}$ values. Each $\langle N\rangle^{-1}$ was averaged over 13 independent N values. The $\kappa_{i\to}$ values were summarized in Fig. 2.10(b).

The histogram of t_d calculated from κ-dynamics [Eq. (2.29)] and brute force MD for the system with an effective radius of 2.16 were compared in Fig. 2.11. In the κ-dynamics calculation, 1000 independent Ns were used to make the histogram. 2×10^4 independent t_d values were obtained in the direct MD

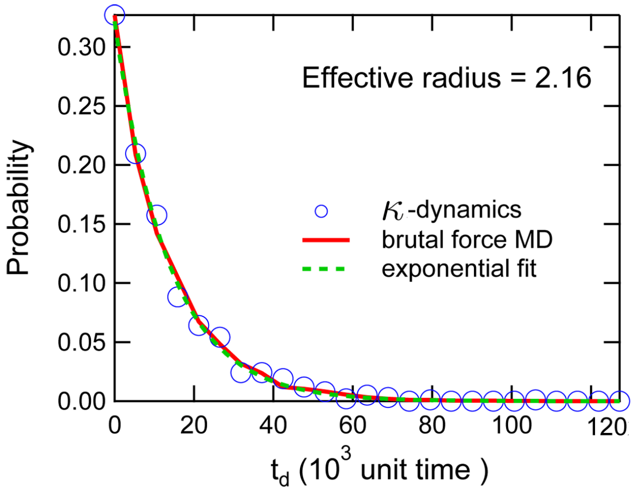

Figure 2.11: Comparison of the t_d distribution calculated from brute force MD (red solid curve) and κ-dynamics (open blue circle) simulations for polymer chain reversal in a pore of effective radius 2.16. The single exponential fit (dashed green line) of the MD data is also shown in the plot.

simulation. The single exponential curve nicely fit the brute force MD data and thus indicates the system obeys first-order kinetics. The average transition rates obtained from these two histograms are 7.27×10^{-5} s^{-1} (κ-dynamics) and 7.24×10^{-5} s^{-1} (MD) respectively.

2.6 Conclusion

The primary limitation of the κ-dynamics method is the need to identify a suitable reaction coordinate that separates reactants from products. In cases where the reactive events involve bond breaking, the bond stretch reaction coordinate of Eq.(2.41) makes sense, but, for example, in conformational rearrangements of biomolecules, the choice of a good reaction coordinate is far less intuitive. Fortunately, the assumed reaction coordinate does not need to be optimal. The κ-dynamics trajectories from the TS are typically very short for systems with low values of $\kappa_{i\rightarrow}$. For example, if 10^6 trajectories can be integrated, a TS with $\kappa_{i\rightarrow} = 10^{-6}$ is acceptable. Furthermore, a flexible TS can be used to maximize $\kappa_{i\rightarrow}$.

Two other computational details are worth noting. First, each part of the algorithm is implemented in parallel, including sampling the TS to find equilibrium crossing points; the use of multiple replicas and replica exchange to enhance sampling; and following trajectories from the TS. N_{max} is limited only by the number of processors available for the calculation. Second, the state-to-state trajectory, which is typically the most interesting aspect of the calculation, can be found at a fraction of the total computational work. Generating a trajectory requires sampling the TS and finding a single successful short-time trajectory out of each state visited. Then, as much computational effort as desired can be used to determine $\mathrm{k}^{\mathrm{TST}}$ and the time for each transition in the trajectory. An order of magnitude estimate requires less computational work than a precise time history.

Chapter 3

Effect of finite trajectory length on the correlation function analysis of single molecule data

3.1 Abstract

The effect of finite trajectory length on single molecule rotational correlation functions has been studied by utilizing time series analysis and numerical simulations. Correlation functions obtained from the trajectories of length less than 100 times the correlation time constant (τ_ℓ) exhibit significant deviations from the true correlation function. The distributions of sample time constants (τ_F) and stretching exponents (β_F) are mapped by fitting a large number of rotational trajectories to stretched exponentials. As the trajectory length gets smaller, the distributions become broader and asymmetric and their mean values deviate from the true value predicted by pure rotational diffusion. Analysis based on higher order spherical harmonics is suggested as a method for minimizing the effect of the trajectory length. The distributions of time constants for different higher order spherical harmonics are also compared. While the focus of the paper is on rotational correlation functions, the general conclusions apply to any dynamical process that yields an exponentially decaying correlation function.

3.2 Introduction

Single molecule spectroscopy (SMS) is a powerful tool for probing biological and material systems. [59, 60, 12, 61, 62] The great advantage of SMS over conventional spectroscopic methods is the ability for SMS to directly measure distributions of properties rather than only their ensemble averaged values. Single molecule methods rely on repeated measurements of the same molecule over time yielding a trajectory of intensity, emission frequency, polarization, or other properties. An effective method for analyzing such a time series is correlation function analysis. While this method is a powerful tool for extracting time scale of a fluctuating property, it can be severely limited by the length of the observation time. As many single molecule experiments rely on fluorescent dyes, the length of the trajectories can be relatively short as the result of photochemistry. This short trajectory length can lead to large errors in estimating the true correlation function. For a SMS experiment, this implies that even in the absence of any sample heterogeneity there will be an inherent distribution of correlation functions measured for different molecules and that this distribution will strongly depend on the length of the trajectories. In this paper we will examine the effect of finite trajectory length on the correlation function analysis of single molecule trajectories for rotational diffusion. For simplicity we will examine trajectories for isotropic diffusion with a single rotational constant. Experimentally, single molecule rotation can be studied either by measuring a projection of the transmission dipole moment polarization, denoted as the reduced linear dichroism, [63, 64, 65] or by measuring the three-dimensional (3D) orientation of the transmission dipole. [66, 67, 68, 69, 70] With the use of high numerical aperture objectives utilized in single molecule experiments, it has been shown that the correlation functions of the dichroism signal yield decays that are equivalent to the rotational correlation function (RCF) for the $\ell = 2$ spherical harmonic. [64] With trajectories of the angles from the full (3D) orientation of the molecule, it is possible to calculate any RCF that corresponds to an even Legendre polynomial. For isotropic diffusion, each RCF is a single exponential decay whose decay time depends only on the rotational diffusion constant and the order of the correlation function. As such, measuring any RCF yields equivalent information. However, for more complex dynamics, measuring different RCFs is essential. [71] In this paper we will examine how the effects of finite trajectory length on the decay of the RCFs translate into distributions of decay times. Also, rotational relaxation in many systems is often analyzed with stretched exponential functions. [72, 73] We will also explore how the distribution of correlation function decays manifests itself in distributions of the stretching exponent. This will be accomplished through a combined approach of statistical time series analysis and a simulation of single molecule rotational trajectories.

3.3 Analysis and simulation methods

In many research areas, time series analysis has been widely used to evaluate the probability structure of the system under study. If a system is at statistical equilibrium, or in a stationary state, then the probability structure of the system can be simply characterized by its lower moments of probability distribution, namely, mean (μ), variance (σ^2), and covariance function (γ). [74, 75] For a given series of experimental observations $\{X_t; t = 1, 2, 3, \ldots\}$, if the stationarity is satisfied, its covariance function can be defined as the following:

$$\gamma(k) = E[(X_t - \mu)(X_{t+k} - \mu)], \tag{3.1}$$

where $E(\cdot)$ denotes the expectation value, $\mu = E(X_t)$, and $\gamma(0) = E[(X_t - \mu)^2] = \sigma^2$. One of the important features of a stationary system is that it does not matter what reference point we choose [i.e., t in Eq. (3.1)]. The value of covariance function depends only on the time lag k. The normalized form of covariance function, or the so-called correlation function, is defined as

$$\rho(k) = \gamma(k)/\gamma(0), \tag{3.2}$$

which is useful when comparing data with different scales. In theory, an infinite number of data points are required to calculate the true covariance and correlation functions; however, in a real measurement, the data size is always limited. The correlation function can be estimated from a finite time series using an estimator. Equation (3.3) is the most commonly used correlation function estimator:

$$\hat{P}(k) = \frac{\sum_{t=1}^{T-k}(X_t - \bar{X})(X_{t+k} - \bar{X})}{\sum_{t=1}^{T}(X_t - \bar{X})^2}, \tag{3.3}$$

where T and $\bar{X}$ are sample size and sample mean, respectively. For a specific estimate, $\hat{\rho(k)}$ is usually called the sample correlation function. The estimator in Eq. (3.3) is biased, but when $T \to \infty$, it will asymptotically yield a normal distribution about a mean that is the true correlation function ρ. The distribution will be governed by a covariance matrix C_{ij} which can be calculated from Bartlett's formula: [75]

$$C_{ij} = \frac{1}{T}\sum_{t=1}^{\infty}[\rho(t+i)\rho(t-i) - 2\rho(t)\rho(i)] \times [\rho(t+j)\rho(t-j) - 2\rho(t)\rho(j)]. \tag{3.4}$$

Of particular interest is the variance at any lag k:

$$\sigma^2 = C_{kk} = \frac{1}{T}\sum_{t=1}^{\infty}[\rho(t+k)\rho(t-k) - 2\rho(t)\rho(k)]^2. \tag{3.5}$$

Since Eq. (3.3) sums up only to $t = T - k$, there is no way to evaluate the values beyond $\rho(T-1)$ without further information. Also, the number of pairs $(X_t - \bar{X})(X_{t-k}\bar{X})$ used to calculate the sum decreases with k. This implies that estimations for large k will be unreliable. It is suggested by Box and Jenkins that $T > 50$ and $k < T/4$ are required. [76] Rotational motion of molecules has been intensively studied in a wide variety of media. [77, 78, 79] The model used to describe the rotation depends strongly on the nature of the matrix. In the gaseous phase, for example, the molecules rotate inertially in specific direction until collision with another molecule. The occurrence of big jumps in angle decorrelates the orientational properties. But in the condensed phase, where the collisions are much more frequent, the trajectory is composed of small, independent hops, and the system can be described by rotational diffusion. In the case of molecular probes embedded in the condensed matrix, the rotational motion can be approximately seen as a diffusive process, and it is mathematically equivalent to the random walk on the surface of a sphere. [80] In this case, the probability propagator $K(\Omega, \Omega_0; t)$ [Eq. (3.6)] can be expressed in terms of spherical harmonics $Y_{\ell,m}(\Omega)$, where Ω_0 and Ω represent the solid angles at times 0 and t, respectively,

$$K(\Omega, \Omega_0; t) = \sum_{\ell,m} Y^*_{\ell,m}(\Omega) Y^*_{\ell,m}(\Omega_0) e^{-\ell(\ell+1)D_{rot}t}, \tag{3.6}$$

where D_{rot} is the rotational diffusion coefficient. The correlation function with respect to rank ℓ at time lag k can be calculated by averaging the joint probability over all solid angles, and then normalized by the same quantity at $k = 0$:

$$\begin{aligned} \rho_{\ell,m,\ell',m'}(k) &= \frac{\langle \ell', m', \Omega | K(\Omega, \Omega_0; k) | \ell, m, \Omega_0 \rangle_{\Omega,\Omega_0}}{\langle \ell', m', \Omega | K(\Omega, \Omega_0; 0) | \ell, m, \Omega_0 \rangle_{\Omega,\Omega_0}} \\ &= e^{-\ell(\ell+1)D_{rot}k} \delta_{\ell,\ell'} \delta_{m,m'} = \rho_\ell(k). \end{aligned} \tag{3.7}$$

The result turns out to be a single exponential decay of time constant $\tau_\ell \equiv [\ell(\ell+1)D_{rot}]^{-1}$. The rotational diffusion in a homogeneous environment can be simulated by taking random walks on the surface of a unit sphere. Instead of using Eq. (3.6), we adopt the flat-plane approximation [81] to generate a small displacement on the curved surface. The validity of this approximation depends on the size of the steps as determined by the magnitude of the diffusion constant. It can be shown that this assumption is valid as long as $D_{rot} < 0.1$ ($\tau_1 > 5$). In the simulation the direction of each step is chosen randomly from $[0, 2\pi]$, and the probability of moving a distance r within a unit time interval is given by

$$K(r) = \frac{r}{2D_{rot}} e^{-r^2/4D_{rot}}. \tag{3.8}$$

By using the rejection method, [82] displacements with the desired probability distributions can be generated, and the resulting coordinates of each step are used to calculate the corresponding $Y_{\ell,m}(\Omega)$ value. Equation (3.3) can be used to calculate any rotational correlation function from the angular trajectories. The average value $\bar{X}$ can be calculated for any given trajectory. However, since $\langle Y_{\ell,m} \rangle_\Omega = 0$ for all $\ell > 0$ and m, we replace $\bar{X}$ by its expectation value $E(X) = 0$ to reduce the uncertainty in estimating the correlation functions. We will use this modification of Eq. (3.3) in the following calculations. This implies that rotational diffusion is somewhat of a specialized case as one knows a priori the true mean of the time series. Analysis of other processes in which this information is not known will lead to even greater uncertainties than those presented here.

One frequently used method to characterize the relaxation is to fit the curve with the stretched exponential function: $\exp[-(k/\tau_F)^{\beta_F}]$. [72, 73] From this the two parameters τ_F and β_F can be obtained. The fitting process is carried out by the method of least squares with the constraint τ_F, $\beta_F \geq 0$. The curve is fitted up to time lag k_U, where the function itself is equal to the standard deviation, i.e., the difference between $\hat{\rho}(k_U)$ and zero is smaller than the range of fluctuation. [76] We should note that the purpose of using a stretched exponential is only to quantify the deviation from single exponential decay. There is no indication that the correlation function should inherently be a stretched exponential decay. Also, there is no constraint other than τ_F, $\beta_F \geq 0$ applied in the fitting. We found that more limitations, such as $\beta_F \leq 1$, artificially alter the distribution of τ_F and β_F and thus are not adopted in our fitting routine. By plugging Eq. (3.7), $\rho(k) = \exp(-k/\tau_\ell)$, into Eq. (3.5), we can obtain the variance as a function of time lag k:

$$\begin{aligned} \sigma^2(k) &= \frac{1}{T}\left\{\coth\left(\frac{1}{\tau_\ell}\right)[1-e^{-2k/\tau_\ell}] - 2ke^{-2k/\tau_\ell}\right\} \\ &= \frac{1}{\bar{T}}[\alpha(1-e^{-2\bar{k}}) - 2\bar{k}e^{-2\bar{k}}], \end{aligned} \tag{3.9}$$

where $\bar{k} \equiv k/\tau_\ell$, $\bar{T} \equiv T/\tau_\ell$, and $\alpha \equiv \coth(1/\tau_\ell)/\tau_\ell$. When $\tau_\ell > 5$, $\alpha \approx 1$, and both $\rho(k)$ and $\sigma^2(k)$ can be reduced to the standard forms in a normalized scheme (i.e., $k \to \bar{k}$, $T \to \bar{T}$) which is τ_ℓ independent,

$$\sigma^2(k) \approx \frac{1}{\bar{T}}[1-(1+2\bar{k})e^{-2\bar{k}}] \text{ for } \tau_\ell > 5. \tag{3.10}$$

Another way to interpret the τ_ℓ independence in Eq. (3.10) is that the magnitude of variance is determined only by T/τ_ℓ. The key point of reducing the variance is to make longer measurement and not to increase density of trajectory once τ_ℓ is larger than five units. This implies that the dynamic range of the experiment can be optimized by utilizing time bins such that the decay time is not significantly larger than five time units. Given a limited number of photons emitted from a single molecule, it is better to spread them out over a longer period of time rather than measuring fine time points. Alternatively, as will be discussed later, it is possible to calculate higher order RCFs with shorter time constants to maximize the effective trajectory length. However, one should note that with fewer points present in the decay, it is more difficult to fit, and the information from faster dynamics might be lost. In practice, the frequency of acquiring data depends on the case under study, and compromises always exist. In the later discussion, while τ_ℓ is always chosen to be larger than 5, the specific choice of time constant has no effect on the analysis.

3.4 Results and discussion

3.4.1 The sample distribution in the correlation function space

In the following discussion, we focus on the case $\ell = 1$ [i.e., $\{X_t\} = \{\cos\theta_t\}$, $\tau_1 = (2D_{rot})^{-1}$] without losing any generality, even though the most commonly measurable term is $\ell = 2$. First, we use the method described above to generate a single rotational trajectory of length T and its $\ell = 1$ spherical harmonic component. Next, we used Eq. (3.3) together with the condition that $\bar{X} = 0$ to calculate the correlation function. Figure 3.1 shows a typical sample correlation function of $\tau_1 = 200$ and $T = 500\tau_1$ and its corresponding trajectory. The correlation function is shown on a semi-log scale to emphasize the decay. The correlation function is fitted in the statistically significant region as previously described. For this trajectory, the estimated correlation function happened to be nearly identical to the true value.

Figure 3.2 compares two sample correlation functions of $T = 10\tau_1$ and $1000\tau_1$. Qualitatively it is easy to observe a number of representative differ-

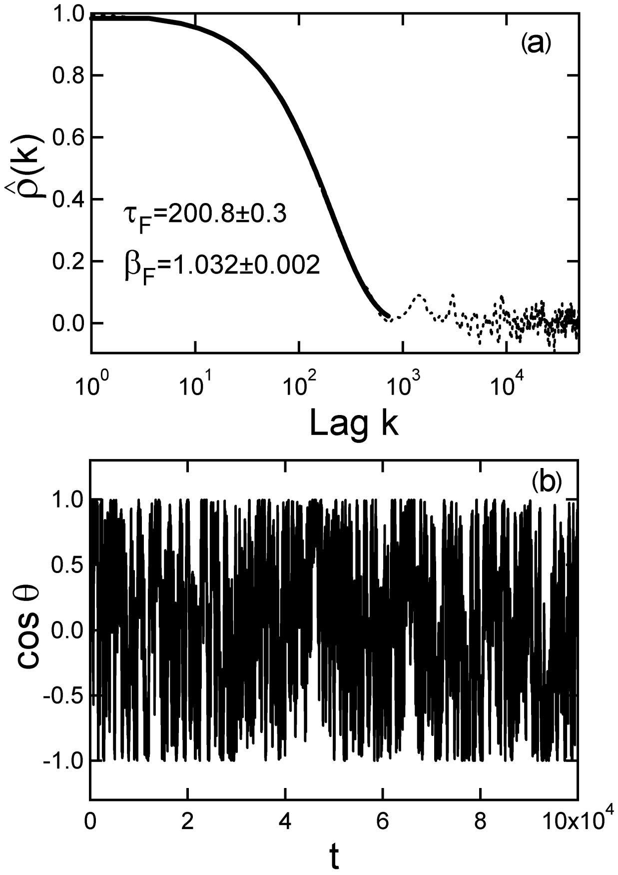

Figure 3.1: (a) Sample correlation function ($\ell = 1$, dashed line) calculated from (b) simulated rotational trajectory of size $T = 500\tau_1$. The result of the stretched exponential fit (solid line) gives $\tau_F \approx 200.8 \pm 0.3$ and $\beta_F = 1.032 \pm 0.002$, which agrees with the original settings: $\tau_1 = 200$ and $\beta_1 = 1$.

ences in the decays that result from the length of the trajectory. The correlation function for the longer trajectory, Fig. 3.2(a), has fewer fluctuations, and a larger portion of the decay has points with statistical significance. The fit is again nearly identical to the true correlation function. The decay time 197.3 ± 0.3 compared to the true value of 200, and the stretching exponent

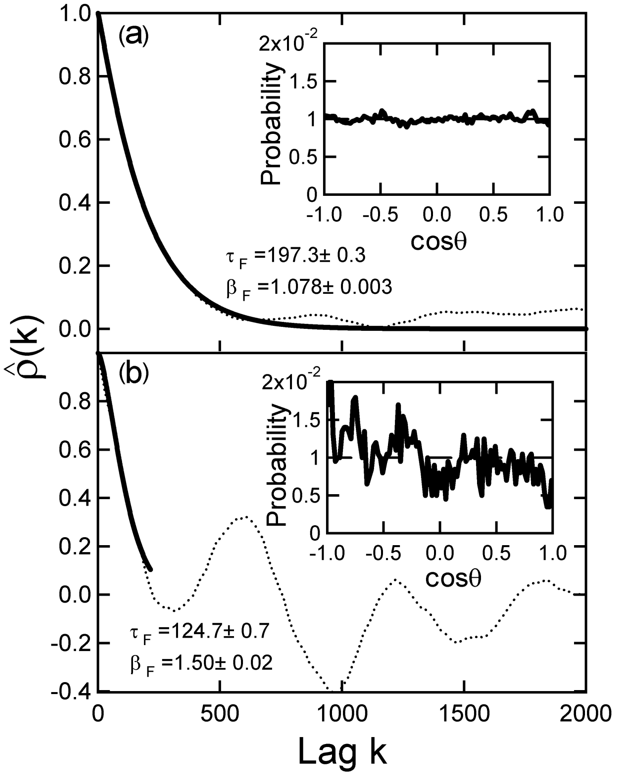

Figure 3.2: Sample correlation functions ($\ell = 1$, $\tau_1 = 200$) obtained from trajectories of different sizes: (a) $T = 1000\tau_1$ and (b) $T = 10\tau_1$. The stretched exponential fits (solid line) and the corresponding τ_F and β_F values are also shown. The insets give the probability distributions of $\cos\theta$, which exhibit great fluctuations as T gets smaller.

is 1.078 ± 0.003 compared to the true value of $\beta_1 = 1$. The shorter trajectory yields a significantly worse estimation of the true correlation function, as shown in Fig. 3.2(b). The decay has more fluctuations and fewer points above the noise. The fit yields a decay time of 124.7 ± 0.7 with a stretching exponent of 1.50 ± 0.02. The difference between the fit and the true value is not a result of poor fitting or a noisy function. The fit is an excellent representation of the

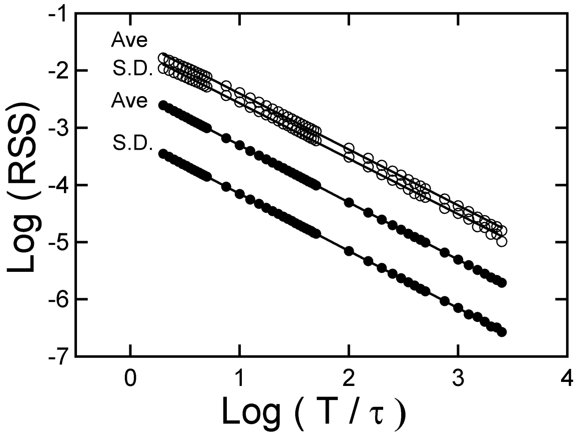

Figure 3.3: The average (Ave) and the standard deviation (S.D.) of residual sum of squares (RSS) plotted as a function of trajectory size T. The results of two different dynamics: rotational diffusion ($\ell = 1$, $\tau_1 = 200$, open circles) and random jumps within $[-1, 1]$ (filled circles) are compared. The solid lines are the corresponding linear fits which show close agreement with straight lines of slope (-1). The averages and standard deviations are calculated from pieces of given size (T) that are generated by breaking a long trajectory (10^7 points). Each point on the plot is the result of averaging ten different such long trajectories.

decay. The problem is that the short trajectory provides a poor estimation of the true correlation function. The insets shown in Fig. 3.2 are the probability distributions of $\cos\theta$. As the $T \to \infty$, the probability will be evenly distributed, i.e., all values of $\cos\theta$ are equally sampled. However, for a given trajectory of finite size T, the distribution is not perfectly flat. The residual sum of squares (RSS) calculated from the difference between sample and true probability will increase as T becomes shorter.

Figure 3.3 shows the log(RSS) vs $\log(T/\tau_1)$ for the rotational trajectories (open symbols). The linear trend with a slope of -1 implies an inverse

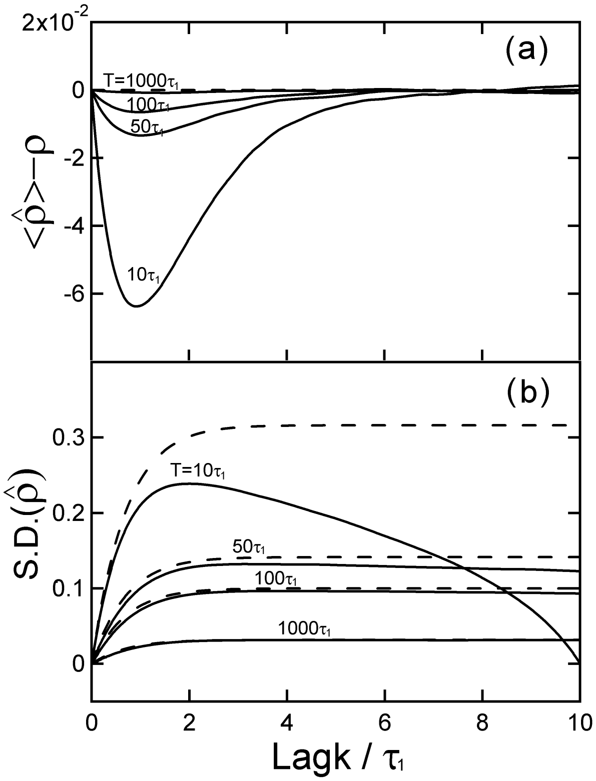

Figure 3.4: (a) The difference between the average value of the sample correlation functions and the true correlation function and (b) the standard deviation of sample correlation functions plotted vs lagk/τ_1. The solid lines are the simulated results ($\ell = 1$, $\tau_1 = 200$) of different Ts and the dashed lines are predictions based on Bartletts formula. Each line is calculated from 5×10^4 different trajectories.

relation. Figure 3.3 also shows a comparison of the rotational diffusion to trajectories of random jumps within $[-1, 1]$ (solid symbols). It is not surprising that the rotational diffusion and random jumps follow the same relation: RSS$\propto 1/T$. However, because the points in a rotational trajectory are not totally independent, the RSS is larger than that of a random trajectory for any given T. We should note that the relative standard deviation of RSS is also bigger for rotational diffusion, which means that the variation of RSS between different trajectories is larger in rotational diffusion than in a random scheme. This indicates that the properties of rotational diffusion will depend highly on the trajectory chosen. This effect plays an important role in the sample distribution of properties of rotational diffusion, and we will see more examples in the later discussion.

Bartlett's formula, Eq. (3.5), predicts the asymptotic behavior of correlation functions at large T. In order to check the validity of the formula, a large number of trajectories of a given size were generated and their correlation functions were calculated. Figures 3.4(a),3.4(b) show the standard deviation and the difference between sample and true correlation function as a function of time lag k/τ_1. It is important to note that the key variables are the time lag k and the total trajectory length T normalized to the time constant τ_1. By comparing the simulation results with the predictions from Bartlett's formula, considerable deviations are observed. Figure 3.4a shows that when the trajectories are shorter than 1000 times the decay time, the distribution of correlation functions does not have the true correlation function as the mean. The mean of the estimated correlation functions always underestimates the correlation at small time lag. This deviation gets smaller as T increases. Figure 3.4(b) shows the difference between the standard deviation of the estimated correlation function compared to the standard deviation from Bartlett's formula. There are again deviations when the length of the trajectory is less than 1000 times the decay time.

There are two different reasons that account for these deviations. If we go back to Eq. (3.3), the estimator of the correlation function is composed of two different parts: the estimations of $\gamma(k)$ and $\gamma(0)$. One commonly used covariance function estimator can be written as

$$\hat{\Gamma}(k) = \frac{1}{T}\sum_{t=1}^{T-k}(X_t - \bar{X})(X_{t+k} - \bar{X}). \tag{3.11}$$

The correlation function estimator in Eq. (3.3) can be expressed in terms of Eq. (3.11):

$$\hat{P}(k) = \frac{\hat{\Gamma}(k)}{\hat{\Gamma}(0)}. \tag{3.12}$$

It can be shown that Eq. (3.11) itself is a biased estimator [74] with the expectation value of the estimator being

$$E[\hat{\Gamma}(k)] = \left(1 - \frac{k}{T}\right)[\gamma(k) - var(\bar{X})]. \tag{3.13}$$

where $var(\cdot)$ denotes the variance. If we set $\bar{X} = 0$, the deviation results only from the scaling factor of $(1-k/T)$. This is not a surprise, as the scaling factor is a consequence of the “zero filling” effect. Since the summation in Eq. (3.11) only includes $(T-k)$ terms, it will underestimate the covariance if $k \neq 0$. For Eq. (3.12), the expectation value of the correlation function estimator will be roughly proportional to $(1-k/T)$. This effect accounts for a large part of the deviation found in Fig. 3.2(a). The actual expectation value of Eq. (3.12) is required to provide a more precise description of the deviations.

As for the standard deviation, a considerable zero filling effect was found in small T case, as seen in Fig. 3.4(b) where $T = 10\tau_1$. A first approximation to describe this deviation is to assume that the sample standard deviation will have the same scaling factor as the correlation function, i.e., $(1 - k/T)$. The zero filling effect will reduce the effective size from T to $(T - k)$. According to Bartlett's formula, the standard deviation increases as a factor of $\sqrt{T/T - k}$. Thus, the combination of these two effects gives us a total factor: $\sqrt{(T - k)/T}$. This approximate relation can be used to explain the deviation in Fig. 3.4(b) for large T cases. If T is small ($< 50\tau_1$), more accurate equations are needed. Regardless of specific causes for the deviations, Fig. 3.2 demonstrates that the estimation of correlation function from samples with finite size systematically deviates from the true correlation function. For example, when $T = 10\tau_1$, there is about an 18% error (estimated at $k = \tau_1$), which greatly affects the distribution of decay constants.

3.4.2 The sample distributions in the τ_ℓ and β_ℓ spaces

In the real experiments, the data are seldom compared directly in the correlation function space. A more useful method is to fit the correlation function with the stretched exponential, from which two parameters τ_F and β_F can be obtained for further analysis. The previous section has demonstrated how finite trajectories lead to a distribution of correlation functions. Here we can see how this distribution propagates in the τ_ℓ and β_ℓ spaces. To map the distributions, large numbers of trajectories of given size were generated, their

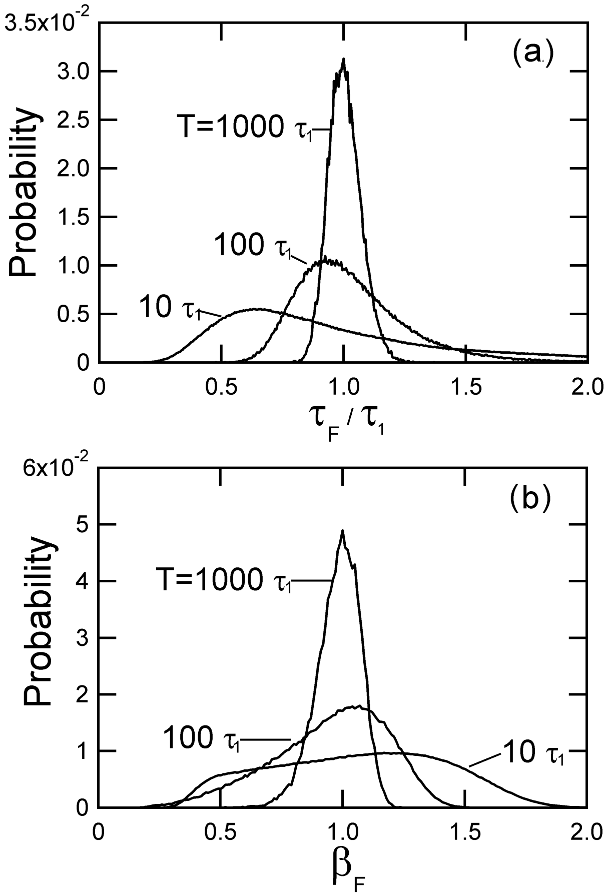

Figure 3.5: Distributions of (a) τ_F and (b) β_F with respect to different Ts ($10\tau_1$, $100\tau_1$, and $1000\tau_1$). Each curve is calculated from 1000 trajectories ($\ell = 1$, $\tau_1 = 200$, length 10^7 broken into pieces of desired size T.

correlation function calculated, and then fitted with stretched exponentials. According to the law of large numbers, τ_F and β_F will approach their theoretical distributions. Figures 3.5(a), 3.5(b) are the resulting distributions obtained from the simulated trajectories of sizes $T = 10^3\tau_1$, $10^2\tau_1$, and $10\tau_1$. It is obvious that as T decreases, both the distributions of $\{\tau_F\}$ and $\{\beta_F\}$

are broadened and the shapes become asymmetric. For $\{\tau_F\}$, its distribution has a positive tail and the most probable τ_F shifts to the smaller side of τ_1. The degree of skew becomes larger as T gets smaller. However, the $\{\beta_F\}$ distribution tails at the opposite side, and the most probable β_F is larger than 1. Unlike $\{\tau_F\}$, the negative tail of $\{\beta_F\}$ is limited by the condition $\beta_F > 0$, hence the shape of the $\{\beta_F\}$ distribution shows deformation while T is small. Limiting β_F to $0 < \beta_F \leq 1$ yields distributions that are obviously truncated by the criterion $\beta_F \leq 1$.

In order to know how $\{\tau_F\}$ and $\{\beta_F\}$ change as a function of T, we plot the average and standard deviation of $\{\tau_F\}$ and $\{\beta_F\}$ at different Ts in Figs. 3.6(a) and 3.6(b). For large $T(> 100\tau_1)$, the average of $\{\tau_F\}$ is approximately the true τ_1. When T is smaller than $100\tau_1$, the tailing effect of distribution is significant and the average value becomes larger than the true value. If T gets even smaller than $20\tau_1$, the zero filling effect dominates. As a result, both the average and the standard deviation decline rapidly and monotonically. As for $\{\beta_F\}$, the trend is similar in the region $T > 20\tau_1$, but since the tailing of distribution is in the opposite direction, the average of $\{\beta_F\}$ will be less than 1. However, compared to τ_F, β_F is much more sensitive to the shape of the curve. When $T < 20\tau_1$, the zero filling effect becomes significant. As a consequence, the suppression of the function together with the fluctuations at large k make the curve easily pass through zero rather than gradually approaches it, and β_F turns out to be larger than 1 [see Fig. 3.2(b) for example].

The most important feature of Fig. 3.6 is that there is always a distri-

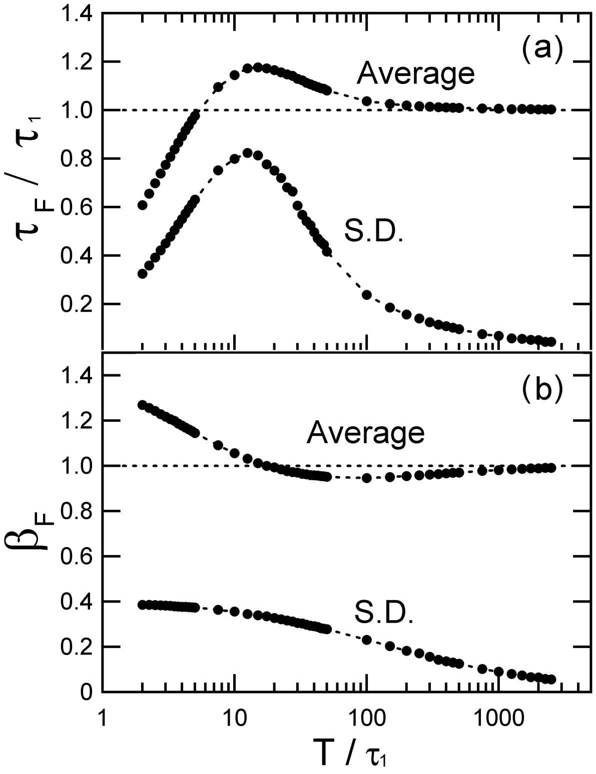

Figure 3.6: The average and standard deviation of (a) τ_F/τ_1 and (b) β_F as a function of T/τ_1. Each point is calculated from a long trajectory ($\ell = 1$, $\tau_1 = 200$, length 10^7 broken into pieces of desired size T, and the resulting value is the average of ten different long trajectories.

bution in τ_F and β_F, even for a system in which the dynamics yield a perfect single exponential correlation function. Even for T as large as $1000\tau_1$, the standard errors of τ_F and β_F are about 10% when compared with τ_1 and β_1. If the lengths of the trajectories obtained from the experiment are less than $50\tau_1$, the range of τ_F and β_F will be enormous. A simple method to estimate the average and standard error of $\{\tau_F\}$ in the region $T/\tau_1 > 100$ is to fit the curves $\rho_{\pm}(k) = \rho(k) \pm \sigma(k)$, where $\sigma(k)$ is given by Eq. (3.5). The values of $(\tau_{F_+} + \tau_{F_-})/2$ and $(\tau_{F_+} - \tau_{F_-})/2$ are close to the simulated average and standard error at any given T. When T is less than $100\tau_\ell$, this method does not accurately predict the true average or standard deviation of τ_ℓ. For $\{\beta_F\}$, this method gives much poorer predictions for all trajectory lengths and is not recommended.

The large standard error of τ_F and β_F can be attributed to the correlation function itself. Since any point in the rotational trajectory is not totally independent of the adjacent points, one can expect the way in which the trajectory evolves to be related to its history. In other words, if the total length T is not long, the resulting sample correlation function will depend highly on the specific trajectory. The way deviations at different lags correlate with each other can be seen by examining their covariance function Eq. (3.4). Plugging the correlation function $\rho(k) = \exp(-k/\tau_\ell)$ into Eq. (3.4), we obtain the covariance of the correlation deviations $[\hat{\rho}(k) - \rho(k)]$ at time lag $k = i$ and $j (j > i)$:

$$\begin{aligned} C_{ij} &= \frac{e^{-j/\tau_\ell}}{T}\left[e^{i/\tau_\ell}\left(j-i+\frac{1}{e^{2/\tau_\ell}-1}\right)-e^{-i/\tau_\ell}\left(j+i+\frac{1}{e^{2/\tau_\ell}-1}-\sum_{k=1}^{i} e^{2k/\tau_\ell}\right)\right] \qquad (3.14) \\ &= \frac{e^{-j/\tau_\ell}}{T}\left[e^{i/\tau_\ell}\left(j-i+\frac{1}{e^{2/\tau_\ell}-1}\right)-e^{-i/\tau_\ell}\left(j+i+\frac{e^{2/\tau_\ell}+1-e^{2(i+1)/\tau_\ell}}{e^{2/\tau_\ell}-1}\right)\right], \end{aligned}$$

especially

$$C_{1j} = \frac{2j}{T} \sinh\left(\frac{1}{\tau_\ell}\right) e^{-j/\tau_\ell}. \qquad (3.15)$$

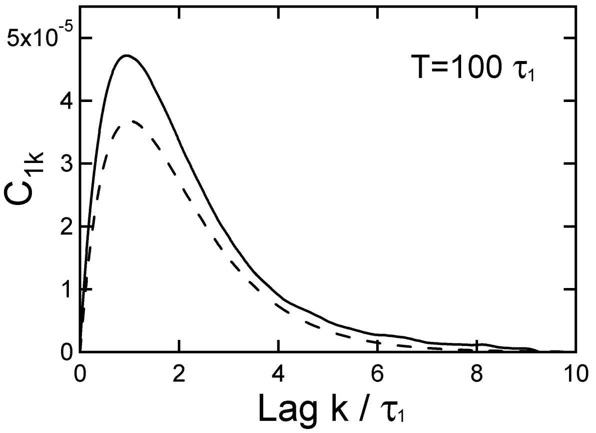

Figure 3.7: The covariance function C_{1k} of $\hat{\rho} - \rho$ plotted as a function of lag k/τ_1. The solid line is the simulation result obtained from averaging 5×10^3 different trajectories ($\ell = 1$, $\tau_1 = 200$, length 10^7), and the dash line is the prediction of Bartletts formula. Note that the deviation from Bartletts formula is on the opposite side as in Fig. 3.4, because the signs cancel when calculating the products in C_{1k}.

Again, we can rewrite Eq. (3.14) in a normalized scheme by replacing $T = \bar{T}\tau_\ell$, $i = \bar{i}\tau_\ell$, and $j = \bar{j}\tau_\ell$:

$$C_{ij}=\frac{e^{-\bar{j}}}{\bar{T}\tau_\ell}\left\{e^{\bar{i}}\left[(\bar{j}-\bar{i})\tau_\ell+\frac{1}{e^{2/\tau_\ell}-1}\right]-e^{-\bar{i}}\left[(\bar{j}+\bar{i})\tau_\ell+\frac{e^{2/\tau_\ell}+1-e^{2\bar{i}}e^{2/\tau_\ell}}{e^{2/\tau_\ell}-1}\right]\right\}. \tag{3.16}$$

For $\tau_\ell \gg 2$, $\exp(2/\tau_\ell) \approx 1 + 2/\tau_\ell$. The large τ_ℓ approximation of Eq. (3.16) can be written as

$$C_{ij}\approx\frac{e^{-\bar{j}}}{\bar{T}}\left\{e^{\bar{i}}\left(\bar{j}-\bar{i}+\frac{1}{2}\right)-e^{-\bar{i}}\left(\bar{j}+\bar{i}+1-\frac{e^{2\bar{i}}}{2}\right)\right\}. \tag{3.17}$$

Note that Eq. (3.17) is independent of τ_ℓ. Therefore, not only the correlation function itself but also the variance and covariance of the correlation deviations can be rescaled in the standard forms: Eq(3.10) and (3.17). Figure 3.7 plots $C_{1,j}$ as a function of lag k/τ_1 for the simulated data set and as calculated using Eq. (3.15). The simulated result is close to the theoretical prediction in spite of the positive deviation which is again the consequence of zero filling effect. The positive covariance values in Fig. 3.7 indicate that the deviation from the true correlation function tends to maintain its sign for a period of time, instead of randomly jumping around the true values. Thus the shapes of the correlation functions change and lead to a broad distributions in $\{\tau_F\}$ and $\{\beta_F\}$. Most importantly, the agreement between the variance/covariance derived from Bartlett's formula and the rotational simulation indicated that the distributions of $\{\tau_F\}$ and $\{\beta_F\}$ are a general result for any process with an exponential correlation function.

Many researches use the distribution of $\{\tau_F\}$ and $\{\beta_F\}$ as an indication of environment heterogeneity. [69, 83] From the discussion above, it is clear that even for the homogeneous case (i.e., $\beta_\ell = 1$), there are always distributions in $\{\tau_F\}$ or $\{\beta_F\}$. Therefore, the question one should ask is not whether the distributions exist but instead check if the distributions obtained from an experiment are significantly larger than the "inherent width". Since the average and standard deviation of the distribution at different Ts are provided in Fig. 3.6, it is convenient to compare to the experimental distributions by means of statistical test (F test, for instance [84]). We should note that τ_ℓ and T are the key parameters for further analysis. In different measurements, T might not have the same value. But the distribution can only be built from trajectories of the same size, and truncations are sometimes needed. As for τ_ℓ, it can be estimated by averaging $\{\tau_F\}$; however, if there are not enough trajectories, the error of the estimation will be huge. Also, since short trajectories yield an average τ_ℓ that systematically deviates from the true τ_ℓ, it can be challenging to know the length of the trajectory relative to the true correlation time.

3.4.3 Correlation function analysis for higher rank spherical harmonics

From the discussion above, it is clear that any analysis based on $T < 50\tau_\ell$ will be extremely difficult. One way to improve the quality of correlation analysis is to get trajectories as long as possible; however, in the fluorescent probe measurement, many factors such as photobleaching, focus drifting, and apparatus instability will limit the length of the observation time. At the start of Section 3.4.1, we noted that the discussion would be based on $\ell = 1$, but there is no reason to analyze and compare only one of the components. In theory, rotational diffusion in a homogeneous matrix can be expressed in terms of spherical harmonics [Eq. (3.6)]. Each of the components has a single exponential correlation function with $\tau_\ell[\ell(\ell+1)D_{rot}]^{-1}$. Since $\tau_\ell \propto [\ell(\ell+1)]^{-1}$, the value of τ_ℓ will be small for large ℓ. Thus the requirement of large T/τ_ℓ is satisfied when we analyze the data based on higher order spherical harmonics. Figures 3.8(a), 3.8(b) show the average and standard deviation of $\{\tau_F\}$ and $\{\beta_F\}$ calculated for $\ell = 1$, 4, and 8 at different T. Under the normalized scale, all the curves approximately fall into a standard form. Since τ_ℓ is smaller for larger ℓ (for example, $\tau_8 = \tau_1/36$), the curves for larger ℓ will cover a T/τ_ℓ region where the standard errors are relatively smaller. Closer inspection

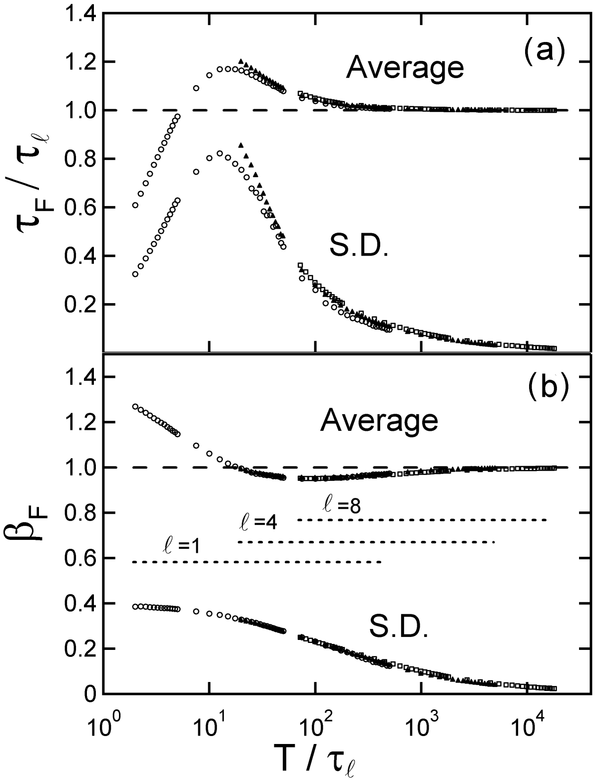

Figure 3.8: The average and standard deviation of (a) τ_F/τ_ℓ and (b) β_F plotted as a function of T/τ_ℓ. The points $\ell = 1$ (open circles), $\ell = 4$ (filled triangles), and $\ell = 8$ (open squares) are calculated from a long trajectory ($\tau_1 = 200$, length 10^6 broken into pieces of desired size T, and the resulting values are the average of 100 different long trajectories.

reveals that the curves for $\ell > 1$ gradually deviate from the $\ell = 1$ curve. The deviation is more significant in τ_F than in β_F, and the difference increases as T/τ_ℓ gets smaller. If we repeat the calculation for another trajectory whose τ_1 is set to be exactly the same as τ_8 in Fig. 3.8, the resulting curve matches the $\ell = 1$ curve and not the $\ell = 8$. This implies that the discrepancy in Fig. 3.8 is inherent to the simulated trajectory. We attribute this inconsistency to the error introduced from flat-plane approximation, which alters the probability distribution from the free diffusion. The effect becomes more significant when examining the correlation functions of higher order spherical harmonics that are sensitive to small angle changes.

It seems that one can gain advantages by using higher order spherical harmonics to calculate the correlation function. However, from the theoretical and practical points of view, there must be a compromise, and one should be cautious when interpreting the results. First, Eq. (3.7) ensures that all the correlation functions have an exponential form if the dynamics are given by homogeneous rotational diffusion. Mathematically, all the spherical harmonic terms need to be checked in order to identify the model of dynamics under study. If the $\ell = 1$ trajectory yields a single exponential correlation function, it does not guarantee that other terms will be the same. Since rigorous proof of model matching based on limited data is seldom available, comparing only one or two terms is a more realistic approximation. A major question arises: How large an ℓ value can be calculated? The obvious restriction arises from the fitting. Because it is almost impossible to fit the curve with decay constant less than unity, once the unit of time is set, the highest ℓ is also determined. It seems that the difficulty of fitting insufficient points can be overcome by increasing the resolution of measurement, i.e., to increase the point density of trajectory. However, as we have discussed above, the crucial factor which decides how many points we can measure is the durability of fluorescence probes. If we increase the frequency of illumination, the dye molecules will be more prone to photobleaching. Another important reason that restricts the usage of higher ℓ correlation calculation is the sensitivity to noise. Since the higher order spherical harmonic terms account for the fast changing phenomena, they are very sensitive to the small difference in the trajectories. As seen in Fig. 3.8, the curves for larger ℓ deviate from the standard curve, which reflects the slight difference between the homogeneous rotational diffusion and the flat-plane approximation. In real measurements, the quality of data will be reduced by the noise and affect the performance of higher order calculations. Despite these limitation, examination of the correlation functions for larger ℓ should be a useful means to increase the effective trajectory length T/τ_ℓ. The ratio of τ with respect to two different ℓs can be useful when comparing different models of rotational motion. [77, 79, 85] Diffusive rotation, for example, exhibits the characteristic relation between two different τ_ℓ's, i.e., $R_{\ell,\ell'} \equiv \tau_\ell/\tau_{\ell'} = [\ell'(\ell'+1)]/[\ell(\ell+1)]$. Other models, however, show different behaviors. [85] For example, when the large scale jumps are involved in the molecular rotation, the ratio will change (e.g., $R_{2,1} \to 1$ instead of $1/3$). [86] Therefore, the deviation from the prediction might imply the inconsistence in the model of dynamics. Obviously, the finite sample effect plays an important role in the sample distributions of $R_{\ell,\ell'}$. As discussed above, we know that the distribution of $\{\tau_F\}$ is broader for a smaller ℓ. Hence, it can be anticipated that the distribution of ratios including τ_1 will be strongly influenced by the size of T. Figure 3.9 shows the averages and standard deviations of $R_{2,1}$, $R_{4,1}$, and $R_{8,1}$. Each curve is rescaled by its theoretical ratio ($R_{2,1} = 1/3$, $R_{4,1} = 1/10$,

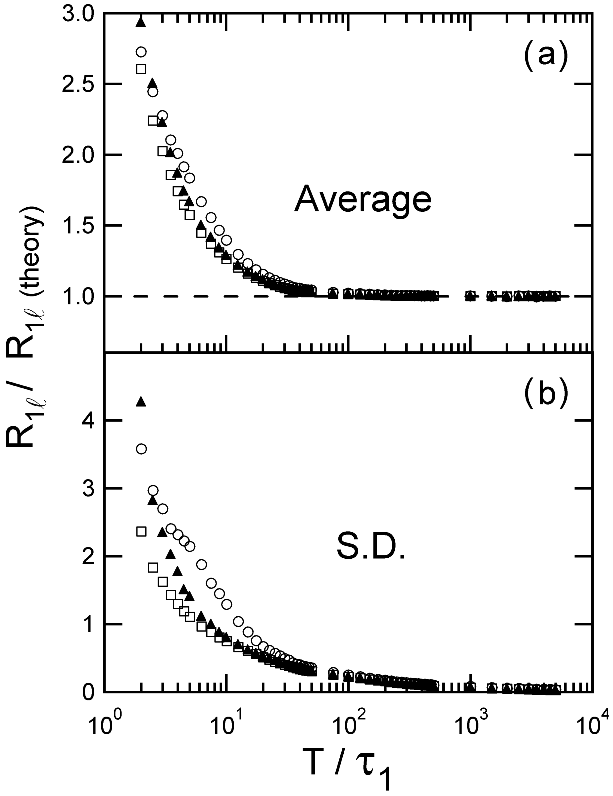

Figure 3.9: The averages (open symbols) and standard deviations (filled symbols) of ratios $R_{2,1}$ (circles), $R_{4,1}$ (triangles), and $R_{8,1}$ (squares) at different $T/\tau 1$. In order to make a comparison, all the curves are divided by their theoretical ratios $R_{2,1} = 1/3$, $R_{4,1} = 1/10$, and $R_{8,1} = 1/36$, so the common asymptote will be 1. Each point is calculated from a long trajectory ($\tau_1 = 200$, length 10^7) broken into pieces of desired size T, and the resulting values are the average of 20 different long trajectories.

and $R_{8,1} = 1/36$). From the figure, we can see that all average curves approach to 1 when $T > 50\tau_1$ and that the averages become larger as T gets smaller in the region $T < 50\tau_1$. The standard deviation (S.D.) curves have the same trend, and it is not surprising that when T decreases further from $50\tau_1$ the

S.D. curve of $R_{2,1}$ rises earlier than the other two, which can be attributed to the relatively broader distributions in both $\{\tau_F\}_{\ell=1}$ and $\{\tau_F\}_{\ell=2}$. However, in the region $T < 10\tau_1$ the zero filling effect starts to suppress $\{\tau_F\}_{\ell=2}$, and thus one can see in Fig. 3.9 that the $R_{2,1}$ curves are even lower than $R_{4,1}$ curves at small T. It is clear that even for $T = 50\tau_1$, the relative S.D. is about 30% of the average value. The result indicates that care must be taken when we choose the ratio as a measure of characterization. Again, it is not a fixed number; instead, one needs to show whether the experimental result is statistically different from the simulated value.

3.4.4 Covariance versus correlation function analysis

Lastly, one would often like to compare an average single molecule result with an ensemble averaged value. The deviations of the average of sample correlation functions from the true correlation function complicate this problem. As discussed previously, the correlation estimator Eq. (3.3) is biased, and hence the correlation function will be underestimated for $k > 0$. This has no effect on comparison of experimental values with simulation, since the trajectories are treated with the same correlation function analysis. However, if the time constant is a factor whose exact value is used for further analysis or interpretation, then the accuracy of this value is very important. Another means of measuring the correlation time constant is by utilizing the covariance function instead of the correlation function. By definition the two functions only differ by a factor $\gamma(0)$ and the decay constants are the same. By fitting the sample covariance functions with a stretched exponential (preexponential factor undetermined), one can expect to obtain the same result. One problem is that the common covariance estimator, Eq. (3.11), is biased. Therefore, it would be better to utilize a different covariance estimator that will give an unbiased estimation of the covariance function: [74]

$$\hat{\Gamma}'(k) = \frac{1}{T-k}\sum_{t=1}^{T-k}(X_t - \bar{X})(X_{t+k} - \bar{X}). \tag{3.18}$$

In theory, the estimates of the sample covariances, $\hat{\gamma}'(k)$, obtained from Eq. (3.18) are unbiased, i.e., $E[\hat{\gamma}'(k)] = \gamma(k)$. Hence, by fitting the average of sample covariance functions calculated from Eq. (3.18), one obtains a better estimation of time constant than the value from the averaged sample correlation functions. The reason one should not fit the curves first and then average the resulting time constants is that the mean of $\{\tau_F\}$ is not the theoretical value as shown in Fig. 3.6. Since we force the curves to be fitted by stretched exponentials, there will be some complex interrelations among the undetermined parameters which account for the trends of deviations in the distributions.

3.5 Conclusions

We have numerically simulated rotational diffusion in a homogeneous environment, and the properties of finite size trajectories have been studied. For a trajectory of whose length is less than 100 times the correlation time ($T/\tau_\ell < 100$), the deviation from the true correlation function is significant.

For an ensemble of trajectories of a given length, fits of sample correlation functions yield distribution of $\{\tau_F\}$ and $\{\beta_F\}$ rather than fixed values. These distributions broaden and become asymmetric as T/τ_ℓ gets smaller. As a consequence, dynamical heterogeneity should be invoked only when measured distributions are shown to be significantly different from the simulated results by means of statistical criterion such as the F test. In theory, it is necessary to examine all the correlation functions of different ℓs for the purpose of identification of a rotational model. However, if one assumes the rotational model to be diffusion, all RCFs yield equivalent information. This allows for the analysis of the RCF for higher order spherical harmonics. Since correlation functions with larger ℓ decay faster, the distributions of $\{\tau_F\}$ and $\{\beta_F\}$ are relatively narrower. Thus, the data size required for the analysis based on the higher order spherical harmonics will be smaller, and it will be easier to map $\{\tau_F\}$ and $\{\beta_F\}$ distributions from limited experimental data. An ideal practice would be to analyze the highest possible ℓ that maximized trajectory length while maintaining sufficient signal to noise to fit the correlation function decay. A comparison of the decay constants for two ℓ values should be utilized to validate that the dynamics are diffusive. The ability to calculate higher order RCFs from trajectories of the polar and azimuthal angles provides an advantage for methods that measure the full 3D orientation over techniques that measure only one spherical harmonic component.

Finally, while some of the results presented are specific to rotational correlation functions, many have implications in general for correlation analysis of single molecule trajectories. As the advantage of single molecule experiments is the ability to measure distributions of properties rather than ensemble averaged values, it is critical to understand the inherent distributions that will be observed as a result of the analysis. Given that a great deal of single molecule data is limited by photochemistry which shortens observation time, it follows that finite trajectory length will be a critical issue for any correlation analysis. In general, the average values and distributions presented in Fig. 3.6 should hold for any dynamic process whose correlation function is a single exponential. Ideally, comparison should be made directly with distributions obtained from simulation of the appropriate kinetic or dynamic model.

Chapter 4

Analysis of orientational dynamics of single fluorophore trajectories from three-angle polarization experiments

4.1 Abstract

An algorithm of single fluorophore orientation reconstruction based on a recently proposed method [J. T. Fourkas, Opt. Lett. 26, 211 (2001)] is studied, which converts three measured intensities $\{I_0, I_{45}, I_{90}\}$ to the dipole orientation $\{I_T, \theta, \phi\}$. Fluctuations in the detected signals $\{\delta I_0, \delta I_{45}, \delta I_{90}\}$ caused by the shot noise results in different profiles in $\delta\theta$ and $\delta\phi$, causing the originally equivalent coordinates (X, Y, Z) to separate into in-plane (X, Y) and out-of-plane (Z) components. The overall fluctuation in $\delta\theta$ turns out to be higher than $\delta\phi$, and thus noise has a greater effect on the Z component of the signal than on the X and Y components. Therefore, care should be taken not to interpret differences in the in-plane and out-of-plane dynamics as being evidence of nonisotropic rotational motion. For some molecular orientations around $\Theta = \pi/2$, the total signal intensity cannot be inverted directly to angular coordinates. An optimization method is proposed that calculates the corrected angular coordinates for the points in the trajectory. To test the effects of this recovery scheme, the covariance/correlation functions for recon-

structed angular trajectories were calculated for the case of isotropic rotational diffusion. Rotational correlation functions of rank ℓ were found to deviate from the ideal single exponential decay as a result of the noise. This effect becomes more significant for large ℓ cases. The correlation functions were fitted to a stretch exponential to characterize their deviation from the true single exponential decay. Correlation functions of Z have larger deviations from the true correlation function due to the larger noise in the Z component. The trends and the distributions of stretched exponential parameters $\{\tau_F\}$ and $\{\beta_F\}$ fitted from trajectories of a given size T also exhibit the influences from noise. Again, large ℓ cases show a greater effect from the noise which eliminates the benefit of calculating higher rank correlation functions because of the smaller time constants. Due to the errors in estimating the correlation functions, significant differences between correlation functions of different orders can result from the statistics rather than being an indication of a nondiffusive behavior.

4.2 Introduction

The rotational dynamics of single molecules provides useful information about the local environment, such as rheological properties, spatial geometry, and the interaction with the surrounding molecules. The techniques developed for detecting molecular orientations have been applied in many materials and biological systems. [67, 87, 88, 65, 69, 89, 90, 91, 92] An easy method to acquire orientation information with polarization spectroscopy of single fluorescent molecules, which relates the intensity profile and the polarization distribution of the collected fluorescence radiation to the emitting source orientation. [93, 94] In practice, many detection schemes have been proposed, and each has its own design for measuring the polarization with the collected fluorescence. Two types of measurements are widely used: wide-field [95, 96, 68, 97]/scanning [98, 70] imaging and confocal microscopy. [66, 99] The imaging methods are capable of monitoring several molecules simultaneously and thus are popular for studying biological systems. More intense illumination is required to achieve high image quality and time-consuming data processing limits these applications for studying long-time dynamics, which is always restricted by the short durability of probed molecules. Instead of spreading out the signals, the confocal scheme restricts the measurement to 1 pixel/detector, and thus the collected photons can be concentrated in only a few polarization channels. Recently, a rapid orientation reconstruction method based on three-angle polarization measurements was proposed by Fourkas. [66] In theory, with the total emission rate left unknown, the intensities from three different polarizations are sufficient to solve the dipole orientation in spite of the symmetry issue that creates degeneracy in the reconstruction. The formulas are derived under the conditions of a high numerical aperture (N.A.) and infinite-corrected polarization-preserving objective, both of which can be implemented in a confocal scheme. Since only three channels are required, it becomes a more economical choice for studying long-time dynamics when compared with other single molecule imaging methods. In this paper, more detailed properties of the Fourkas formulation are explored, and an algorithm for angular trajectory reconstruction is proposed. In order to demonstrate the capability of extracting dynamic information, rotational diffusion is used as a model to examine numerically simulated intensity trajectories. In the previous chapter, we have examined the finite size effect of the pure rotational diffusion correlation functions. [21] In particular, one discovers that limited observation time leads to significant errors in both the decay constant and shape of the estimated correlation function. Ideally, transients would be collected for thousands of times longer than the decay constant. One way to increase the effective length of the transients is to study higher order spherical harmonic components because of their relatively faster decay constants. For example, if one could calculate $\ell = 8$ instead of $\ell = 2$, the transient would be effectively 12 times longer since τ_8 is 12 times shorter than τ_2. To generate spherical harmonics of any order requires full orientation information. The three-angle polarization experiment is a practical choice to calculate the single molecule orientations. To examine the effect of noise, single molecule transients of isotropic diffusion are simulated. The resulting three-detector signals are calculated and shot noise is introduced. Then, the angular trajectories are calculated to understand how noise can affect the reconstructed orientations as well as the shapes and the distributions of the correlation functions. For isotropic diffusion, one would expect the in-plane and out-of-plane dynamics to be identical. One would also expect that correlation functions of any rank spherical harmonic could be normalized to the same diffusion time. It will be shown that the shot noise causes significant differences in both of these signatures of diffusive behavior.

4.3 Theory and analysis methods

In the following discussion, calculations are based on the theory of three-dimensional (3D) orientation reconstruction proposed by Fourkas. [66] The model will be extended by considering the effect of detection limitations, such as detector efficiencies and noise. In order to examine the capability of extracting dynamics from a rotating system, numerical simulations of isotropic rotational diffusion are used as an example model. Having the full orientational information allows for the calculation of higher order rotational correlation functions as well as comparison of in-plane and out-of-plane dynamics. The calculations with the three-detector method are compared with a relatively simpler two-detector scheme which can only monitor a single rank of the rotational correlation function. [94, 63, 64]

4.3.1 Angular distribution of dipole radiation and orientation reconstruction

Consider the case where an emitting dipole is at the focal point. When the fluorescence is collected by an infinite-corrected and polarization-preserving objective, the dipole orientation $\Omega(\Theta, \Phi)$ and the system geometry can be defined as in Fig. 4.1(a). The maximum of the collecting angle (α) is determined by the objectives numerical aperture N.A. and the refractive index (n) of the medium: $\alpha = \sin^{-1}(\mathrm{N.A.}/n)$. (The values N.A. $= 1.35$, $n = 1.518$ are used in

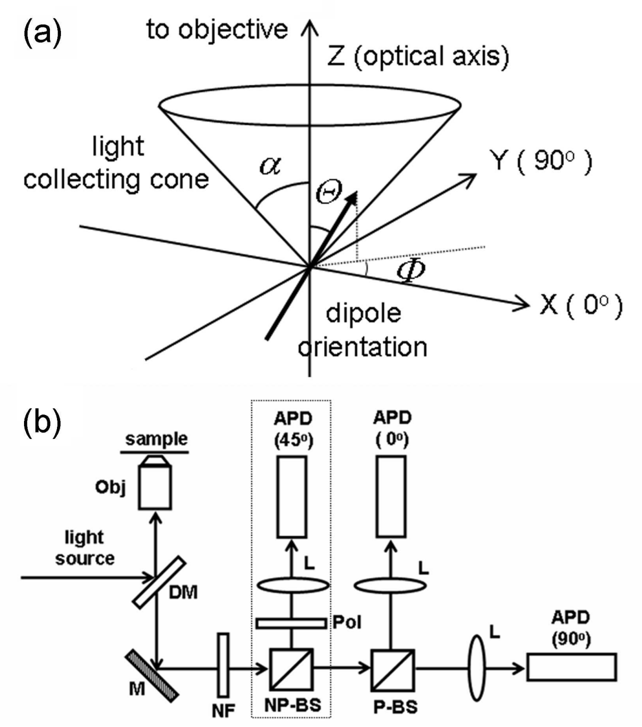

Figure 4.1: (a) Geometry defined for a radiating dipole with orientation $\{\Theta, \Phi\}$. (b) Example of three-angle polarization experiment setup with epifluorescence confocal scheme. The excitation light and the fluorescence collected by an objective (Obj) are separated by a dichroic mirror (DM). The fluorescence then passes through a mirror (M), and a notch filter (NF) and is then consecutively split by a nonpolarizing (NP-BS) and a polarizing beamsplitter (P-BS). The linear polarizer (Pol) is set at 45^o. Each beam is finally focused by a lens (L) onto the APD detector.

this paper.) We assume that the medium is uniform and the refractive index difference between the medium and the objective can be neglected. Only the objective can affect the propagation of light emitted from the dipole. With the above assumptions, the intensities (I_i, $i = 0$, 45, 90) collected in three different polarizations of 0^o, 45^o, and 90^o have been shown to have the following forms:

[66]

$$\begin{aligned} I_0(\Theta,\Phi) &= I_{tot}(A + B\sin^2\Theta + C\sin^2\Theta\cos 2\Phi), \\ I_{45}(\Theta,\Phi) &= I_{tot}(A + B\sin^2\Theta + C\sin^2\Theta\sin 2\Phi), \\ I_{90}(\Theta,\Phi) &= I_{tot}(A + B\sin^2\Theta - C\sin^2\Theta\cos 2\Phi), \end{aligned} \tag{4.1}$$

where

$$A = \tfrac{1}{6} - \tfrac{1}{4}\cos\alpha + \tfrac{1}{12}\cos^3\alpha,$$

$$B = \tfrac{1}{8}\cos\alpha - \tfrac{1}{8}\cos^3\alpha,$$

$$C = \tfrac{7}{48} - \tfrac{1}{16}\cos\alpha - \tfrac{1}{16}\cos^2\alpha - \tfrac{1}{48}\cos^3\alpha.$$

It is obvious that the dipole orientations Θ and Φ as well as the total intensity I_{tot} emitted during the period of measurement can be obtained by solving the above three equations. We denote $\{I_T, \theta, \phi\}$ to be the corresponding reconstructed values of $\{I_{tot}, \Theta, \Phi\}$,

$$I_T = \frac{G-B}{2AC}\sqrt{2(I_0 - I_{45})^2 + 2(I_{90} - I_{45})^2}, \tag{4.2}$$

$$\theta = \sin^{-1}\sqrt{\frac{A}{G-B}}, \tag{4.3}$$

$$\phi = \frac{1}{2}\tan^{-1}\left(\frac{2I_{45} - I_0 - I_{90}}{I_0 - I_{90}}\right), \tag{4.4}$$

where

$$G = \frac{C(I_0 + I_{90})}{\sqrt{2(I_0 - I_{45})^2 + 2(I_{90} - I_{45})^2}}.$$

We should note that the solution itself is not unique because of the periodicity of trigonometric functions: $\sin^2\Theta = \sin^2(\pi - \Theta)$ and $\sin, \cos(2\Phi) =$

$\sin, \cos[2(\Phi + \pi)]$. Thus, the total symmetry of the orientation mapped from three detectors will be fourfold. If one would like to determine angles in a trajectory, it is reasonable to choose the least-rotation point from the four equivalent images as long as the dynamics are smooth and without large jumps. Another similar problem will also occur when the trajectory crosses the equator ($\Theta = \pi/2$). The least-rotation method always selects the "reflected" point rather than the point on the other side of the equator. As a result, the trajectory will be trapped in one hemisphere. To avoid this situation, the least-rotation algorithm is modified by introducing a random process. That is, once two or more images have great-circle distances to the previous point that are less than some criterion (0.5 was chosen for a unit sphere), the procedure randomly assigns the new orientation to one of those images. A more accurate method is to assign a probability to points weighted according to their distances. However, in the following examples, the difference is small and can be ignored. In practice, one can utilize polarizing optics to separate the collected fluorescence into three polarizations. For example, in Fig. 4.1(b) a polarizing beamsplitter, together with a linear polarizer set at 45^{o}, is used in the setup to extract I_0, I_{45}, and I_{90}. In typical fluorescence polarization spectroscopy, only the two orthogonal polarizations $\{I_0, I_{90}\}$ are monitored. The cost of introducing the third detector is that the measured intensity will be further reduced by a half when compared with the two-detector scheme. The benefit is that the three-detector method provides full orientation information. We should note that since light has been split, the intensity readings of the detectors as well as the calculated I_T are actually one-fourth of the original value in the three-detector system and one-half in the two-detector scheme. To prevent confusion, in the following calculations we report I_{tot} as the intensity level "after" splitting. Also, since the intensity of three-detector setup is half of that in the two-detector scheme, we will include this factor in the simulations to make fair comparisons between the two methods.

4.3.2 Rotational diffusion and correlation function analysis

The rotation of fluorescent molecules embedded in a homogeneous condensed phase can be approximately described by the diffusion model.[77, 79, 78] Since molecular motion is a stochastic process, it is useful to use correlation functions to study the probability structure of the underlying dynamics. It can be shown that under the stationary condition, the correlation function of the angular trajectory has the following single exponential form:[80]

$$\begin{aligned} \rho_{\ell',m',\ell,m}(k) &= \frac{\langle Y_{\ell'}^{m'}(\Omega)|K(\Omega,\Omega_0;k)|Y_\ell^m(\Omega_0)\rangle_{\Omega,\Omega_0}}{\langle Y_{\ell'}^{m'}(\Omega)|K(\Omega,\Omega_0;0)|Y_\ell^m(\Omega_0)\rangle_{\Omega,\Omega_0}} \\ &= e^{-\ell(\ell+1)D_{rot}k}\delta_{\ell,\ell'}\delta_{m,m'}, \end{aligned} \tag{4.5}$$

where

$$K(\Omega,\Omega_0;t) = \sum_{\ell,m} Y_\ell^{m*}(\Omega)Y_\ell^m(\Omega_0)e^{-\ell(\ell+1)D_{rot}t}$$

is the probability propagator.

In the above equation, the rotational motion is expressed in terms of its spherical harmonic components with the rank ℓ. The decay time constant for each order of correlation function is defined as $\tau_\ell \equiv [\ell(\ell+1)D_{rot}]^{-1}$, where

D_{rot} is the so-called rotational diffusion constant. Since the system is assumed to be stationary, the form is independent of the point chosen where $t = 0$. For pure rotational diffusion, the ratio of decay time constants obtained from the correlation functions of order ℓ and ℓ' strictly follow $\tau_\ell / \tau_{\ell'} = [\ell'(\ell'+1)]/[\ell(\ell+1)]$. It is often used as a signature to identify a diffusive type of rotation.

With an angular trajectory $\{X(\Omega_t), t = 0, 1, 2, \cdots, T-1\}$ of finite size T, the true correlation function can only be estimated. In theory, if full orientational information is available, all spherical harmonics can be obtained from the orientation trajectory $\{\Omega_t\}$ and the correlation functions exhibit a single exponential decay, described by Eq. (4.5). However, in many experimental cases only two orthogonal polarizations, I_0 and I_{90}, are measured to determine the reduced linear dichroism. It can be shown that with a high N.A. value, the correlation function for the dichroism is dominated by the first term, namely, the $\ell = 2$ term, which gives $\tau = \tau_2 = (6D_{rot})^{-1}$. [64] We should note that reduced linear dichroism is a function of both Θ and Φ. Thus, this measurement is not mathematically sufficient to generate spherical harmonic trajectories of arbitrary orders. It is possible to use two nonorthogonal polarizations to extract higher order signals. [100] However, this is not an efficient method compared with 3D orientation reconstruction if two or more orders need to be monitored simultaneously. The method of generating rotational diffusion trajectories for a given diffusion coefficient has been described previously. [21] Briefly, rotational diffusion in a homogeneous environment can be simulated by a random walk on the surface of a unit sphere. The flat-plane approximation [21] is used to generate a small displacement on the curved surface. The resulting coordinates (Θ, Φ) of each step are used to calculate the intensity transients for the three detectors using Eq. (4.1).

Considering the finite size of the trajectories and the effect of noise, the correlation functions for these trajectories will no longer be single exponential. In order to characterize the effect, the stretched exponential function $\xi_F \exp[-(t/\tau_F)^{\beta_F}]$ is used to fit the correlation functions calculated from the sample trajectories. Three parameters, ξ_F, β_F and τ_F, are obtained in the fitting process. The effect of noise, together with the finite sampling on the distributions of the decay time constants (τ_F) and the stretching exponents (β_F), will be explored.

4.3.3 Detection limitations and noise

By looking at Eqs. (4.2)(4.3)(4.4), one uses $\{I_0, I_{45}, I_{90}\}$ to calculate $\{I_T, \theta, \phi\}$. Since the total intensity I_T is treated as an unknown, its value is independent of θ and ϕ. The benefit of this formulation is that the exact I_T does not need to be known a priori, and fluctuations in the emission rate will affect I_T but not θ and ϕ. Only the ratios I_i/I_j $(i \neq j)$ are important, and therefore, the remaining problem is how to balance the detectors. Because the optical efficiency varies in different polarization channels, one needs to know the correction factors to make sure that the corrected intensity ratios between any two of the detectors reflect the exact values. This is an important experimental consideration but is trivial in the simulation where the three channels are assumed to have exactly the same efficiency.

Most importantly, all measurements contain noise. The issue of noise becomes critical when the signals are weak. Because of the quantized nature of photons, the arrival times follow Poisson statistics and thus exhibit fluctuations, which are usually referred to as "shot noise". [101, 102] Unlike instrumental noise, shot noise is unavoidable. The relative photon number fluctuation $\delta N/N$ within a given time interval is inversely proportional to $\sqrt{N}$. Thus, the only way to reduce the effect of shot noise is by increasing the number of collected photons. This is not always practical in reality. In the calculation, shot noise is chosen as the only source of noise. In practice, other experimental sources of noise could make the fluctuations even larger. In particular, all single molecule experiments will have a background which cannot be explicitly subtracted form the data. Because the background can vary greatly in single molecule experiments, the simulations were chosen to be background free. This represents an idealized shot-noise limited scenario. Real experiments will suffer even larger errors in converting the three-detector intensity into angular coordinates from the less than perfect balance between the channels and the finite background in the signals. To compare the simulations with experiments, intensity levels of $I_{tot} = 2000$ and 4000 were chosen for the three- and two-detector methods, respectively, which yield reasonable ranges of simulated $\{I_0, I_{45}, I_{90}\}$. The noise-free trajectories $\{I_0, I_{45}, I_{90}\}$ are calculated from Eq. (4.1), and the shot noise is introduced by adding normally distributed random variables with a mean $\mu = \{0, 0, 0\}$ and a variance

$\sigma^2 = \{I_0, I_{45}, I_{90}\}$. Each number is then truncated to the nearest integer which is less or equal to the original value. Rarely, the rounded results are negative and those points are set equal to zero.

4.4 Results and discussion

4.4.1 Orientation reconstruction from noisy trajectories

Without noise, the intensities $\{I_0, I_{45}, I_{90}\}$ can be exactly inverted to $\{I_T, \theta, \phi\}$ by using Eqs. (4.2)(4.3)(4.4). However, when noise is added to the signals, not all intensity combinations are invertable. Equation (4.3) can be rewritten to

$$\sin^2\theta = \frac{A}{G - B} \equiv p(I_0, I_{45}, I_{90}). \tag{4.6}$$

By definition, the polar angle $\Theta \in [0, \pi]$, and thus $\sin^2\Theta \in [0, 1]$. The value $A/(G - B)$ calculated from $\{I_0, I_{45}, I_{90}\}$ with the noise is, in general, a real number and is not strictly in the range of $[0, 1]$. This will cause a problem when trying to calculate θ by taking the square root and/or inverting the sine function. Without noise, the parameter G is a function only of Θ, and its value decreases monotonically from $\Theta = 0$ until it reaches the minimum $G = A + B$ at $\Theta = \pi/2$. If $G < A+B$, p starts falling out of the range $[0, 1]$. This situation happens only when noise is included and Θ is very close to $\pi/2$, which makes $G < (A+B)$ possible and implies that the uninvertable points are mostly from $\Theta \approx \pi/2$. To circumvent this problem, $p\{I_0, I_{45}, I_{90}\}$ is used to identify those problematic points, and the solution for the rest of the trajectory is obtained

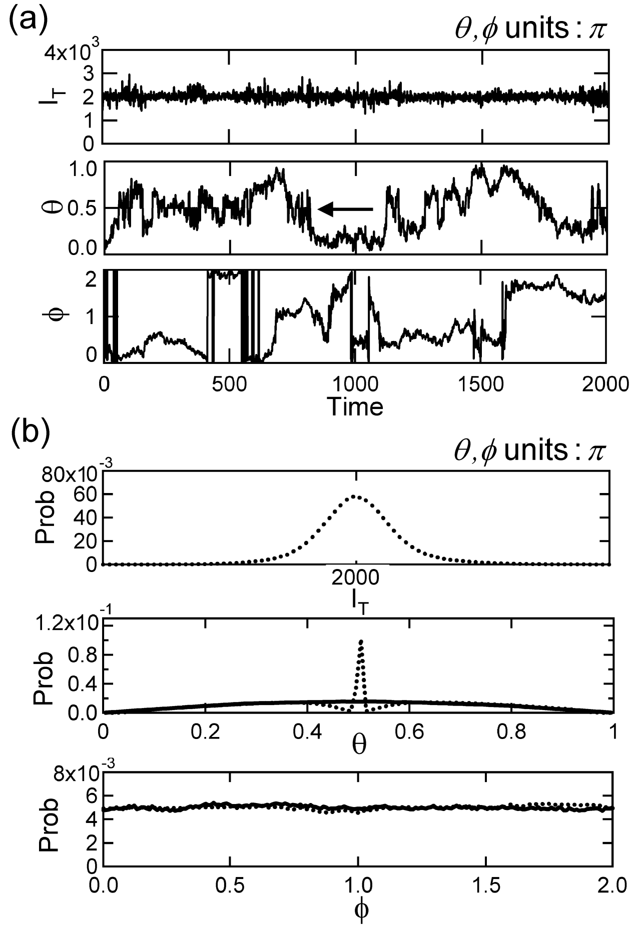

Figure 4.2: Example of the simulated pure rotational diffusion data of $\tau_1 = 200$ and size 10^6. The shot noise is added based on $I_{tot} = 2 \times 10^3$ level. (a) Trajectories $\{I_T\}$, $\{\theta\}$, and $\{\phi\}$ are reconstructed from the first 2×10^3 points. The arrow shown in $\{\theta\}$ indicates where the trajectory has been flattened. (b) Histograms obtained from the whole trajectory. The dotted lines represent the reconstructed results in which the noise is considered. The solid lines are from the corresponding noise-free data. The noise-free $\{I_T\}$ histogram is a delta function peaked at $I_T = 2 \times 10^3$, which is not shown in the figure.

with Eqs. (4.2)(4.3)(4.4). For the uninvertable data, an optimization method

[82] is used to find $\{I_T, \theta, \phi\}$, which minimizes the following equation:

$$f(I_T, \theta, \phi) = (\tilde{I}_0 - \hat{I}_0)^2 + (\tilde{I}_{45} - \hat{I}_{45})^2 + (\tilde{I}_{90} - \hat{I}_{90})^2, \tag{4.7}$$

where $\hat{I}$s are the measured data, and

$$\begin{aligned} \tilde{I}_0 &= I_T(A + B\sin^2\theta + C\sin^2\theta\cos 2\phi), \\ \tilde{I}_{45} &= I_T(A + B\sin^2\theta + C\sin^2\theta\sin 2\phi), \\ \tilde{I}_{90} &= I_T(A + B\sin^2\theta - C\sin^2\theta\cos 2\phi). \end{aligned} \tag{4.8}$$

This algorithm is included in the procedure to recover the “bad data”. Once the whole trajectory is converted to $\{I_T, \theta, \phi\}$, the least-rotation algorithm is used to arrange the points in a smooth trajectory. Figure 4.2 shows such a diffusion trajectory of size 10^6 and $\tau_1 = 200$ and the corresponding histograms of $\{I_T, \theta, \phi\}$ for both the noise-free and shot-noise limits. As a result of the noise, $\{I_T\}$ is no longer constant and there is a distribution around the true value. As for the orientation, $\{\phi\}$ has approximately the same distribution as $\{\Phi\}$, which is a uniform distribution over $[0, 2\pi]$. However, the distribution of $\{\theta\}$ is strongly affected by the presence of the outlier points. Since the optimization method usually selects $\theta \approx \pi/2$ for those points, the θ trajectory appears “flattened” in the time periods where there are many outlier data points. As a result, the distribution $\{\theta\}$ shows a peak at $\theta = \pi/2$.

It is clear that with noise, the calculated orientations will deviate from the true values. The extent of the error in estimating the orientation depends on both the intensity fluctuations of each detector (denoted by δI) and the orientation itself. When the intensity level is high, the Poisson distribution can be approximately represented by a normal distribution with the same mean and variance. Then, the detector signal can be seen as Gaussian noise added onto the noise-free signal. Assuming that the noise is small and is independent from detector to detector, the errors $\{\delta I_T, \delta\theta, \delta\phi\}$ that propagate from $\{\delta I_0, \delta I_{45}, \delta I_{90}\}$ are, to the first order, calculated by Eq. (4.9) [103]

$$(\delta W)^2 = (\delta I_0 \partial_{I_0} W)^2 + (\delta I_{45} \partial_{I_{45}} W)^2 + (\delta I_{90} \partial_{I_{90}} W)^2, \tag{4.9}$$

where $W \equiv \{I_T, \theta, \phi\}$, and $\delta I = \sqrt{I}$ is chosen for the shot noise. By plugging Eqs. (4.2)(4.3)(4.4) into Eq. (4.9) and using the relation from Eq. (4.1), the surface plots of δI_T, $\delta\theta$, and $\delta\phi$ are calculated for full-range orientation (i.e., $\Theta \in [0, \pi]$, $\Phi \in [0, 2\pi]$), as presented in Fig. 4.3. On each surface, the level represents the standard error of a calculated quantity at a specific orientation $\{\Theta, \Phi\}$ and a given total emission I_{tot}. The error surfaces δI_T, $\delta\theta$, and $\delta\phi$ exhibit different orientation dependences. All of them show periodic patterns which are the consequences of their trigonometric periodicity. It can be shown that the function of $\delta\phi$ has a factor $\sin^2\Theta$ in the denominator, and thus contains singularities at $\Theta = 0$ and π. This can be easily rationalized because of the rapid change in Φ around the poles, and the small noise in the intensities will lead to a large deviation from the true Φ. Unlike $\delta\phi$, the error surface $\delta\theta$ has an additional singular region at $\Theta = \pi/2$. It is because of the fact that the factor $\sin 2\Theta$ rather than $\sin^2\Theta$ appears in the denominator. By comparing the contour plots in Figs. 4.3(b), 4.3(c), the overall error contribution is higher in θ than in ϕ (solid angle averaging). The

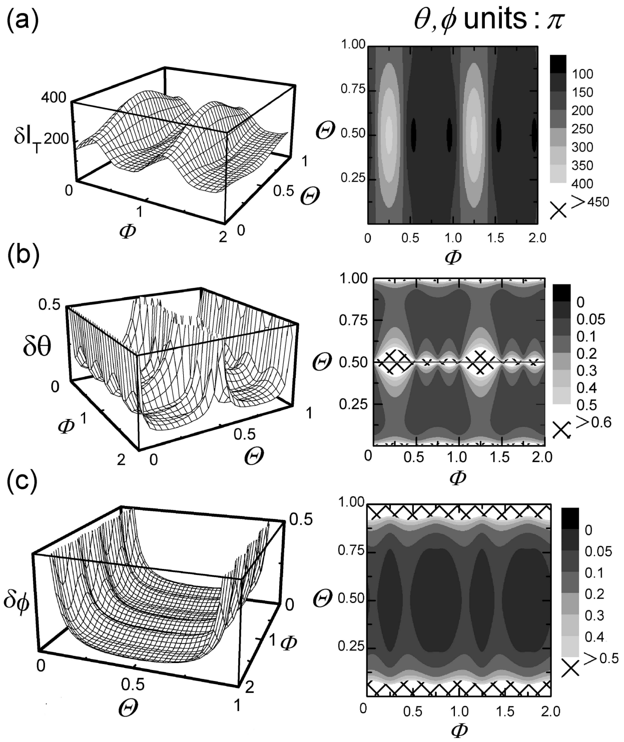

Figure 4.3: The error surface and contour plot of (a) I_T, (b) θ, and (c) ϕ as a function of dipole orientation $\{\Theta, \Phi\}$. The errors are calculated based on $I_{tot} = 2 \times 10^3$ level, and the upper bound of the error scales (0.5) shown in (b) and (c) is about 29^{o}.

region where $\delta\phi$ exceeds 0.5 ($\approx 30^{\text{o}}$) is concentrated about $\Theta = 0$ and π. This is where $\delta\theta$ exhibits similar deviations. In addition, $\delta\theta$ shows larger deviations when Θ is near $\pi/2$, and the area expands even more when $\Phi \approx \pi/4$ and $5\pi/4$. Lastly, we would like to discuss a special case in which the dipole orients in plane, i.e., $\Theta = \pi/2$. We particularly emphasize this situation because in some experiments the fluorophores are loaded on the surface or doped into a thin film. Due to the interface interaction, molecules may show a preference in

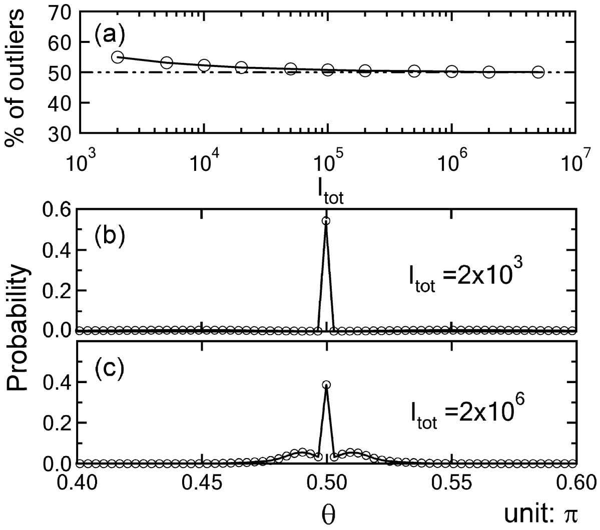

Figure 4.4: (a) Outlier percentages calculated from an in-plane dipole trajectory of size 10^6 for I_{tot} ranges from 2×10^3 to 5×10^6. Selected θ distributions are presented in (b) $I_{tot} = 2\times10^3$ and (c) $I_{tot} = 2\times10^6$. In the case $I_{tot} = 2\times10^3$, the probability, except for $\theta = \pi/2$, is too small to be seen and spread out over a large range.

specific orientations, such as lying in a plane perpendicular to the optical axis. If the emission dipoles align with the same surface, Θ will have a distribution centered around $\pi/2$. According to the previous discussion, we can expect that a large portion of $\{I_0, I_{45}, I_{90}\}$ will be uninvertable. To simulate this, trajectories with I_{tot}s ranging from 2×10^3 to 2×10^6 were generated. The angle Θ is fixed at $\pi/2$ and Φ is randomly chosen from $[0, 2\pi]$. With noise added, the percentage of uninvertable data (outliers) at various I_{tot}s are shown in Fig. 4.4(a). For the regions that are experimentally accessible with I_{tot} around 10^3, nearly 60% of the total points are outliers. About 50% of the points are outliers in the limit of very high I_{tot}. Since $\Theta = \pi/2$ is at the boundary of the domain of $\sin^2\theta$, it results that if $\delta\theta$ is symmetrically distributed, half of the possibility will be an outlier. This symmetry condition is valid only when I_{tot} is high. In the low I_{tot} case, the relatively higher noise contribution as well as the digitization procedure used in generating $\{I_0, I_{45}, I_{90}\}$ makes the error distribution asymmetric, and thus the percentage of outlier points will increase from 50%. The distributions of $\{\theta\}$ are also illustrated for $I_{tot} = 2 \times 10^3$ and 2×10^6 in Figs. 4.4(b), 4.4(c), respectively. In the former case, the points where $\theta \approx \pi/2$ (mostly from outliers) is higher, but the rest of the data is spread out over a larger range of θ. When I_{tot} is high, the distribution remains centered at the true value of $\pi/2$, but the probability of $\theta = \pi/2$ decreases.

4.4.2 Noise effect on the correlation functions of rotational diffusion

The correlation function of $\{Y_\ell^m(\Omega_t)\}$ obtained from a pure rotational diffusion has a decay form that is a single exponential. In the previous chapter, we have studied the behavior of correlation functions in the noise-free case. In theory, when the full orientation information $\{\Omega_t\}$ is known, all $\{Y_\ell^m(\Omega_t)\}$ will be available. However, the detected noise will degrade the precision of the data, and make it more difficult to extract orientation information from higher order correlation functions. The effect of the noise will be examined, and particular attention will be paid to the differences that occur when the higher order correlation functions are calculated.

As shown in Fig. 4.3, the error profiles are different for θ and ϕ. The overall $\delta\theta$ is larger and some $\{I_0, I_{45}, I_{90}\}$ have even become uninvertable because of the noise. Using the optimization algorithm, we can recover those bad points. However, the process tends to pick a θ which is closer to $\pi/2$ than the true value. This affects the distribution of $\{\theta\}$, as shown in Fig. 4.2. Pure rotational diffusion is an isotropic process. Since the effect of noise is different for θ than for ϕ, the Z axis, which is also the optical axis, will separate from X and Y. As a result, the coordinate $Z = \cos\theta$, which is the simplest spherical harmonic component Y_1^0, loses more accuracy due to the noise than if either of the other axes are chosen: $X = \sin\theta \sin\phi$ and $Y = \sin\theta \cos\phi$. Therefore, the correlation functions obtained from the Z coordinate are different from those computed from X and Y. With the same method, as previously described, we simulated angular trajectories of size 10^6 which were recovered from the intensities $\{I_0, I_{45}, I_{90}\}$ with noise added for $I_{tot} = 2\times10^3$ and 2×10^4. The calculated orientations $\{\theta, \phi\}$ were then transformed to the coordinates $\{X(\theta, \phi), Z(\theta)\}$. We considered both X and Z as Y_1^0, and thereby generate higher order terms: Y_2^0, Y_4^0, Y_6^0, and so on. The reason only even terms are chosen is because they are experimentally measurable due to the symmetry of the dipole. In order to make a comparison to a two-detector scheme, the linear dichroism $\{D\}$ is also calculated, but I_{tot} value is twice that of the three-detector scheme. In order to show the relative magnitude between functions, we chose sample covariance functions $\gamma(k)$, instead of correlation functions $[\gamma(k)/\gamma(0)]$ to represent the data. In Figs. 4.5 and 4.6, $\gamma(k)$s calculated from the Z-coordinate (denoted as 3 Det-Z), X-coordinate (3 Det-X), and two-detector scheme (2 Det) under

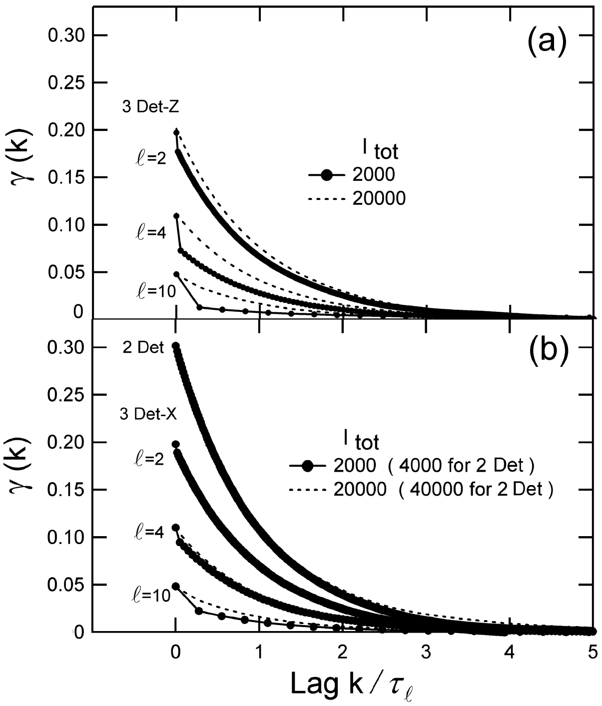

Figure 4.5: Covariance functions calculated from the reconstructed rotational diffusion trajectories of size 10^6 for orders $\ell = 2, 4, 10$ and $I_{tot} = 2 \times 10^3$ (filled circles) and 2×10^4 (dashed lines). The spherical harmonics are obtained from (a) Z (3 Det-Z) and (b) X (3 Det-X) trajectories. The results of the two-detector scheme (2 Det) are also presented in (b).

various conditions are presented. The 2 Det curve has the largest magnitude, whereas the case of the 3 Det- X,Z is smaller and decreases with ℓ. The 2 Det and the high I_{tot} 3 Det-X,Z curves can both be approximated with a single exponential decay. At low I_{tot}, the 3 Det-X,Z curves exhibit deviations and have a sudden drop at the second time point as a result of the noise. The overall decrease in the magnitude of the low I_{tot} curves arises from the lower correlation caused by the noise. In order to characterize the covariance functions, a

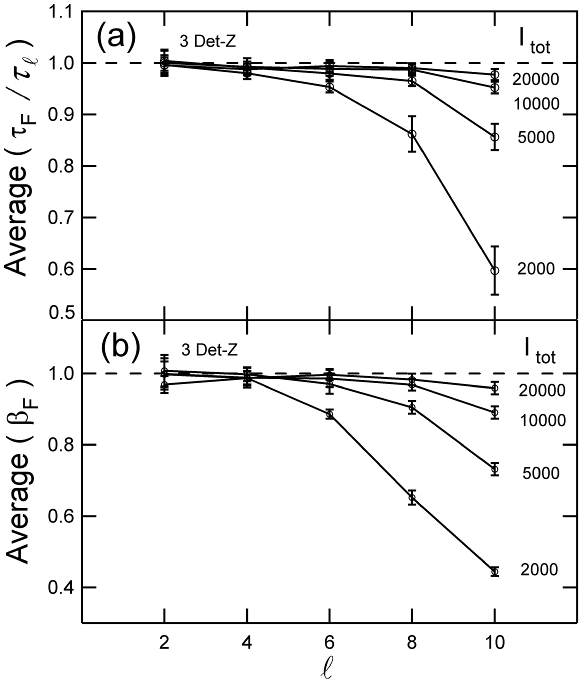

Figure 4.6: The (a) τ_F/τ_ℓ and (b) β_F are obtained from the covariance functions of reconstructed rotational diffusional Z trajectories with size 10^6. The trajectories are simulated under various I_{tot} levels and order ℓ. Each point is averaged from ten different calculations and the error bars represent the corresponding standard deviations. All covariance functions are fitted by a stretched exponential function in the range of $[1, 5\tau_\ell]$.

stretched exponential function is used to fit those curves. During the fitting the first point was dropped to avoid a discontinuity in shape of the curve. If the noise is "memory-less", it only affects the covariance/correlation function decay at the first point. Fitting the rest of the curve gives a better estimation of the decay constant when the noise effect does not propagate beyond the first point. The fitting results are presented in Fig. 4.6 (3 Det-Z) and Fig. 4.7 (3 Det-X and 2 Det). For the 3 Det-Z case, τ_Fs and β_Fs deviate from

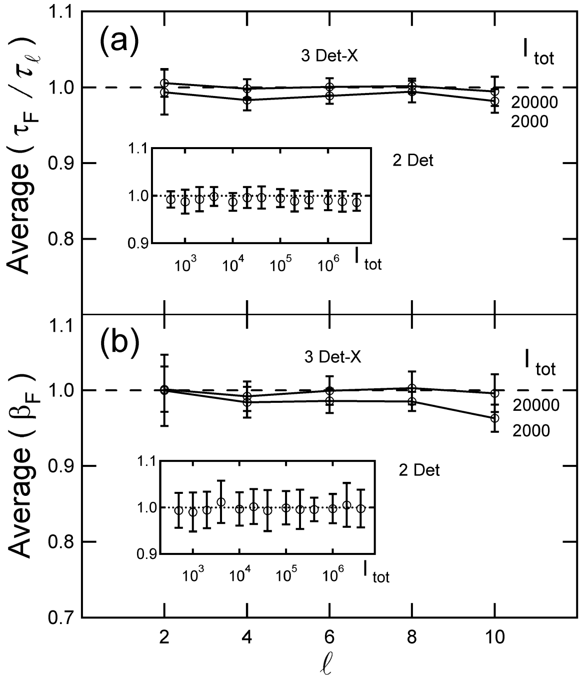

Figure 4.7: The (a) τ_F/τ_ℓ and (b) β_F are obtained from the covariance functions of reconstructed rotational diffusion X trajectories with size 10^6. The simulation conditions and the fitting range are predescribed in Fig. 4.6. The insets are the corresponding results calculated from two-detector linear dichroism under various I_{tot} levels.

one when ℓ increases. This trend becomes more prominent especially for low I_{tot}. When $I_{tot} = 2000$, the τ_F and β_F drop to ≈ 0.6 and ≈ 0.4, respectively, at $\ell = 10$. The deviations in τ_Fs and β_Fs imply the decay is no longer a single exponential, but has been “stretched” by the noise effect. However, in Fig. 4.7, τ_Fs and β_Fs for the 3 Det-X case do not show significant deviations from one. As for the 2 Det fittings, both τ_F and β_F agree with the single exponential decay with $\ell = 2$ over the range $I_{tot} = 5 \times 10^2$ to 5×10^6. From the previous discussion, it is clear that in the three-detector method choosing a coordinate is critical when calculating the rotational correlation/covariance function. In-plane coordinates (X, Y) are recommended because of the relatively small noise effect. The two-detector scheme is less vulnerable to noise even when I_{tot} is as low as 500. As the noise has a different effect on the 3 Det-Z and 3 Det-X, Y correlation functions, the difference between the in-plane and out-of-plane dynamics should not immediately be interpreted as a sign of anisotropic diffusion. Based on the statistics, the average correlation time for these two coordinates can differ significantly. In addition, even isotropic diffusion simulations yield a distribution of time constants calculated from individual trajectories. These trajectories are nonexponential despite molecular motion being governed by pure rotational diffusion. Given the effect of the noise, it is tempting to interpret this nonexponential behavior as resulting from a fluctuating diffusion constant. This effect is amplified as one observes higher order rotational diffusion constants.

4.4.3 Noise and finite size effect on the distributions of $\{\tau_F\}$ and $\{\beta_F\}$

In the previous chapter, we have shown that in the simple case of pure rotational diffusion, the τ_F and β_F fitted from a correlation function of finite size have distributions rather than being an exact number. These distributions arise from the statistical nature of finite sampling. In a real experiment, the size of data is always finite, and the observation time is quite limited by the stability of the system. Photobleaching determines the life span of fluorophores, and thus plays an important role in single molecule fluorescence measurements. [104, 105] As discussed in the previous section, signal noise will change the shape of covariance/correlation functions to a degree that depends on both the noise level and the type of function. This noise affects the sample correlation functions as well as the distributions of $\{\tau_F\}$ and $\{\beta_F\}$. The details about the sample correlation function calculation were described previously. [21] Briefly, an angular trajectory of size 10^7 and $\tau_1 = 200$ is generated for a specific I_{tot} and order ℓ. The long trajectory is then broken into pieces of the desired length. By calculating the sample correlation function and fitting it to a stretched exponential function, each piece is characterized with two parameters τ_F and β_F. Since a large number of correlation functions are obtained from the long trajectory, the collected $\{\tau_F\}$ and $\{\beta_F\}$ are used to estimate the average and standard deviation (SD) for a given trajectory size T. Also, based on the law of large numbers, the distributions of $\{\tau_F\}$ and $\{\beta_F\}$ can be mapped out if the sample size is sufficiently large. Again, there are some adjustments in the present fitting procedure than in the previous chapter. The first point is skipped during the fitting and the variables are constrained such that $\xi_F, \tau_F, \beta_F > 0$. The constraint $\xi_F = 1$ is released in order to make the fitting more flexible. As a consequence, small changes in the distributions will occur when the new fitting routine is applied.

The average and the SD as a function of trajectory size T under different conditions are presented in Figs. 4.8, 4.9. The noise-free trajectory is the raw diffusion data without the conversion to intensities. Thus, the results are not altered by the intensity conversion or detection limitations. Theoretically,

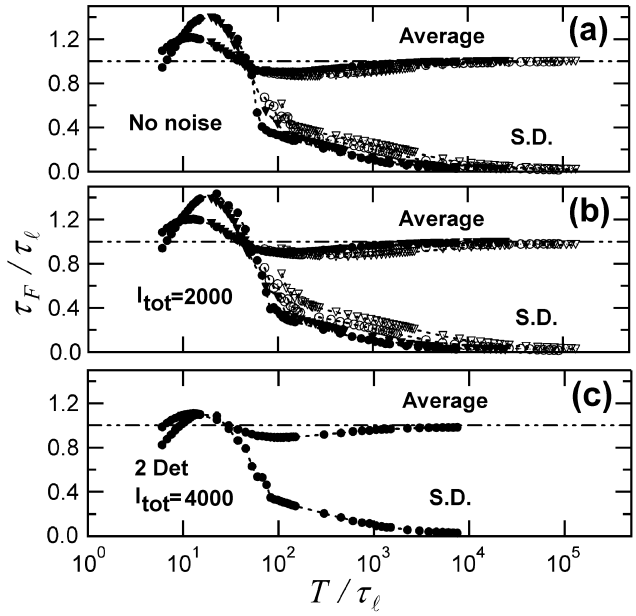

Figure 4.8: The average and standard deviation of τ_F/τ_ℓ plotted as a function of T/τ_ℓ for the cases: (a) noise-free, (b) $I_{tot} = 2 \times 10^3$, and (c) two-detector scheme. The points $\ell = 2$ (filled circles), $\ell = 4$ (filled triangles), $\ell = 8$ (open circles), and $\ell = 10$ (open triangles) are calculated from a long trajectory ($\tau_1 = 200$, length 10^7) broken into pieces of desired size T. The resulting values are the average of ten long trajectories.

under the normalized scheme ($\bar{\tau_F} = \tau_F/\tau_\ell, \bar{T} = T/\tau_\ell$) all $\bar{\tau_F}(\bar{T})$ and $\beta_F(\bar{T})$ should fall into the same average and SD standard curves as long as $\tau_\ell \gg 5$. [21] In Figs. 4.8(a), 4.9(a), the average curves of $\bar{\tau_F}$ and β_F for $\ell = 2$, 4, 8, and 10 exhibit good agreement with each other in most regions. However, the $\ell = 8$ and $\ell = 10$ SD curves for both $\bar{\tau_F}$ and β_F deviate away from the standard curve. This can be explained by the poor fitting quality and the breakdown of the constraints in comparison to the standard curves. Neither time constant $\tau_8 \approx 5.56$ nor $\tau_{10} \approx 3.64$ satisfies the condition $\tau_\ell \gg 5$, which

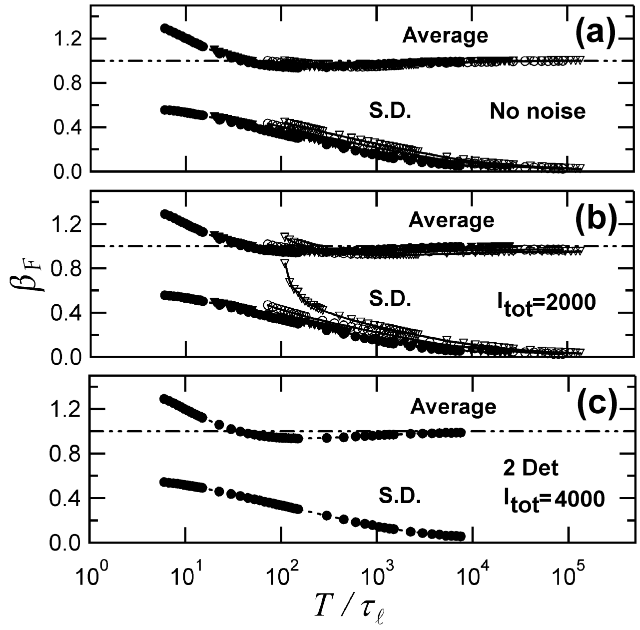

Figure 4.9: The average and standard deviation of β_F as a function of T/τ_ℓ from the same calculations described in Fig. 4.8: (a) noise-free, (b) $I_{tot} = 2 \times 10^3$, and (c) two-detector, where the symbols are assigned for $\ell = 2$ (filled circles), $\ell = 4$ (filled triangles), $\ell = 8$ (open circles), and $\ell = 10$ (open triangles), respectively.

is required for the standard form. For the small τ_ℓ cases, the fitting process becomes very unstable and unreliable since only a few points are used to calculate in the decay. A wider range of $\bar{\tau_F}$ is obtained and the SD for large ℓ thereby increases. Due to a few extremely large fitting results that appear in the data, the curve occasionally exhibits "peaks". In such a case, the nonrealistic data points were manually removed. When $\bar{T}$ is large ($> 10^3$), both $\bar{\tau_F}$ and β_F approach 1, which is the expected value for pure rotational diffusion. However, when $\bar{T}$ gets smaller, the average curves of $\bar{\tau_F}$ and β_F

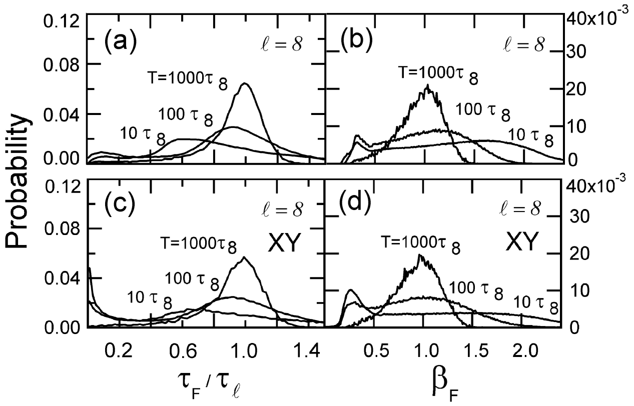

Figure 4.10: Distributions of τ_F and β_F calculated from [(a) and (b)] $\ell = 2$ noise-free rotational diffusion trajectories; [(c) and (d)] three-detector, $I_{tot} = 2 \times 10^3$, $\ell = 2$ (X, Y); [(e) and (f)] three-detector, $I_{tot} = 2 \times 10^3$, $\ell = 2$ (Z), and [(g) and (h)] two-detector, $I_{tot} = 4 \times 10^3$, with respect to different Ts ($10\tau_\ell$, $100\tau_\ell$, $1000\tau_\ell$). Each curve is calculated from 100 trajectories ($\tau_1 = 200$, length 10^7), then broken into pieces of desired size T. The bin sizes are 0.02 and 0.01 for τ_F and β_F, respectively.

deviate up and down by about 1, depending on which range $\bar{T}$ belongs to. The SD curves increase with decreasing $\bar{T}$ because small samples exhibit large fluctuations in the correlation functions. When $10 < \bar{T} < 50$, the $\bar{\tau_F}$ SD is even larger than the average. However, due to the zero-filling effect, both the $\bar{\tau_F}$ average and SD curves suddenly decline when $\bar{T} < 10$. The results for $I_{tot} = 2000$ with noise effect added are presented in Figs. 4.8(b), 4.9(b). The trends of $\bar{\tau_F}(\bar{T})$ and $\beta_F(\bar{T})$ are similar to the corresponding noise-free examples. When noise is included, the fitting becomes more difficult especially for $\ell = 8$ and $\ell = 10$. The SD curves deviate further from the standard scheme, and in the large $\bar{T}$ limit, both $\bar{\tau_F}$ and β_F are slightly lower than 1, which is consistent with the results shown in Fig. 4.6. Histograms of

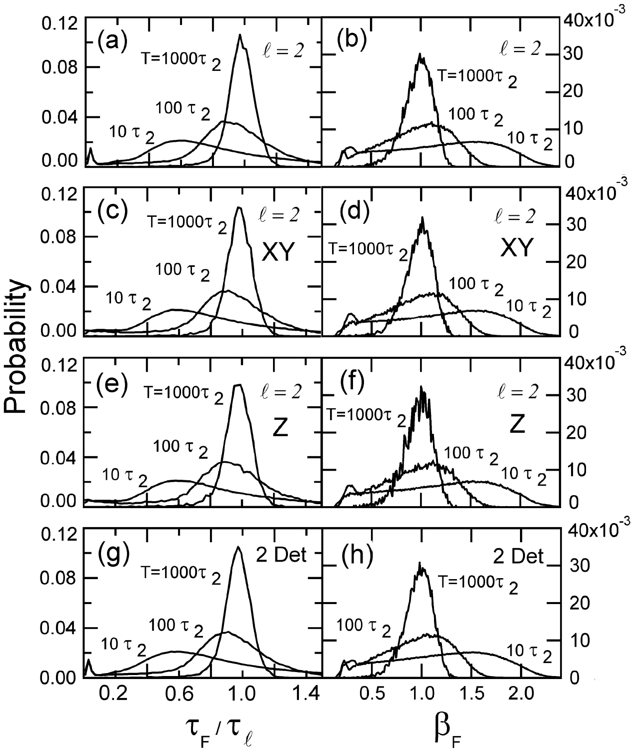

Figure 4.11: Distributions of τ_F and β_F calculated from [(a) and (b)] $\ell = 8$ noise-free rotational diffusion trajectories and [(c) and (d)] three-detector, $I_{tot} = 2 \times 10^3$, $\ell = 8$ (X, Y), with respect to different Ts ($10\tau_\ell$, $100\tau_\ell$, $1000\tau_\ell$). The calculation details are the same as in Fig. 4.10, except for the trajectory size is 10^6. About 4.5% of the fittings failed in $\ell = 8$ noise-free cases due to the ill-defined curve shape of small samples, whereas for $\ell = 2$, the percentage of failed fitting is only 0.3. When noise is added, the failed fittings in $\ell = 8$ (X, Y) increased to about 6%.

$\{\bar{\tau_F}\}$ and $\{\beta_F\}$ for $\bar{T} = 10$, 10^2, and 10^3 show the detailed shapes of the distributions. The noise-free and $I_{tot} = 2000$ distributions are presented in Figs. 4.10, 4.11. For $\ell = 2$, no significant differences in the distributions are observed between the distribution for different coordinates with and without noise [noise-free, Figs. 4.10(a), 4.10(b); $I_{tot} = 2000$ X, Figs. 4.10(c), 4.10(d); Z, Figs. 4.10(e), 4.10(f)]. However, there are significant differences for the higher order correlation function. For the $\ell = 8$ case [noise-free, Figs. 4.11(a), 4.11(b); $I_{tot} = 2000$ X, Figs. 4.11(c), 4.11(d)] the distributions become more broad. For the very short transients, $T = 10\tau_8$, the curves no longer have well-defined shapes. Due to the serious deviation from a single exponential, a large portion of the correlation functions could not be fitted with a stretched exponential in the 3 Det-Z $\ell = 8$ calculations and thus are not presented. Therefore, when looking at higher orders, whatever could be gained as an advantage in trajectory length is lost to the difficulty in estimating the correlation functions. This can be seen when comparing $T = 1000\tau_8$ and $T = 100\tau_2$ which are effectively the same length. The distribution for the $\ell = 8$ transients is nearly identical to the $\ell = 2$ despite that fact that they are effectively ten times longer. Lastly, the two-detector results are shown and compared [Figs. 4.8(c), 4.9(c), 4.10(g), 4.10(h)]. The trends of 2 Det curves are almost the same as the noise-free case, except for the smaller average and SD in $\bar{\tau_F}$ when $\bar{T} < 50$.

4.5 Dicussion and conclusions

In this work, the detailed properties of single fluorophore orientation reconstruction under the context of three-angle polarization measurements are discussed. The pure rotational diffusion model is adopted in the simulation to demonstrate the way of extracting rotational dynamics through correlation function analysis. According to Fourkas' formula, the total emission and the dipole orientation $\{I_T, \theta, \phi\}$ can be inverted from the intensities measured at three different polarizations $\{I_0, I_{45}, I_{90}\}$ by using Eqs. (4.2)(4.3)(4.4). In order to evaluate the noise effect, shot noise was added to the three signals and was propagated as error for the total intensity and the angles. The resulting error surfaces indicate that the error in estimating $\{I_{tot}, \Theta, \Phi\}$ will depend on the orientation. Most importantly, the surfaces show singularities at specific angles: $\Theta = 0$ and π for $\{\delta\phi\}$; $\Theta = 0$, $\pi/2$, and π for $\{\delta\theta\}$. When $\Theta = \pi/2$, some intensity combinations become uninvertable. In this situation, an optimization method is proposed to determine $\{I_T, \theta, \phi\}$. Although the optimization algorithm recovers the originally uninvertable data, it tends to select θs which are closer to $\pi/2$. As a result, the θ trajectory is flattened to $\pi/2$ when there are many outliers, and the θ histogram shows a peak at $\pi/2$. A special case when the dipole Θ is fixed at $\pi/2$, greater than 50% of the points will be uninvertable. The distribution $\{\theta\}$ also varies at different I_{tot} levels, as shown in Fig. 4.4. This situation may occur frequently in experiments where the fluorophores are restricted to a surface.

Due to the different error properties of θ and ϕ, the pure rotational diffusion trajectory recovered from $\{I_0, I_{45}, I_{90}\}$ is no longer spatially isotropic. The $Z = \cos\theta$ trajectory suffers more from the noise than X and Y. By calculating the covariance functions for pure rotational diffusion trajectories under various conditions, it is shown that the shape of the curves becomes stretched, especially for the trajectories obtained from the Z coordinate of larger ℓ and lower I_{tot}. Again, even for the idealized case of background free isotropic diffusion, significant differences are observed in the correlation functions for X and Z because of the greater loss of accuracy due to the noise in the Z coordinate. In-plane and out-of-plane motions should be analyzed with caution before interpreting the results as anything more complex than statistical fluctuations.

Both the three-detector X, Y correlation functions and the two-detector scheme show excellent agreement with single exponential decays. The noise has an effect on the distribution of time constants and stretching exponents for the measured decays. $\bar{\tau_F}(\bar{T})$ and $\beta_F(\bar{T})$ curves as well as the selected distribution profiles for $\bar{T} = 10$, 10^2, and 10^3 were examined. Not only the noise but also the finite sample effect will change the trends observed for the curves. The average and the SD curves deviate more from the standard curves, and the distribution becomes even broader in higher order cases. In the large $\bar{T}$ limit, the finite size effect can be ignored. The $\bar{\tau_F}(\bar{T})$ and $\beta_F(\bar{T})$ curves of $\ell = 8$ and $\ell = 10$ obtained from the trajectory with noise, slightly deviate from one. The deviations imply that artifacts are introduced by the noise and the reconstruction method itself, not from finite sampling.

Finally, the above results provide a guideline for choosing a proper experimental design. It is clear that if one only cares about the lowest available order, $\ell = 2$, then the two-detector scheme will be the most economical choice and retain acceptable performance. This method is limited as it does not yield angular trajectories. The three-angle polarization measurements can measure the angles and further calculate higher order rotational correlation functions. Care should be taken when examining details of the angular distributions particularly for angles near $\Theta = \pi/2$. For calculating correlation functions, the coordinates X and Y yield useful correlation functions while the Z coordinate is dominated by the noise. X and Y correlation functions up to rank $\ell = 6$ can be measured but higher ranks suffer from excessive noise. The higher order correlation function shows a different dependence on trajectory length and noise, so very little is gained when attempting to extend effective transient length by calculating them. It should be possible to test different models of diffusion by comparing the correlation function of different ranks as measured with the three-detector method.

Chapter 5

How geometric relaxation in metallic nanoparticles affect the oxygen reduction reaction

5.1 Abstract

Better oxygen reduction catalysts are needed to improve the efficiency and lower the cost of fuel cells. Metal nanoparticles are good candidates for new catalysts because their catalytic properties are different from bulk metals. Using density functional theory calculations, we studied the geometric relaxation of metal nanoparticles for the oxygen reduction reaction. Result show Pt and Au exhibit a larger structural deformation than other metals especially when the particle size is less than 100 atoms. Structural deformation induced by atomic oxygen binding stabilizes the oxidized state and thus reduces the catalytic activity of Pt-based random alloys. Catalytic performance of Pt can be improved by making alloys with less deformable metals which is also illustrated in this study.

5.2 Introduction

Fuel cells are attractive power sources since potentially they can convert chemical energy to electricity with high efficiency. However, there are several limitations of current proton-exchange membrane fuel cells. The most important issues are related to the catalyst at the cathode. Better and less-expensive catalysts are needed to make the widespread use of low temperature fuel cells viable. Bimetallic alloys, for example, provide a particularly exciting possibility for tuning the reactivity of catalysts. In certain cases, new property can appear in the alloy system which is absent in the constituent metals. [106, 107]

Computer modeling has become a powerful tool in screening potential candidates of fuel cell catalysts. Using the binding energy of atomic oxygen as a measurement of the ORR (oxygen reduction reaction) activity in the metal catalysts was proposed by Bligaard et al. [30] For metals other than Ag and Au, a weaker oxygen binding energy would increase the ORR activity. While a large portion of recent studies focus on the electronic properties of catalyst, the geometric contribution to the catalytic activity has received less attention. From a chemistry point of view, changes in binding site geometry should also play an important role in chemical reactions. This is especially important for metal catalysts when the particles size goes down to nano- or subnano-region. [108]

For Pt-based random alloy, when oxygen adsorbed on the metal surface, the structural deformation can stabilize the oxidized states and thus reduces the catalytic activity. The possibility of improving catalytic performance by making alloys with less deformable metals is discussed below.

5.3 Methodology

5.3.1 Density function theory (DFT) calculation

Our calculations of atomic oxygen adsorption on metallic surfaces were done with density functional theory (DFT), using the generalized gradient approximation with the PW91 functional [109] as implemented in the VASP code. [110, 111] Valance electrons were treated explicitly in the Kohn-Sham [112] equations and core electrons were described by pseudopotentials with the projector augmented-wave (PAW) method. [113, 114] A plane-wave basis set with an energy cutoff of 251 eV was used for all calculations except for particles containing Cu (274 eV). Spin-polarization was tested in all cases and used as needed. Stable structures were calculated using force-based energy minimization. Geometries were considered optimized when the force on each atom was less than 0.003 eV/Å.

5.3.2 System geometry and configuration

5.3.2.1 Metallic slab

Single crystal surfaces were modeled with 4 layer slabs containing 9 atoms per layer in a p(3×3) unit cell of the (111) surface (Fig. 5.1). Since the face-centered-cubic (FCC) hollow exhibits the weakest oxygen binging strength, it is considered as the most ORR active site. In the simulation,

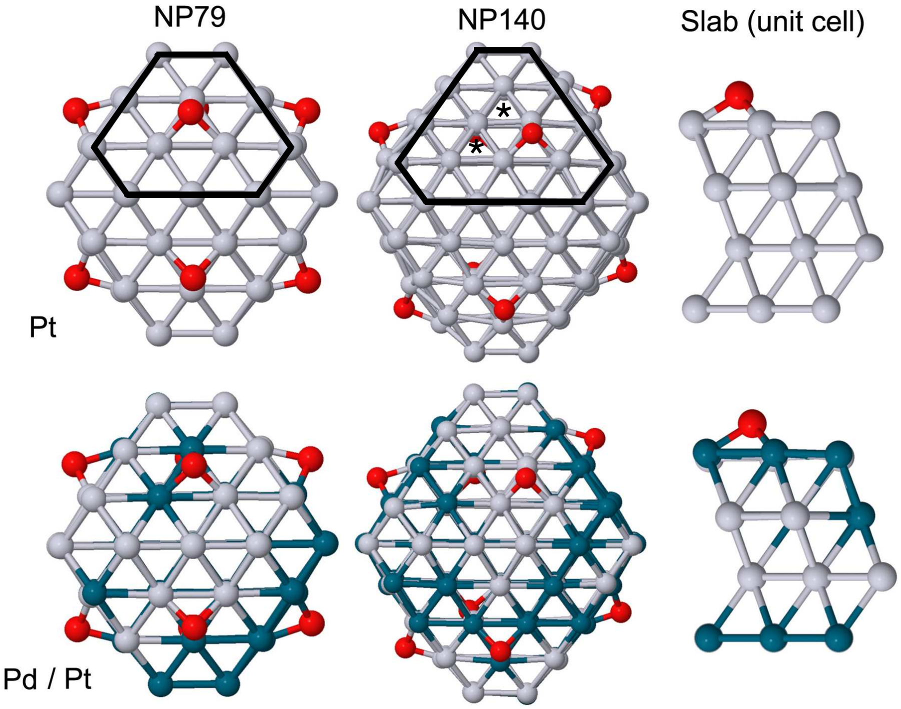

Figure 5.1: Structures of NP79, NP140 and slab unit cell bound with oxygen atoms (red). One of the (111) surface in both NP79 and NP140 is shown (the region surrounded by solid black line). In NP140, two other FCC hollow sites were marked with a $*$. The top and bottom row show the structures for pure Pt and Pd / Pt (1:1) random alloy respectively.

an oxygen atom was adsorbed on one of the FCC hollows. A surface of this size and a vacuum gap of at least 10Å between slabs (in the z direction) was used to isolate adsorbed oxygen atoms from their periodic images. A $(3\times3\times1)$ Monkhost Pack k-point mesh was used to sample the Brillouin zone. [115] In all calculations, the bottom two layers of the slab were held frozen in their lattice positions.

5.3.2.2 Metal nanoparticles

Nanoparticles (NPs) were modeled as a FCC crystallite in the shape of a truncated octahedron (Fig. 5.1). The truncated octahedron was found to be the most stable structure for a pure Pt particle of 79 atoms (denoted as NP79). The particles were contained in a cubic box of side length 20Å (NP79) or 23Å (NP140). Since the particles were isolated by a vacuum gap in all directions, a single Γ-point sampling of the Brillouin zone was used. Eight oxygen atoms were adsorbed on the center FCC hollows of NP79. For NP140, eight oxygen atoms were adsorbed symmetrically on one of the center FCC hollow sites in each facet (shown in Fig. 5.1). During the minimization all atoms in the nanoparticles were allowed to relax.

5.3.2.3 Random alloy

Random alloy configurations were generated by randomly shuffling the type of atoms in a bimetallic NP/slab. A total of 12, 12 and 10 different configurations were used in the NP79, NP140 and slab calculations, respectively.

5.3.3 Oxygen binding energy decomposition

The average oxygen binding energy E_{tot} is defined as the energy change per adsorbed oxygen atom as compared to O_2 and the metal. As illustrated

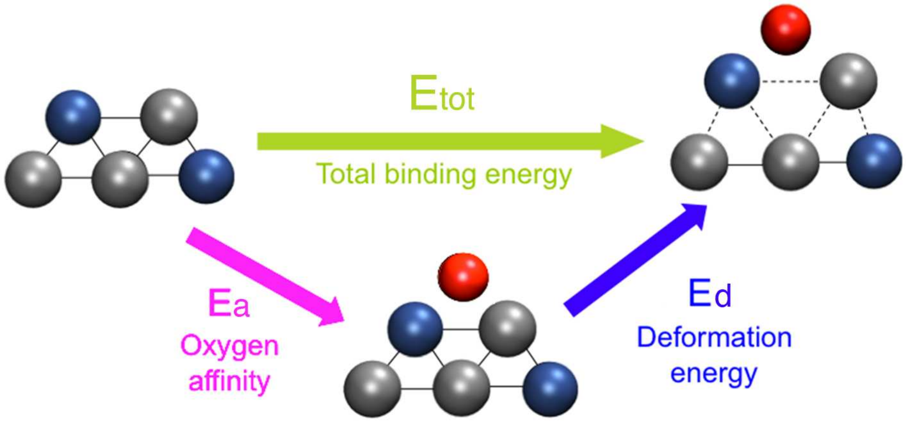

Figure 5.2: The total oxygen binding energy (E_{tot}) is decomposed into an oxygen affinity energy (E_a) component and a deformation energy (E_d) component.

in Fig. 5.2 and the derivation below, E_{tot} can be decomposed into two parts

$$\begin{aligned} E_{tot} &= \frac{E_{MO_x} - E_M - (x/2)E_{O_2}}{x} \\ &= \frac{E_{MO_x} - E_{MO_x}^{(\text{frozen})}}{x} + \frac{E_{MO_x}^{(\text{frozen})} - E_M - (x/2)E_{O_2}}{x} \\ &= E_d + E_a \end{aligned} \tag{5.1}$$

where X is the number of bound oxygen atoms, E_{M} is the optimized energy of the NP/slab, $E_{\mathrm{MO}x}$ is the energy of the oxygen-bound NP/slab with the metal atoms either in a relaxed or frozen structure as specified. E_{O_2} is the energy of a gas phase O_2 molecule. E_d is defined as the energy of geometric relaxation and E_a is the energy of oxygen affinity to the metal surface. In the following, we focus on the relationships between E_{tot}, E_a and E_d in both the pure metal and alloy systems.

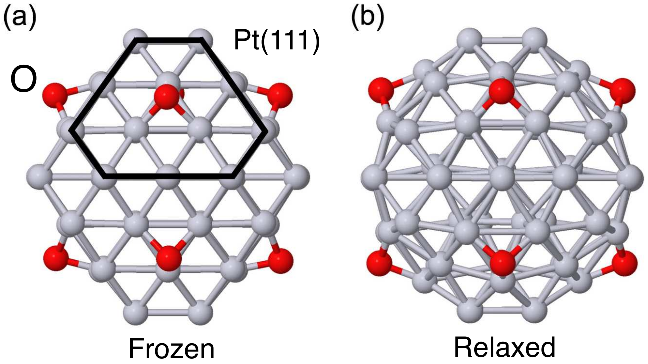

Figure 5.3: The optimized structure of Pt NP79 (grey) bound with eight oxygen atoms (red). All oxygen atoms bind to the center FCC hollow of the (111) facets. The calculations were done for (a) a frozen particle and (b) a relaxed particle where all Pt atoms are allowed to move during the energy minimization.

5.4 Results and discussion

5.4.1 Decomposition of E_{tot} for pure metallic NP79

As shown in Fig. 5.3, eight oxygen atoms bound to the Pt NP79 with frozen and movable atoms result in different geometries. According to Eq. (5.1), the energy difference between the two structures is equal to (eight times) E_d. The value of E_d can be used as a measure of the metal deformation whereas the binding energy to the frozen particle, E_a, reflects the intrinsic metal-oxygen affinity. The values of E_d and E_a for various metal NP79 are summarized in Fig. 5.4. The result shows that the E_d contribution for most metals are much less than E_a, except for Au and Pt. For metals such as Ag, Pd, Cu, Ir and Rh the overall oxygen binding strength is mainly determined by their intrinsic oxygen affinity E_a. The geometric contribution E_d is surprisingly high for Pt and Au which indicates the structure relaxation plays an important role in the

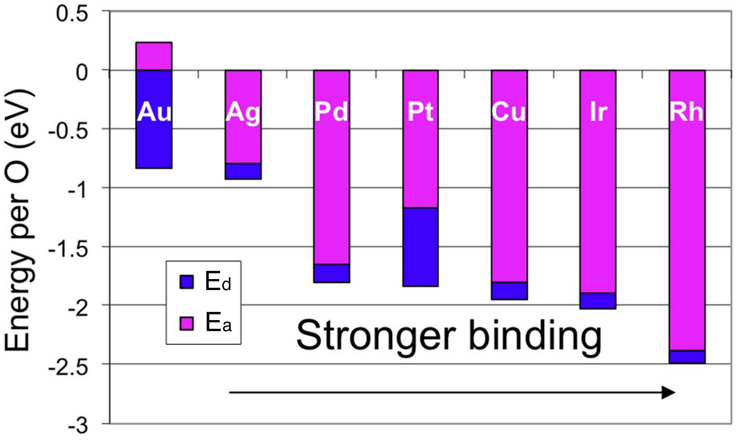

Figure 5.4: The energies E_d (blue) and E_a (pink) for various metal NP79. The sum of E_d and E_a (with sign) in each column is equal to the total oxygen binding energy. Pt and Au show similar binding strength as the adjacent metals on the plot but the driving force of oxygen binding is quite different.

oxygen binding process.

5.4.2 Decomposition of E_{tot} for Pt-based bimetallic random-alloy systems

When two metals form a random alloy, the resulting binding energy could be very different from the interpolation of the pure metals. Fig. 5.5(a) summarizes the total oxygen binding energy for Pd/Pt random alloys in the forms of NP79, NP140 geometries and slabs. Each data point is averaged over 12 different configurations (10 for the slab) of the same composition. For the slabs and NP140 geometry, the total binding energy increases (becomes less negative) monotonically with Pt ratio. The curve shape changes dramatically to convex when the particle size reduces to 79 atoms. The energy decompo-

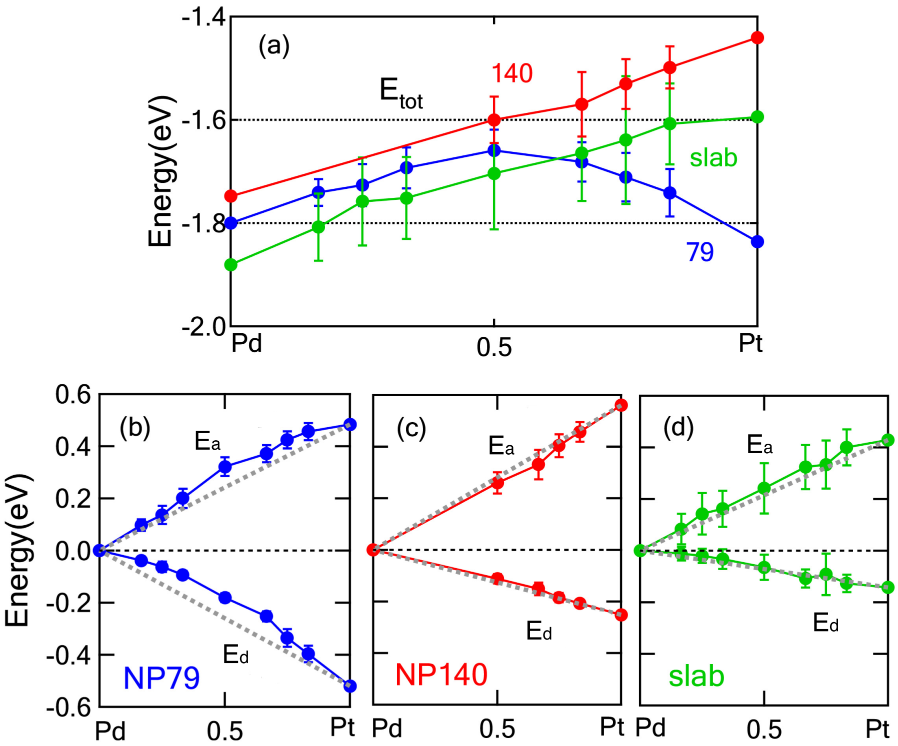

Figure 5.5: (a) The total oxygen binding energy and the energy decomposition of Pd/Pt random alloy in the forms of NP79 (b), NP140 (c) and slab (d) at various compositions. To make comparison easier, all the curves in (b), (c) and (d) were shifted to make the left end values zero. The dashed lines in (b), (c) and (d) represent the linear interpolations from the data of pure metals.

sition in Fig. 5.5(b), 5.5(c) and 5.5(d) exhibits strong size dependence in E_d. The change in E_d becomes comparable to that in E_a when the particle size goes down, and the effect is significant at high Pt ratio as inferred from Fig. 5.4. Also one may notice that the E_a and E_d curves of NP79 are actually not linear but have a convex shape. In the Pd rich region, the change of E_d is relatively small. Therefore the slope of E_{tot} is determined by the trend of E_a

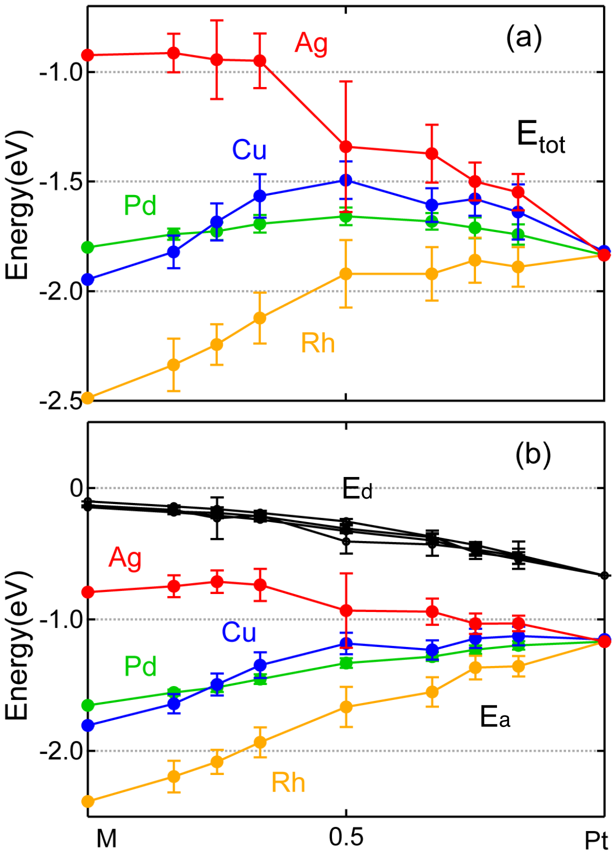

Figure 5.6: (a) The total oxygen binding energy and (b) the energy decomposition of Pt-based random alloy NP79 at various compositions. The Colored E_a curves represent the following types of alloy: Ag/Pt (red), Rh/Pt (yellow), Pd/Pt (green) and Cu/Pt (blue). Since the E_d curves are similar, their colors are kept in black for visual clarity.

curve. On the contrary, in the Pt rich region the trend of E_{tot} is dominated by the slope of E_d curve. The above factors explain why the E_d trend in NP79 reverses at high Pt ratio and looks so different from the curves of NP140 and slab geometry.

Here we introduce the terms “hard” and “soft” to distinguish whether a metal is prone to deform in response to oxygen binding. In the previous example we know the geometry relaxation is mainly from Pt which we considered as a “soft” metal. When hard metal forms alloy with Pt, it will not only change the oxygen affinity (E_a) but also make the alloy harder (E_d). The effect can be observed in other Pt based alloys. The oxygen binding energy curves and the corresponding energy decompositions for Ag/Pt, Pd/Pt, Cu/Pt and Rh/Pt NP79 are summarized in Fig. 5.6. According to Fig. 5.4, we know all these four metals are hard but differ in the oxygen affinity. The E_d curves in Fig. 5.6(b) are nicely overlapped which indicates that all hard metals look the same to Pt and the trend of the E_d curve can be considered characteristic of Pt. Therefore the difference in E_a determines the binding trend of these alloys. Among them, Rh have the strongest oxygen affinity and thus its binding curve shown in Fig. 5.6(a) is dominated by E_a. Unlike other metals, the E_a curve of Ag has the same sign of slope as E_d. Both of them are energetically unfavorable when the Ag ratio increases. As a result, the Ag binding curve exhibits an opposite trend to Rh. The E_d curves of Pd and Cu lay in between and their magnitude of changes in E_d are comparable to the change in E_a. Therefore their binding curves turn out to be a convex peaked in the middle as a compromise between changes in E_a and E_d.

5.5 Conclusion

From the above discussion, we know when the size of a metal particle is small (less than 100 atoms) the geometric relaxation induced by oxygen binding becomes significant for soft metals such as Pt and Au. The overall oxygen binding energy is thus the balance between the intrinsic oxygen affinity and the geometric relaxation energy. Geometric relaxation can significantly stabilize the particle and, for Pt alloys, reduce the ORR activity. One possible way to fine tune the binding energy is by making an alloy. Our calculations show that by introducing hard metals such as Pd or Cu, their mild oxygen affinity will not change the overall oxygen affinity dramatically but instead the binding energy can be adjusted by suppressing the structural relaxation. This concept provides an alternative way to manipulate the electronic structure for the rational design of nano-metallic ORR catalysts.

Bibliography

[1] G. H. Vineyard. Frequency factors and isotope effects in solid state rate processes. *J. Phys. Chem. Solids*, 3:121–127, 1957.

[2] L. Xu and G. Henkelman. Adaptive kinetic Monte Carlo for first-principles accelerated dynamics. *J. Chem. Phys.*, 129:114104, 2008.

[3] A. F. Voter, F. Montalenti, and T. C. Germann. Extending the time scale in atomistic simulation of materials. *Annu. Rev. Mater. Res.*, 32:321–346, 2002.

[4] A. F. Voter. Parallel replica method for dynamics of infrequent events. *Phys. Rev. B*, 57:R13985–R13988, 1998.

[5] A. F. Voter. Hyperdynamics: Accelerated molecular dynamics of infrequent events. *Phys. Rev. Lett.*, 78:3908–3911, 1997.

[6] A. F. Voter. A method for accelerating the molecular dynamics of infrequent events. *J. Chem. Phys.*, 106:4665–4677, 1997.

[7] R. A. Miron and K. A. Fichthorn. Accelerated molecular dynamics with the bond-boost method. *J. Chem. Phys.*, 119:6210–6216, 2003.

[8] M. M. Steiner, P. A. Genilloud, and J. W. Wilkins. Simple bias potential for boosting molecular dynamics with the hyperdynamics scheme. *Phys.*

Rev. B, 57:10236–10239, 1998.

[9] H. Jónsson, G. Mills, and K. W. Jacobsen. Nudged elastic band method for finding minimum energy paths of transitions. In B. J. Berne, G. Ciccotti, and D. F. Coker, editors, *Classical and Quantum Dynamics in Condensed Phase Simulations*, pages 385–404. World Scientific, Singapore, 1998.

[10] G. Henkelman, B. P. Uberuaga, and H. Jónsson. A climbing image nudged elastic band method for finding saddle points and minimum energy paths. *J. Chem. Phys.*, 113:9901–9904, 2000.

[11] W. E. Moerner. New directions in single-molecule imaging and analysis. *Proc. Nat. Acad. Soc.*, 104:12596–12602, 2007.

[12] W. E. Moerner and D. P. Fromm. Methods of single-molecule fluorescence spectroscopy and microscopy. *Rev. Sci. Instrum.*, 74:3597–3619, 2003.

[13] W. E. Moerner. A dozen years of single-molecule spectroscopy in physics, chemistry, and biophysics. *J. Phys. Chem. B*, 106:910–927, 2002.

[14] B. Hecht, B. Sick, U. P. Wild, V. Deckert, R. Zenobi, O. J. F. Martin, and D. W. Pohl. Scanning near-field optical microscopy with aperture probes: Fundamentals and applications. *J. Chem. Phys.*, 112:7761–7774, 2000.

[15] J. B. Pawley. *Handbook of biological confocal microscopy*. Springer, new York, 3rd edition, 2006.

[16] Y. Sako and T. Uyemura. Total internal reflection fluorescence microscopy for single-molecule imaging in living cells. *Cell Structure and Function*, 27:357–365, 2002.

[17] X. S. Xie. Enzymology and life and the single molecule level. *Single Molecule Spectroscopy in Chemistry, Physics and Biology Nobel Symposium*, pages 435–448, 2010.

[18] X. S. Xie, P. J. Choi, G.-W. Li, N. K. Lee, and G. Lia. Single-molecule approach to molecular biology in living bacterial cells. *Annu. Rev. Biophys*, pages 417–444, 2008.

[19] H. Yang and X. S. Xie. Statistical approaches for probing single-molecule dynamics photon-by-photon. *Chem. Phys.*, pages 423–437, 2002.

[20] H. Yang and X. S. Xie. Probing single molecule dynamics photon by photon. *J. Chem. Phys.*, pages 10965–10979, 2002.

[21] C.-Y. Lu and D. A. Vanden Bout. Effect of finite trajectory length on the correlation function analysis of single molecule data. *J. Chem. Phys.*, 125:124701, 2006.

[22] J. M. Stellman. *Encyclopaedia of occupational health and safety*, volume 3. International labour office, Geneva, 4th edition, 1998.

[23] M. Haruta. Size- and support-dependency in the catalysis of gold. *Catal. Today*, 36:153–166, 1997.

[24] M. Valden, X. Lai, and D. W. Goodman. Onset of catalytic activity of gold clusters on titania with the appearance of nonmetallic properties. *Science*, 281:1647–1650, 1998.

[25] W. Tang and G. Henkelman. Charge redistribution in core-shell nanoparticles to promote oxygen reduction. *J. Chem. Phys.*, 130:194504, 2009.

[26] M. Mavrikakis, B. Hammer, and J. K. Nørskov. Effect of strain on the reactivity of metal surfaces. *Phys. Rev. Lett.*, 81:2819–2822, 1998.

[27] B. Hammer and J. K. Nørskov. Electronic factors determining the reactivity of metal surfaces. *Surf. Sci.*, 343:211–220, 1995.

[28] J. N. Brönsted. Acid and basic catalysis. *Chem. Rev.*, 5:231–338, 1928.

[29] M. G. Evans and N. P. Polanyi. Inertia and driving force of chemical reactions. *Trans. Faraday Soc.*, 34:11, 1938.

[30] T. Bligaard, J. K. Nørskov, S. Dahl, J. Matthiesen, C. H. Christensen, and J. Sehested. The Brønsted-Evans-Polanyi relation and the volcano curve in heterogeneous catalysis. *J. Catal.*, 224:206–217, 2004.

[31] J. A. Dumesic, D. F. Rudd, L. M. Aparicio, J. E. Rekoske, and A. A. Trevi no. *The Microkinetics of Heterogeneous Catalysis.* Am. Chem. Soc., Washington, DC, 1993.

[32] M. Boudart and G. Djéga-Mariadassou. *Kinetics of Heterogeneous Catalytic Reactions*. Princeton Univ. Press, Princeton, NJ, 1984.

[33] J. K. Nørskov, J. Rossmeisl, A. Logadottir, L. Lindqvist, J. R. Kitchin, T. Bligaard, and H. Jónsson. Origin of the overpotential for oxygen reduction at a fuel-cell cathode. *J. Phys. Chem. B*, 108:17886–17892, 2004.

[34] A. F. Voter and M. R. Sørensen. Accelerating atomistic simulations of defect dynamics: Hyperdynamics, parallel replica dynamics, and temperature-accelerated dynamics. *Mat. Res. Soc. Symp. Proc.*, 591:427, 2000.

[35] M. R. Sørensen and A. F. Voter. Temperature-accelerated dynamics for simulation of infrequent events. *J. Chem. Phys.*, 112:9599–9606, 2000.

[36] A. B. Bortz, M. H. Kalos, and J. L. Lebowitz. A new algorithm for Monte Carlo simulation of Ising spin systems. *J. Comput. Phys.*, 17:10, 1975.

[37] D. T. Gillespie. A general method for numerically simulating the stochastic time evolution of coupled chemical reactions. *J. Comp. Phys.*, 22:403–434, 1976.

[38] H. Eyring. The activated complex in chemical reactions. *J. Chem. Phys.*, 3:107–115, 1935.

[39] E. Wigner. The transition state method. *Trans. Faraday Soc.*, 34:29–41, 1938.

[40] J. C. Keck. Variational theory of chemical reaction rates applied to threebody recombinations. *J. Chem. Phys.*, 32:1035–1050, 1960.

[41] J. C. Keck. Statistical investigation of dissociation cross-sections for diatoms. *Dicuss. Faraday Soc.*, 33:173–182, 1962.

[42] J. B. Anderson. Statistical theories of chemical reactions. distributions in the transition region. *J. Chem. Phys.*, 58:4684–4692, 1973.

[43] A. F. Voter and D. Doll. Dynamical corrections to transition state theory for multistate systems: Surface self-diffusion in the rare-event regime. *J. Chem. Phys.*, 82:80–92, 1985.

[44] A. F. Voter and D. Doll. Transition state theory description of surface self-diffusion: Comparison with classical trajectory results. *J. Chem. Phys.*, 80:5832–5838, 1984.

[45] G. Henkelman and H. Jónsson. Long time scale kinetic Monte Carlo simulations without lattice approximation and predefined event table. *J. Chem. Phys.*, 115:9657–9666, 2001.

[46] A. K. Erlang. Solution of some problems in the theory of probabilities of significance in automatic telephone exchanges. *Elektrotkeknikeren*, 13:5–13, 1917.

[47] Koji Hukushima and Koji Nemoto. Exchange monte carlo method and application to spin glass simulations. *J. Phys. Soc. Jpn.*, 65:1604–1608, 1996.

[48] U. H. E. Hansmann. Parallel tempering algorithm for conformational studies of biological molecules. *Chem. Phys. Lett.*, 281:140–150, 1997.

[49] Yuji Sugita and Yuko Okamoto. Replica-exchange molecular dynamics method for protein folding. *Chem. Phys. Lett.*, 314:141, 1999.

[50] W. Nadler and U. H. E. Hansmann. Optimizing replica exchange moves for molecular dynamics. *Phys. Rev. E*, 76:057102, 2007.

[51] N. Metropolis, A. W. Rosenbluth, M. N. Rosenbluth, A. H. Teller, and E. Teller. Equation of state calculation by fast computing machines. *J. Chem. Phys.*, 21:1087–1092, 1953.

[52] G. M. Torrie and J. P. Valleau. Monte carlo free energy estimates using non-boltzmann sampling: Application to the sub-critical lennard-jones fluid. *Chem. Phys. lett.*, 28:578–581, 1974.

[53] J. G. Kirkwood. Statistical mechanics of fluid mixtures. *J. Chem. Phys.*, 3:300–313, 1935.

[54] B. Roux. The calculation of the potential of mean force using computer simulation. *Comp. Phys. Comm.*, 91:275–282, 1995.

[55] P. J. Feibelman. Diffusion path for an Al adatom on Al(001). *Phys. Rev. Lett.*, 65:729–732, 1990.

[56] W. C. Swope, H. C. Andersen, P. H. Berens, and K. R. Wilson. A computer simulation method for the calculation of equilibrium constants

for the formation of physical clusters of molecules: Application to small water clusters. *J. Chem. Phys.*, 76:637–649, 1982.

[57] H. C. Andersen. Molecular dynamics simulations at constant pressure and/or temperature. *J. Chem. Phys.*, 72:2384–2393, 1980.

[58] L. Huang and D. E. Makarov. The rate constant of polymer reversal inside a pore. *J. Chem. Phys.*, 128:114903–1–114903–9, 2008.

[59] W. P. Ambrose, P. M. Goodwin, J. H. Jett, A. Van Orden, J. H. Werner, and R. A. Keller. Single molecule fluorescence spectroscopy at ambient temperature. *Chem. Rev.*, 99:2929, 1999.

[60] M. Orrit. Single-molecule spectroscopy: The road ahead. *J. Chem. Phys.*, 117:10938, 2002.

[61] F. Kulzer and M. Orrit. Single-molecule optics. *Annu. Rev. Phys. Chem.*, 55:585, 2004.

[62] P. F. Barbara. Single-molecule spectroscopy. *Acc. Chem. Res.*, 38:503, 2005.

[63] G. Hinze, G. Diezemann, and T. Basché. Rotational correlation functions of single molecules. *Phys. Rev. Lett.*, 93:203001, 2004.

[64] C.-Y. J. Wei, Y. H. Kim, R. K. Darst, P. J. Rossky, and D. Vanden Bout. Origins of nonexponential decay in single molecule measurements of rotational dynamics. *Phys. Rev. Lett.*, 95:173001, 2005.

[65] P. M. Wallace, D. R. B. Sluss, L. R. Dalton, B. H. Robinson, and P. J. Reid. Single-molecule microscopy studies of electric-field poling in chromophore polymer composite materials. *J. Phys. Chem. B*, 110:75, 2006.

[66] J. T. Fourkas. Rapid determination of the three-dimensional orientation of single molecules. *Opt. Lett.*, 26:211, 2001.

[67] A. P. Bartko, K. Xu, and R. M. Dickson. Three-dimensional single molecule rotational diffusion in glassy state polymer films. *Phys. Rev. Lett.*, 89:026101, 2002.

[68] A. P. Bartko and R. M. Dickson. Imaging three-dimensional single molecule orientations. *J. Phys. Chem. B*, 103:11237, 1999.

[69] H. Uji-i, S. M. Melnikov, J. Enderlein, and J. Hofkens. Visualizing spatial and temporal heterogeneity of single molecule rotational diffusion in a glassy polymer by defocused wide-field imaging. *Polymer*, 47:2511, 2006.

[70] M. A. Lieb, J. M. Zavislan, and L. Novotny. Single-molecule orientations determined by direct emission pattern imaging. *J. Opt. Soc. Am. B*, 21:1210, 2004.

[71] W. A. Steele. In molecular liquids: Dynamics and interactions. *NATO Advanced Studies Institute, Mathematical and Physical Sciences*, 135:111, 1984.

[72] M. D. Ediger, C. A. Angell, and S. R. Nagel. Supercooled liquids and glasses. *J. Phys. Chem.*, 100:13200, 1996.

[73] C. A. Angell, K. L. Ngai, G. B. McKenna, P. F. McMillan, and S. W. Martin. Relaxation in glassforming liquids and amorphous solids. *J. Appl. Phys.*, 88:3113, 2000.

[74] G. M. Jenkins and D. G. Watt. *Spectral analysis and Its applications.* Holden-Day, San Francisco, 1968.

[75] P. J. Brockwell and R. A. Davis. *Time series: theory and methods.* Springer-Verlag, New York, 2nd edition, 1991.

[76] G. E. P. Box and G. M. Jenkins. *Time series analysis forecasting and control.* Holden-Day, San Francisco, 1970.

[77] J. E. Anderson. Environmental fluctuations and rotational processes in liquids. *Faraday Symp. Chem. Soc.*, 6:82, 1972.

[78] D. Kivelson and T. Keyes. Unified theory of orientational relaxation. *J. Chem. Phys.*, 57:4599, 1972.

[79] D. Kivelson and D. Miles. Bimodal angular hopping model for molecular rotations in liquids. *J. Chem. Phys.*, 88:1925, 1988.

[80] B. J. Berne and R. Pecora. *Dynamic light scattering with applications to chemistry, biology, and physics.* Dover, New York, 1976.

[81] If the length of each jump is small enough, the motion can be considered taking place on a flat plane, i.e., $\partial C/\partial t = D_{rot}\nabla^2_{\theta,\phi}C \approx D_{rot}\nabla^2_{r,\vartheta}C$, where r is the (local) radial coordinate and ϑ denotes the polar angle counterpart. Thus the solution of the diffusion equation is simply the form of $K(r) = (r/2D_{rot})\ e^{-r^2/4D_{rot}}$.

[82] W. H. Press, S. A. Teukolsky, W. T. Vetterling, and B. P. Flannery. *Numerical recipes in C: The art of scientific computation.* Cambridge University Press, Cambridge, 2nd edition, 1992.

[83] N. Tomczak, N. F. van Hulst, and G. J. Vancso. Probing polymers with single fluorescent molecules. *Eur. Polym. J.*, 40:1001, 2004.

[84] When $T > 100$, the distributions $\{\tau_F\}$ and $\{\beta_F\}$ are approximately normal and thus are valid to utilize F test to judge whether these experimental distributions have different variances compared to the simulation.

[85] W. A. Steele. The rotation of molecules in dense phases. *Adv. Chem. Phys.*, 34:1, 1976.

[86] E. N. Ivanov. *Sov. Phys. JETP*, 18:1041, 1964.

[87] S. A. Rosenberg, M. E. Quinlan, J. N. Forkey, and Y. E. Goldman. Rotational motions of macro-molecules by single-molecule fluorescence microscopy. *Acc. Chem. Res.*, 38:583, 2005.

[88] D. G. Hafeman, J. B. Harkins IV, C. E. Witkowski II, N. S. Lewis, R. J. Warmack, G. M. Brown, and T. Thundat. Defocused orientation and

position imaging (DOPI) of myosin V. *Proc. Natl. Acad. Sci. U.S.A.*, 103:6495, 2006.

[89] C. R. Viteri, J. W. Gilliland, and W. T. Yip. Probing the dynamic guest-host interactions in sol-gel films using single molecule spectroscopy. *J. Am. Chem. Soc.*, 125:1980, 2003.

[90] W. Schroeyers, R. Vallée, D. Patra, J. Hofkens, S. Habuchi, T. Vosch, M. Cotlet, K. Müllen, J. Enderlein, and F. C. De Schryver. Fluorescence lifetimes and emission patterns probe the 3D orientation of the emitting chromophore in a multichromophoric system. *J. Am. Chem. Soc.*, 126:14310, 2004.

[91] H. Piwoski, C. Stupperich, A. Hartschuh, J. Sepioł, A. Meixner, and J. Waluk. Imaging of tautomerism in a single molecule. *J. Am. Chem. Soc.*, 127:5302, 2005.

[92] I. Chung, K. T. Shimizu, and M. G. Bawendi. Room temperature measurements of the 3D orientation of single CdSe quantum dots using polarization microscopy. *Proc. Nat. Acad. Sci. U.S.A.*, 100:405, 2003.

[93] J. R. Lakowicz. *Principles of fluorescence spectroscopy.* Springer, New York, 3rd edition, 2006.

[94] T. Ha, T. A. Laurence, D. S. Chemla, and S. Weiss. Polarization spectroscopy of single fluorescent molecules. *J. Phys. Chem. B*, 103:6839, 1999.

[95] M. Böhmer and J. Enderlein. Orientation imaging of single molecules by wide-field epifluorescence microscopy. *J. Opt. Soc. Am. B*, 20:554, 2003.

[96] D. Patra, I. Gregor, and J. Enderlein. Image analysis of defocused single-molecule images for three-dimensional molecule orientation studies. *J. Phys. Chem. A*, 108:6836, 2004.

[97] M. Prummer, B. Sick, B. Hecht, and U. P. Wild. Three-dimensional optical polarization tomography of single molecules. *J. Chem. Phys.*, 118:9824, 2003.

[98] B. Sick, B. Hecht, and L. Novotny. Orientational imaging of single molecules by annular illumination. *Phys. Rev. Lett.*, 85:4482, 2000.

[99] J. Hohlbein and C. G. Hübner. Simple scheme for rapid three-dimensional orientation determination of the emission dipole of single molecules. *Appl. Phys. Lett.*, 86:121104, 2005.

[100] M. F. Gelin and D. S. Kosov. What can be learned about molecular reorientation from single molecule polarization microscopy? *J. Chem. Phys.*, 125:054708, 2006.

[101] J. D. Ingle and S. R. Crouch. *Spectrochemical analysis.* Prentice-Hall, Upper Saddle River, 1988.

[102] W. C. van Etten. *Introduction to random signals and noise.* Wiley, West Sussex, 2005.

[103] C. W. Garland, J. W. Nibler, and D. P. Shoemaker. *Experiments in physical chemistry.* McGraw-Hill, New York, 7th edition, 2003.

[104] R. Zondervan, F. Kulzer, S. B. Orlinskii, and M. Orritt. Photoblinking of rhodamine 6G in poly(vinyl alcohol): radical dark state formed through the triplet. *J. Phys. Chem. A*, 107:6770, 2003.

[105] R. Zondervan, F. Kulzer, M. A. Kol'chenko, and M. Orritt. Photobleaching of rhodamine 6G in poly(vinyl alcohol) at the ensemble and single-molecule levels. *J. Phys. Chem. A*, 108:1657, 2004.

[106] F. Besenbacher, I. Chorkendorff, B. S. Clausen, B. Hammer, A. M. Molenbroek, J. K. Nørskov, and I. Stensgaard. Design of a surface alloy catalyst for steam reforming. *Science*, 279:1913–1915, 1998.

[107] J. Greeley and M. Mavrikakis. Alloy catalysts designed from first principles. *Nature Materials*, 3:810–815, 2004.

[108] H. Ye and R. M. Crooks. Effect of elemental composition of ptpd bimetallic nanoparticles containing an average of 180 atoms on the kinetics of the electrochemical oxygen reduction reaction. *J. Am. Chem. Soc.*, 129:3627–3633, 2007.

[109] J. P. Perdew and Y. Wang. Accurate and simple analytic representation of the electron-gas correlation energy. *Phys. Rev. B*, 45:13244–13249, 1992.

[110] G. Kresse. Dissociation and sticking of H_2 on the Ni(111), (100), and (110) substrate. *Phys. Rev. B*, 62:8295–8305, 2000.

[111] G. Kresse and J. Hafner. First-principles study of the adsorption of atomic H on Ni (111), (100) and (110). *Surf. Sci.*, 459:287–302, 2000.

[112] G. Kresse and J. Furthmüller. Efficiency of ab-initio total energy calculations for metals and semiconductors using a plane-wave basis set. *Compt. Mater. Sci.*, 6:15–50, 1996.

[113] P. E. Blöchl. Projector augmented-wave method. *Phys. Rev. B*, 50:17953–17979, 1994.

[114] G. Kresse and D. Joubert. From ultrasoft pseudopotentials to the projector augmented-wave method. *Phys. Rev. B*, 59:1758–1775, 1999.

[115] H. J. Monkhorst and J. D. Pack. Special points for Brillouin-zone integrations. *Phys. Rev. B*, 13:5188–5192, 1976.

Vita

Chun-Yaung Lu was born in Taipei, Taiwan in 1979. He received a BSc in Chemistry from National Taiwan University in 2001.

Permanent address: 5F., No.33, Linsen Rd., Yonghe City, Taipei
County 234, Taiwan (R.O.C.)

This dissertation was typeset with LaTeX[†] by the author.

[†] LaTeX is a document preparation system developed by Leslie Lamport as a special version of Donald Knuth's TeX Program.